Topical Review

Metamaterials with magnetism and chirality

Satoshi Tomita[1], Hiroyuki Kurosawa[2,3] Tetsuya Ueda[4], Kei Sawada[5]

[1] Graduate School of Materials Science, Nara Institute of Science and Technology, 8916-5 Takayama, Ikoma, Nara 630-0192, Japan

[2] National Institute for Materials Science, 1-1 Namiki, Tsukuba, Ibaraki 305-0044, Japan

[3] Advanced ICT Research Institute, National Institute of Information and Communications Technology, Kobe, Hyogo 651-2492, Japan

[4] Department of Electrical Engineering and Electronics, Kyoto Institute of Technology, Matsugasaki, Sakyo, Kyoto 606-8585, Japan

[5] RIKEN SPring-8 Center, 1-1-1 Kouto, Sayo, Hyogo 679-5148, Japan

E-mail: `tomita@ms.naist.jp`

November 2017

Abstract. This review introduces and overviews electromagnetism in structured metamaterials with simultaneous time-reversal and space-inversion symmetry breaking by magnetism and chirality. Direct experimental observation of optical magnetochiral effects by a single metamolecule with magnetism and chirality is demonstrated at microwave frequencies. Numerical simulations based on a finite element method reproduce well the experimental results and predict the emergence of giant magnetochiral effects by combining resonances in the metamolecule. Toward the magnetochiral effects at higher frequencies than microwaves, a metamolecule is miniaturized in the presence of ferromagnetic resonance in a cavity and coplanar waveguide. This work opens the door to the realization of a one-way mirror and synthetic gauge fields for electromagnetic waves.

Submitted to: *J. Phys. D: Appl. Phys.*

Contents

1. Introduction

Symmetry breaking is of fundamental interest in physics. Elementary particles in the universe, for example, acquire mass due to spontaneous symmetry breaking [1, 2]. A break in translational symmetry of liquid water corresponds to a phase transition to solid ice [3]. In condensed matter, symmetry breaking causes intriguing electromagnetic properties and enables us to manipulate light polarization [4]. The break in space-inversion symmetry in chiral (from the Greek $\chi\epsilon\iota\rho$, meaning hand) structures like sugars, amino-acids, proteins, helix, and spiral, causes the *optical activity (OA)*; that is to say, the natural optical activity [5]. Broken time-reversal symmetry in all materials under magnetic fields leads to the *magneto-optical (MO) effect*; for example, the Faraday effect [6].

Both the MO effect and OA bring about the polarization plane of an incident linearly-polarized light to be gradually rotated as it passes through the medium. Linearly-polarized light is regarded as a coherent superposition of left- and right-handed circularly-polarized light. In circularly-polarized light, the tip of the electric field sweeps out a helix in real space [7]. The helical pitch corresponds to electromagnetic wavelength, whereas the chirality depends on whether the helix sweeps clockwise or counter-clockwise as the wave moves along its pitch. Both the MO effect and OA can be represented by the refractive index difference between left- and right-handed circularly-polarized light. Therefore, the MO effect and OA rotating the polarization plane look similar phenomenologically when we consider only one-directional propagation. However, they have different physical origins, so that what determines the rotation direction is different. The MO effect is caused by the Lorentz force on electrons in magnetic fields and magnetized materials, whereas the OA is caused by electromagnetic induction in the chiral structures. As a result, the OA is reciprocal, where light polarization rotation direction is dependent on the light propagation direction. On the other hand, the polarization rotation direction in MO media is dependent on magnetic field or magnetization direction, but independent of the light propagation direction; that is to say, non-reciprocal.

It is very interesting to ask what light will experience when time-reversal and space-inversion symmetries are simultaneously broken (i.e., in a medium with magnetism and chirality). A combination of the MO effect and OA gives rise to the directional birefringence independent of polarizations, or the *magnetochiral (MCh) effect* [8, 9, 10, 11]. The MCh effect leads to a difference between transmission coefficients of light from the one side and the opposite side of the medium [12, 13, 14, 15, 16, 17, 18, 19, 20, 21]. The optical MCh effect is promising for new functional devices such as a non-reciprocal polarization-independent "one-way mirror". Moreover, the quest for large optical MCh effects paves the way toward the realization of an effective magnetic field (i.e., synthetic gauge fields) [22, 23, 24, 25, 26, 27, 28, 29], for electromagnetic waves. The MCh effect is, however, much weaker than the MO effect and OA in natural materials at room temperature.

A similar phenomenon called the optical magneto-electric (ME) effect is well known in multiferroic materials [30, 31, 32, 33, 34]. Intensive research efforts on directional birefringence have been devoted to realizing and enhancing intrinsic electronic interactions such as ME resonances. On the other hand, an enhancement in the optical ME effect has been reported using photonic crystals [35], gratings [36], and multilayers [37]. In this way, artificial photonic structures [38], for example, metamaterials consisting of well-designed sub-wavelength structures [39, 40, 41, 42, 43] can boost the MCh effects by several orders of magnitude.

Metamaterials (meta from the Greek $\mu\epsilon\tau\alpha$, meaning beyond) are artificial photonic materials composed of the subwavelength structures, exhibiting exotic optical properties unavailable in natural materials. In this Topical Review, we demonstrate an interplay between magnetism and chirality as the MCh effect in metamaterials. We reveal that the MCh effects occur in the unit structure – metamolecule – without using intrinsic electronic interactions [44]. Large MCh effects by the single metamolecule consisting of a ferrite rod and metallic chiral structure are directly observed at the X-band microwave frequencies under a very weak dc magnetic field of 1 mT. The effects can be enhanced by using resonance in the chiral structure and increasing the magnetic field. The non-reciprocal differences in the real and imaginary parts of refractive indices due to the MCh effect are evaluated to be 10^{-3} at 200 mT. The MCh effect can be further enhanced using magnetic resonance in the ferrite rod in the metamolecule, leading to a giant MCh effect [45]. Furthermore, miniaturization of the MCh metamolecule is demonstrated [46, 47].

We have two goals in mind for this Review. One is to introduce to researchers in magnetics, optics, photonics, and chemistry communities the MCh effects given by natural- and meta-materials having magnetism and chirality simultaneously. The MO effect and OA have long histories in science and technology, providing many useful applications using polarization rotations. Reciprocal OA by chirality was first observed by Arago [4] in 1811, more than 200 years ago. OA is used to characterise the molecular chirality in chemistry, biology, and pharmaceutical chemistry. Non-reciprocal MO effects, which were discovered by Faraday [4] in 1845 using glass under magnetic fields, are familiar in magnetics, photonics, and microwave engineering. The MO effects by magnetism was utilized in MO drives for data storage in 1980s. Moreover, the MO effects enable us to realize optical isolators and circulators, which, in the information technology era, are indispensable devices for modern photonic networks.

The apparent similarity of the MO effect and OA motivated Pasteur to search in vain for a link between the two phenomena just after the discovery of the Faraday effect [48]. Nevertheless, as the technologies relevant to the MO effect and OA become matured, the link does not attract attention. The MCh effect by materials having magnetism and chirality simultaneously is thus less familiar to the researchers, although the MCh effect is of great interest also in the origin of life, quantum vacuum phenomena, and electric devices. Therefore, in this Review, by identifying and comparing the MO effect and OA, and by using translation from photonic to electronic systems (and vice versa) based on the analogy, we attempt to bridge the gap between the MO effect and

OA, and provide a "road map" to the MCh effect.

The other goal is to introduce the metamaterials with both magnetism and chirality to condensed-matter physicists and material scientists. In order to obtain the MCh effects, natural chiral materials, for example, chiral molecules [12, 14, 15] and chiral crystals [17, 21], under magnetic fields have been intensively studied so far. Here we would propose an alternative route to the interplay between magnetism and chirality in structured metamaterials, which are complementary to the natural materials. This route enables us to understand and control the interplay in photonic media. Furthermore, the interplay between magnetism and chirality is of great interest in electronic systems; for example, topological spin textures like Skyrmion [49].

Based on an analogy between electronic and photonic systems, metamaterials with both magnetism and chirality introduced here offer a good playground for proof-of-concept experiments, which are difficult to be carried out in electronic counterparts. For example, phase difference is directly measured in photonic systems using microwaves while it is unlikely in electronic systems. The obtained knowledge using optical metamaterials can be exported to electronic systems so that it may help in understanding the physics underlying the complex electronic systems. The present study is thus one further step for a new avenue of analogy between electrons and lights.
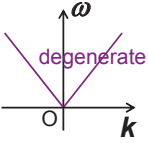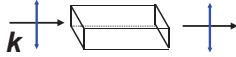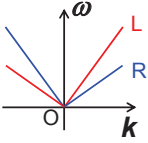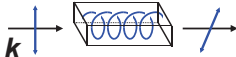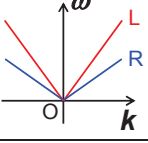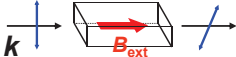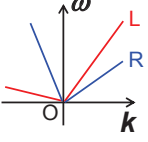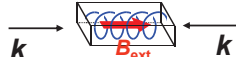
This Review is organized as follows. Section 2 introduces metamaterials with magnetism and chirality accompanied by the MCh effects. Section 3 demonstrates experimental procedures and results of X-band microwave transmission measurements through a single MCh metamolecule in a waveguide under weak and strong magnetic fields. In Section 4, numerical calculations reproduce the experimental results and shed light on the physics of the MCh effects by the metamolecule. Section 5 outlines and discusses the mechanism of the enhanced and giant MCh effects by the metamolecules. Section 6 details miniaturization of the metamolecules with magnetism and chirality. Finally Section 7 concludes the paper and gives outlook for further studies.

2. Prelude to metamaterial with magnetism and chirality

In this section, we introduce metamaterials with magnetism and chirality, and derive the MCh effect from a viewpoint of the symmetry breaking. In 2.1, optical phenomena caused by symmetry breaking are briefly summarized. Explanations for OA in 2.2 and the MO effect in 2.3 will lead to an introduction to the MCh effect in 2.4. Subsection 2.5 describes the historical background, concept, and variation of metamaterials.

2.1. Symmetry breaking and optical phenomenon

Optical phenomena are easily understood and categorized by considering dispersion relations. The top row of Fig. 1 shows that normal media without any symmetry braking have degenerated and symmetric dispersion relations, resulting in conventional propagation. Let us move on to media with broken symmetry and consider dispersion

Broken symmetry	Dispersion	Phenomenon
None		Conventional propagation
Space-inversion symmetry		Optical activity (OA)
Time-reversal symmetry		Magneto-optical (MO) effect
Time-reversal symmetry & Space-inversion symmetry		Magneto-chiral (MCh) effect

Figure 1. Summary of broken symmetries in condensed matter and optical phenomena with dispersion relations.

relation, $\omega = \omega_{\mathrm{L,R}}(\vec{k})$, where L and R denote left- and right-handed circularly-polarized light, respectively. Note that the two circular polarizations are defined as eigenstates of angular momentum as will be described in 2.2.1. The time-reversal operation transforms the dispersion as $\omega_{\mathrm{L,R}}(\vec{k}) \to \omega_{\mathrm{R,L}}(-\vec{k})$. A system with the time-reversal symmetry shown in the second row in Fig. 1 satisfies the following relations,

$$\omega_{\mathrm{L}}(\vec{k}) = \omega_{\mathrm{R}}(-\vec{k}),$$
$$\omega_{\mathrm{R}}(\vec{k}) = \omega_{\mathrm{L}}(-\vec{k}). \tag{1}$$

Similarly, if a system sustains the space-inversion symmetry, the dispersion satisfies the relations,

$$\omega_{\mathrm{L}}(\vec{k}) = \omega_{\mathrm{L}}(-\vec{k}),$$
$$\omega_{\mathrm{R}}(\vec{k}) = \omega_{\mathrm{R}}(-\vec{k}), \tag{2}$$

as shown in the third row in Fig. 1. Therefore, under the symmetry breakings of the time-reversal and/or the space-inversion, Eqs. (1) and (2) are not the case. Especially, if a system lacks both the time-reversal and the space-inversion symmetry as shown at the bottom in Fig. 1, unpolarized electromagnetic waves can have directional dependence, namely the MCh effects. In Fig. 1, schematics of these optical phenomena are summarized together with corresponding dispersion relations.

An analogy between optical and electronic systems is helpful to understand the physics underlying the phenomena. Circular polarizations are interpreted as labels of the angular momenta and also as "spins" of photons. Here we give an intuitive picture

of a general relation between the spin states and the symmetry breaking. Consider a simple case where an electron and photon with spin 1/2 and 1, respectively, are moving to some direction. Each has two spin degrees of freedom. To distinguish those states, one method is to break a symmetry such as the space-inversion and the time-reversal symmetry. In an electronic system, spin-orbit interactions require a break of the space-inversion symmetry. Such a system has a dispersion similar to that in photonic systems with OA as shown in Fig. 1. Another case is a magnetic system where the external magnetic field splits the energy level. This is the Zeeman effect in electric systems, corresponding to the MO effect in optical systems. In the following, we look in more detail at OA in a medium with broken space-inversion symmetry and the MO effect in a medium with broken time-reversal symmetry. Then let us consider electromagnetism in a medium lacking both the space-inversion and time-reversal symmetries, i.e., in an MCh medium.

2.2. Optical activity (OA)

Broken space-inversion symmetry causes OA (chiral birefringence or chiroptical effect). The OA in transmission brings about polarization plane rotations of linearly-polarized light, which is regarded as a coherent superposition of left- and right-handed circularly-polarized light. This is so-called optical rotation (OR) [4], caused by phase delay (retardation) between left- and right-handed circularly-polarized light. The OR is evaluated by rotation angle in a unit of degree. The phase delay is represented by a difference in the real parts of refractive indices between left- and right-handed circularly-polarized light. Refractive index usually shows frequency dispersion. The frequency dependent change in OR is thus referred to as optical rotatory dispersion.

In absorptive OA media, OR is accompanied by circular dichroism (CD), which is caused by the absorption difference between left- and right-handed circularly-polarized light. The CD is given by ellipticity also in degree. The absorption difference is represented by a difference in the imaginary parts of refractive indices between left- and right-handed circularly-polarized light. In this way, after transmission through an absorptive OA medium, the initially linearly-polarized light transforms to elliptically-polarized one because of the superposition of OR and CD. We note that OA is dependent on chirality of the medium; OR (CD) angle has opposite sign between left- and right-handed systems; that is to say, between enantiomers (non-superposable mirror-image structures) [50]. An effect of chirality is represented by chiral parameter ξ.

The OA is known to be symmetric transmission because the rotation angle is dependent on the light propagation direction. Let us assume that we observe the phenomena from the light source and an angle in OR is θ after transmitting through a chiral medium with very small absorption from the one side. If the light transmits the same medium from the opposite side after the reflection by a mirror, the rotation angle is $-\theta$ because the rotation angle is dependent on the light propagation direction. This causes the zero rotation if the light is first transmitted from the one side and then

transmitted from the other after a reflection by a mirror. This is so called reciprocity.

OA is due to electromagnetic induction in the chiral structures. In other words, microscopic origin of OA is magnetic dipoles that are excited in the chiral structures by the electric component of light and vice versa [7, 51]. In a plane wave, the incident electric and magnetic field components are perpendicular to each other. When, as the wave passes through the OA medium, the magnetic component induces an electric dipole parallel to the light magnetic field, the resulting net local electric field will be rotated a bit. Reciprocity demands that, likewise, magnetic dipoles are excited by the electric component. In this way, the magnetic field of light rotates as well. For pure chirality, the locally induced magnetic (electric) dipoles need to be parallel to the local exciting electric (magnetic) field. In this case, the eigen-polarizations correspond to circular polarization of light, whereas they are elliptic in the more general nonparallel (i.e., bianisotropic) case.

2.2.1. Chirality and helicity In this part, we mention two technical terms, chirality and helicity. These terms are used in various fields of science but their meanings depend on the context, which sometimes makes confusion. Chirality means a kind of asymmetry. If an object is chiral, it is distinguishable from its mirror image. Examples are found in left- and right-hands, sugar molecules, and spiral structures. These systems lack space-inversion symmetry and have OA.

Helicity is contrastingly a degree of some rotating motion or structures. For example, the helicity of a vector field, $\vec{v}(\vec{r})$, is defined as $H = \int \vec{v} \cdot (\nabla \times \vec{v}) d\vec{r}$, which is used in fluid mechanics and magnetism. In elementary particle physics, the helicity is defined as a projection of the spin angular momentum onto the direction of momentum, which is described as

$$h = \frac{\vec{S} \cdot \vec{p}}{|\vec{p}|}, \tag{3}$$

where $\vec{S}$ and $\vec{p}$ are the spin and the momentum, respectively. If a circularly-polarized electromagnetic wave is propagating to the z-direction, it has the eigenvalues of the helicity, $h = \pm 1$, where $\pm$ correspond to left- and right-handed polarizations.

Here we have to note that the definition of the circular polarizations are often confusing. In some articles, circular polarizations are defined by their helicities that are odd under the space-inversion operation. In this paper, on the other hand, we define circular polarizations corresponding to the angular momentum that is even under the space-inversion operation [4].

2.3. Magneto-optical (MO) effect

The break in time-reversal symmetry in magnetic fields or magnetized materials causes MO effect. Contrastingly to natural OA associated with intrinsic chirality, the MO effect is induced by external fields, i.e., the induced optical effect [4]. Here we consider the MO effect in transmission configuration where an external magnetic field is applied

along the electromagnetic wave propagation direction; that is to say, the Faraday effect. However, the physics underlying the phenomena is similar in reflection configuration, so-called, longitudinal/transverse/polar MO Kerr effects [52, 53], and in transmission configuration where an external magnetic field is applied in a direction perpendicular to the electromagnetic wave propagation, so-called, the Voigt and Cotton-Mouton effects.

Phenomenologically similar to OR and CD, the MO effect gives rise to polarization plane rotations of linearly-polarized light, i.e., Faraday rotation (FR) and magnetic circular dichroism (MCD). The FR is caused by the phase delay, whereas MCD is owing to the absorption difference between left- and right-handed circularly-polarized light. Both FR and MCD are given in degrees. Contrastingly to the OA, polarization-plane rotation angles in FR and MCD are determined by the magnetic field or magnetization directions. If we look the phenomena from the light source and even if the light propagation direction is in parallel or anti-parallel along to the magnetic field direction, the FR (MCD) angle has the same sign.

Let us assume that an angle in FR is θ after transmitting from the one side of a magnetized MO medium with very small absorption. When the light transmits the medium again from the opposite side after reflecting by a mirror, the rotation angle is θ again because the rotation angle is dependent on the magnetization direction. This causes the 2θ rotation in total. In other words, the transmission of circularly-polarized light is anti-symmetric in an MO medium. This is so called non-reciprocity.

The MO effect is caused by the Lorentz force on electrons by magnetic fields. Lorentz force is directed normal to the magnetic field and to the electron motion. Therefore, the magnetic permeability of MO media becomes tensor $\hat{\mu}$ and has the non-zero off-diagonal components:

$$\hat{\mu} = \begin{pmatrix} \mu_{xx} & -i\kappa & 0 \\ i\kappa & \mu_{yy} & 0 \\ 0 & 0 & \mu_{zz} \end{pmatrix}. \tag{4}$$

On the off-diagonal component, MO parameter κ is proportional to the external magnetic field and gives MO effect.

2.4. Magnetochiral (MCh) effect

Now we may ask naturally what electromagnetic waves experience in a material having magnetism and chirality simultaneously. Combination of the MO effect and OA in the Faraday configuration gives rise to the optical MCh effect, in other words, the directional birefringence which is independent of polarizations. The MCh effect was first predicted theoretically [8, 9, 10, 11] and then experimentally verified by Rikken and Raupach [12] in absorption, i.e., magnetochiral dichroism (MChD) as shown in Fig. 2(a).

Five strategies are found in a route to achieving the MCh effects using natural or artificial materials. The first one is that natural chiral molecules under strong magnetic field [12, 13, 14, 15, 54, 55]. In optically active organic liquids, variations in refractive indices due to the MCh effect in the visible region were measured to be quite small; for
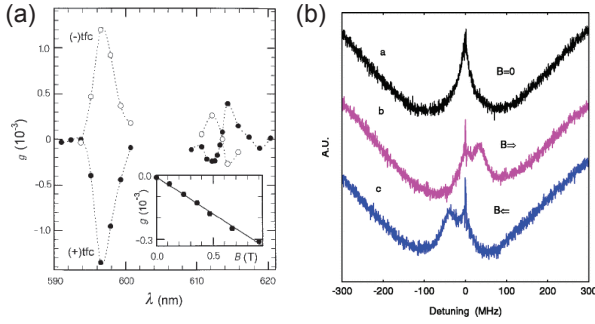
Figure 2. (a) MChD of natural chiral molecules under magnetic field and (b) optically induced chirality in the atomic vapor cell using coherent control. (a) is reprinted by permission from Macmillan Publishers Ltd: [12], copyright (1997). (b) is reprinted figure with permission from [16], copyright (2005) by the American Physical Society.

example, 10^{-8} at 5 T [13] and 10^{-10} at 100 mT [15] using interferometric detection. The second route is via optically-induced chirality in the atomic vapor cell using coherent control [16] as shown in Fig. 2(b). Third, molecular magnets, for example, the two-dimensional (2D) oxalate-based chiral magnets [18], are utilized as shown in Fig. 3(a). In the forth strategy, chirality is incorporated in bulk magnetic materials: for example, noncentrosymmetric canted antiferromagnet CuB_2O_4 [17], antiferromagnet $Ba_2CoGe_2O_7$ that undergoes a magnetic-field driven transition to a chiral form [19], the electromagnon resonance in the screw spin helimagnet $CuFe_{1x}Ga_xO_2$ ($x = 0.035$) [20] as shown in Fig. 3(b), and the multiferroic chiral-lattice magnet Cu_2OSeO_3 [21, 56] as shown in Fig. 3(c) under static dc magnetic fields. The last one is a few attempts to observe the MCh effect using artificial structures [57, 58].

The MCh effect in natural materials is much smaller than the MO effect and OA due to a weak coupling between magnetism and chirality. Hence it becomes important to enhance the magnetochiral coupling. Artificial structured metamaterials are promising routes to achieve the enhancement. In the following, we derive the MCh effects and address how we can enhance the MCh effects. Starting from constitutive equations in a medium with both magnetism and chirality, and Maxwell equations in 2.4.1, we obtain a refractive index of the medium in 2.4.2. In 2.4.3, a small comment at visible frequencies is given when the MO parameter is included in electric permittivity tensor. Furthermore, we introduce several considerable phenomena relevant to the MCh effects; for example, synthetic gauge fields, the homochirality and quantum vacuum effect in 2.4.4 and optical ME effect in 2.4.5.

2.4.1. Wave equation in medium with magnetism and chirality Based on the aforementioned discussion, let us explicitly derive the optical MCh effects by calculating the dispersion. Maxwell equations read

$$\nabla \times \vec{E}(\vec{r}, t) = -\frac{\partial \vec{B}(\vec{r}, t)}{\partial t}, \tag{5}$$
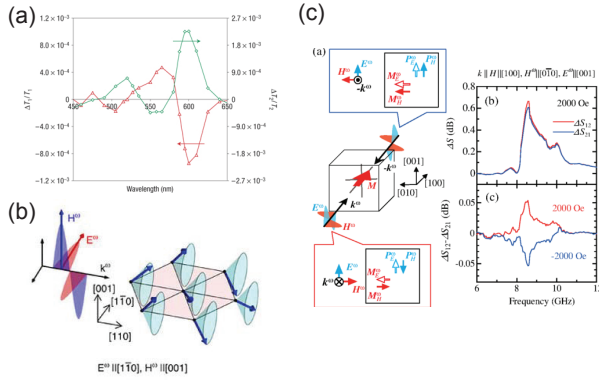
Figure 3. (a) MCh effect by oxalate-based chiral magnets. Reprinted by permission from Macmillan Publishers Ltd: [18], copyright (2008). (b) The screw spin helimagnet CuFe$_{1x}$Ga$_x$O$_2$ ($x = 0.035$). Reprinted by permission from Macmillan Publishers Ltd: [20], copyright (2014). (c) MCh effect by the multiferroic chiral-lattice magnet Cu$_2$OSeO$_3$. Reprinted figure with permission from [21], copyright (2015) by the American Physical Society.

$$\nabla \times \vec{H}(\vec{r},t) = \frac{\partial \vec{D}(\vec{r},t)}{\partial t}, \tag{6}$$

1 where $\vec{E}$, $\vec{B}$, $\vec{H}$, and $\vec{D}$ are the electric field, the magnetic flux density, the magnetic
2 field, and the electric flux density, respectively. The constitutive equations of the chiral
3 media with magnetism are written as

$$\vec{D}(\vec{r},t) = \varepsilon_0 \hat{\varepsilon} \vec{E}(\vec{r},t) - i\frac{\hat{\xi}}{c}\vec{H}(\vec{r},t), \tag{7}$$

$$\vec{B}(\vec{r},t) = \mu_0 \hat{\mu} \vec{H}(\vec{r},t) + i\frac{\hat{\xi}}{c}\vec{E}(\vec{r},t), \tag{8}$$

4 where the parameters, $\hat{\varepsilon}$ and $\hat{\mu}$, are respectively the electric permittivity and the
5 magnetic permeability tensors of the medium. The permeability $\hat{\mu}$ plays a major role to
6 characterize electromagnetic interactions in the microwave region, and the permittivity
7 is assumed to be a scalar, $\hat{\varepsilon} = \varepsilon\hat{1}$. The chirality tensor $\hat{\xi}$ represents an effect of structural
8 chirality that breaks the space-inversion symmetry. Before we rush to substitute Eqs.
9 (7) and (8) into Maxwell equations [Eqs. (5) and (6)] for obtaining wave equation, we
10 must pause to consider another option in ε. In the visible region, $\hat{\varepsilon}$ plays a major role
11 to characterize electromagnetic interactions. Hence, we will briefly give an derivation of
12 the MCh effect in the visible region in 2.4.3.

13   To realize the MCh effect, we break the time-reversal symmetry by applying
14 an external magnetic field to the z-direction. The magnetic permeability $\hat{\mu}$ can be
15 represented by Eq. (4). On the off-diagonal component, the MO parameter κ, which
16 is proportional to the external magnetic field, gives MO effects such as the Faraday
17 effect. We consider a plane wave with the wave vector, $\vec{k} = (\vec{k}_{\text{t}}, k_z)$, where the subscript
18 "t" denotes the transverse component. Now we consider plane waves of $\vec{E}$, $\vec{B}$, $\vec{H}$, and
19 $\vec{D} \propto e^{i\vec{k}\cdot\vec{r}-i\omega t}$. Equations (5) and (6) become

$$\vec{k} \times \vec{E}(\vec{r}) = \omega \vec{B}(\vec{r}), \tag{9}$$

$$\vec{k} \times \vec{H}(\vec{r}) = -\omega \vec{D}(\vec{r}). \tag{10}$$

Let us write $\vec{E}$ and $\vec{B}$ in terms of $\vec{H}$. From Eqs. (7) and (10), the electric field is written as

$$\vec{E} = \frac{1}{\varepsilon_0 \varepsilon} \Big[\frac{-1}{\omega} \vec{k} \times \vec{H} + i\frac{\hat{\xi}}{c} \vec{H} \Big], \tag{11}$$

where position dependence is omitted for simplicity. Substituting this representation of the electric field into Eq. (8), we get

$$\vec{B} = \mu_0 \hat{\mu} \vec{H} + i\frac{1}{c\varepsilon_0 \varepsilon} \hat{\xi} \Big[\frac{-1}{\omega} \vec{k} \times \vec{H} + \frac{\hat{\xi}}{i} \vec{H} \Big]. \tag{12}$$

From Eqs. (11) and (12) combined with Eq. (9), the wave equation is written to be

$$-\vec{k} \times (\vec{k} \times \vec{H}) - i\vec{k} \times (\hat{\xi}\vec{H}) - i\hat{\xi}(\vec{k} \times \vec{H})$$
$$= \frac{\omega^2}{c^2} \varepsilon \hat{\mu} \vec{H} + \frac{\omega}{c} \hat{\xi}^2 \vec{H}. \tag{13}$$

2.4.2. Dispersion relation and refractive index We assume that chiral axis is parallel to the z-direction corresponding to our experimental setup shown later. The chirality tensor is written as

$$\hat{\xi} = \begin{pmatrix} 0 & 0 & 0 \\ 0 & 0 & 0 \\ 0 & 0 & \xi \end{pmatrix}. \tag{14}$$

This means that the z-component of the electric field induces that of the magnetic field, and vice versa. In this case, it is convenient to separate the propagation direction into the transverse and the longitudinal components [59] to be $\vec{k} = (\vec{k}_t, k_z)$. Given that $\mu_{xx} = \mu_{yy} = \mu_{zz} = \mu$ in Eq. (13), the dispersion relation, namely the index ellipsoid, is obtained to be

$$\frac{k_t^2}{(n_t^\pm)^2} + \frac{k_z^2}{(n_z^\pm)^2} = \frac{\omega^2}{c^2}, \tag{15}$$

where

$$n_t^\pm = \sqrt{\varepsilon}\sqrt{\mu} \pm \frac{1}{4}\sqrt{\frac{\varepsilon}{\mu}}\kappa \pm \frac{\xi}{2} + \frac{1}{4}\xi\frac{\kappa}{\mu}, \tag{16}$$

$$n_z^\pm = \sqrt{\varepsilon}\sqrt{\mu} \pm \frac{1}{2}\sqrt{\frac{\varepsilon}{\mu}}\kappa. \tag{17}$$

These are refractive indices in which the sign $\pm$ represents polarization states.

Here we focus on Eq. (16) that consists of four terms with different physical meanings. The first term on the right-hand side is a conventional dispersion without symmetry breakings. The second term is proportional to the external magnetic field that breaks the time-reversal symmetry. This term represents the MO effect and depends on polarization states. The third term also depends on polarization states and has directional dependence, representing OA by the chirality that breaks the space-inversion symmetry. The fourth term in the right-hand side of Eq. (16) represents

₁ what we are looking for in this paper, the MCh effect. This term is independent
₂ of polarization states but depends on propagation directions [60]. Such properties
₃ are caused by the simultaneous breaking of the time-reversal and the space-inversion
₄ symmetries, as summarized in Fig. 1. The MCh effect term contains a product of ξ and
₅ κ, which are originally dependent on light polarization. However, the product results
₆ in a cancel of the polarization dependence, leading to the polarization-independent
₇ directional birefringence.

₈ Our derivation here implies that the MCh effect is realized without an explicit
₉ coupling between the MO effect and OA. Even without the coupling, electromagnetic
₁₀ waves regard κ and ξ combined together as a fictitious interaction, which corresponds
₁₁ to the cascade MCh anisotropy [54]. This is very similar to the conventional refractive
₁₂ index, namely the first term in the right-hand side of Eq. (16), where electromagnetic
₁₃ waves regard ε and μ combined together. In this way, large MCh effects can be achieved
₁₄ by decoupling between κ and ξ, enhancing κ and ξ independently, and combining κ and
₁₅ ξ in the sub-wavelength region.

₁₆ *2.4.3. MO parameter in electric permittivity tensor* In the visible light region, the MO
₁₇ effect is represented by the off-diagonal components of the electric permittivity tensor
₁₈ $\hat{\varepsilon}$. In this case, the MCh effects are similarly derived as the previous section. Consider a
₁₉ light propagation through a magnetic medium under the external magnetic field parallel
₂₀ to the propagating direction, the z-direction. The electric permittivity tensor is written
₂₁ to be

$$\hat{\varepsilon} = \begin{pmatrix} \varepsilon & -i\chi^{\mathrm{MO}} & 0 \\ i\chi^{\mathrm{MO}} & \varepsilon & 0 \\ 0 & 0 & \varepsilon \end{pmatrix}, \tag{18}$$

₂₂ where χ^{MO} is assigned to the MO parameter in electric permittivity tensor. The
₂₃ magnetic permeability is assumed to be diagonal and $\mu_{xx} = \mu_{yy} = \mu$. The wave equation
₂₄ for the electric field vector is obtained to be

$$-\vec{k} \times (\vec{k} \times \vec{E}) - i\vec{k} \times (\hat{\xi}\vec{E}) - i\hat{\xi}(\vec{k} \times \vec{E})$$
$$= \frac{\omega^2}{c^2}\hat{\varepsilon}\mu\vec{E} + \frac{\omega}{c}\hat{\xi}^2\vec{E}. \tag{19}$$

₂₅ This equation has the same form as Eq. (13) with correspondence, $\vec{H} \leftrightarrow \vec{E}$ and $\hat{\varepsilon} \leftrightarrow \hat{\mu}$.
₂₆ Therefore the indices of refraction are written to be

$$n_{\mathrm{t}}^{\pm} = \sqrt{\varepsilon}\sqrt{\mu} \pm \frac{1}{4}\sqrt{\frac{\varepsilon}{\mu}}\chi^{\mathrm{MO}} \pm \frac{\xi}{2} + \frac{1}{4}\xi\frac{\chi^{\mathrm{MO}}}{\mu}, \tag{20}$$

$$n_{z}^{\pm} = \sqrt{\varepsilon}\sqrt{\mu} \pm \frac{1}{2}\sqrt{\frac{\varepsilon}{\mu}}\chi^{\mathrm{MO}}. \tag{21}$$

₂₇ The fourth term on the right hand side in Eq. (20) represents the MCh effects.

₂₈ *2.4.4. MCh effect in optics, photonics, chemistry, biology, and quantum mechanics*
₂₉ The MCh effect leads to the difference between transmission coefficients of

electromagnetic waves from the one side and the opposite side of the medium. A large MCh effect is thus promising for new functional devices such as a polarization-independent non-reciprocal one-way mirror. While non-reciprocal polarization-independent directional birefringence can be implemented using a combination of several optical components, for example, an MO medium, birefringent medium, and $\lambda/2$ wavelength plates, its realization in a single (meta)material would promise a variety of applications in the photonic networks.

Furthermore, the quest for large MCh effects paves a way toward the realization of synthetic gauge fields [24, 25, 26, 27]. Suppose electromagnetic waves through metamaterials with the refractive index gradient, i.e., a spatial variation in the meta-atom or metamolecule density, in a direction perpendicular to the wave incident direction. The refractive index gradient due to the spatial variation deflects the center of gravity of the beam [29]. If the metamaterials consist of non-reciprocal MCh metamolecules, the bending direction depends on the beam propagation direction. The trajectory of electromagnetic wave is very similar to that of electrons under a magnetic field owing to the Lorentz force even though photons not having electric charges never feel the intrinsic Lorentz force by a magnetic field. Since materials are regarded as "fields" by electromagnetic waves, an effective magnetic field for electromagnetic waves [22, 23, 28] can thus be synthesized using non-uniform gradated MCh metamaterials.

The MCh effects are of interest not only in condensed matter physics and material science but also in completely different fields at first blush, for example, biology and quantum physics. It is well known that the chemistry of life is homochiral, being almost exclusively on L-amino acids and D-sugars [48]. L and D are respectively from the Latin *levo* (meaning left) and *dextro* (meaning right) of molecular structure in chemistry. The ability of biological molecules to discriminate between enantiomers is vital for living system. The homochirality in biology and biochemistry is a big question and still under intensive discussion. Rikken and Raupach [14] reported that MChD with chiral molecule complex in solution is utilized to favor the production of one enantiomer in photochemical reactions. This enantioselective MCh photochemistry sheds light to the big question of the possible origins for biological homochirality [48].

In contrast to the macroscopic biological systems, microscopic systems are described by the quantum mechanics. The quantum theory of the free electromagnetic field in the absence of any source was formulated by Born, Heisenberg, and Jordan [61]. After the first application made by Dirac [62], the quantum electrodynamics predicted a fluctuating zero-point or "vacuum" field existing even in the absence of any sources. In other words, the electromagnetic quantum vacuum is not empty but filled with the Casimir energy [63, 64], which is proven convincingly by the attraction between two conducting plates [65]. The quantum electrodynamics calculations were carried out to demonstrate that the kinetic Casimir momentum transferred from the quantum vacuum to an MCh system, in which a chiral oscillator is subject to only an external dc magnetic field [66, 67]. The resulting MCh Casimir momentum is a tiny, but non-zero for the magnetic dipole case, while it vanishes rigorously for the electric dipole case.

The momentum transfer is expressed in terms of observable parameters, for example, the molecular rotatory factor, enabling us to realize zero-point tweezers [68], by which the object's motion can be manipulated by vacuum fluctuations.

2.4.5. Magneto-electric (ME) effect Similarly to the MCh effects, a directional birefringence independent of polarization, called the optical ME effect, is observed in multiferroic materials [30, 31, 32, 33]. While the MCh effect is observed in the Faraday configuration, the optical ME effect is observed in the Voigt configuration, where light transmits through the medium under an external magnetic field in a direction perpendicular to the light propagation. The optical ME effect is represented by the off-diagonal component in the ξ tensor, which is independent of the light polarization.

Recently, one-way transparency due to the optical ME effect has been reported in natural materials at low temperature and/or under strong magnetic field in multiferroic CuB_2O_4 for near-infrared light [34] as shown in Fig. 4(a). In the multiferroic materials, the one-way transparency is traced back to the interference between the $E1$ and $M1$ transitions under the condition that the two transitions have the same amplitude. Intensive research efforts on directional birefringence have been devoted to realizing and enhancing intrinsic electronic interactions such as ME resonances. On the other hand, several studies have been reported to enhance the optical ME effect by using photonic crystals [35] [Fig. 4(b)], gratings [36], and multilayers [37] mainly in optical regions. An enhancement of directional birefringence using photonic structures was theoretically demonstrated [38] as shown in Fig. 5. In this calculation, the ME effect was phenomenologically taken into account by directional dependence of refractive indices. This result is also applicable for the MCh effects. In this way, the MCh effect can be enhanced by artificial photonic structures, for example, metamaterials consisting of well-designed sub-wavelength structures [43].

2.5. Metamaterial

A periodic array of artificial elements can behave as an effective medium for scattering when the wavelength is much longer than both the element dimension and lattice spacing. In other words, waves regard the materials as media with effective parameters by coarse graining. Such artificial materials consisting of the subwavelength structures and bringing about unusual and nonintuitive optics not observed in ordinary materials are called metamaterials [43]. Because the coarse graining is applicable to another waves, metamaterials after the discovery in electromagnetism at the last year of the 20th century [41] are now expanding into acoustic [69, 70] and seismic wave propagations [71], and even into heat diffusion [72, 73]. In this Topical Review, however, we focus on electromagnetic metamaterials unless otherwise noted.

Metamaterial research was triggered by realizing negative index of refraction by Schultz, Smith, and co-workers [41, 42] as shown in Fig. 6(a). Refractive index (n) is defined by how the electromagnetic waves behave at the interface between different
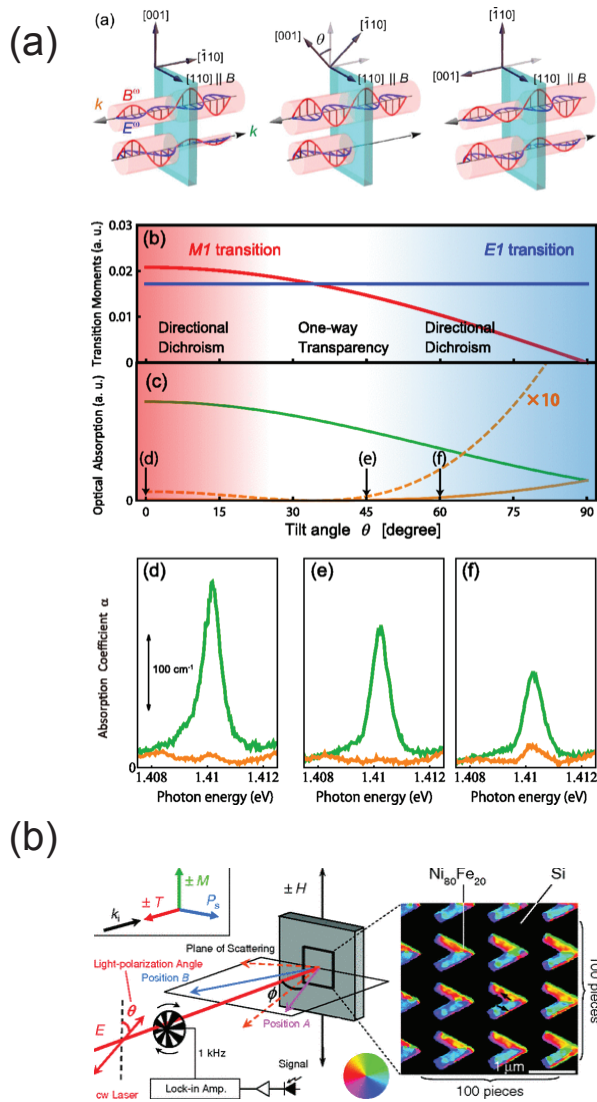
Figure 4. ME effects by (a) natural multiferroic CuB_2O_4 and (b) artificial photonic crystals. (a) is reprinted figure with permission from [34], copyright (2015) by the American Physical Society. (b) is reprinted figure with permission from [35], copyright (2005) by the American Physical Society.

photonic media; that is to say, Snell's law. The n consisting of electric permittivity (ε) and magnetic permeability (μ) in $n = \sqrt{\varepsilon}\sqrt{\mu}$ has positive value larger than unity in most propagative materials because of dispersive and narrow-band characteristics of ε and μ. What makes the metamaterials special is that the effective ε and μ can simultaneously have values not observed in ordinary materials. A negative refractive index stemming from the sign change of the group velocity was a long standing issue [74, 75] as found in the literature about the negative group velocity by Burillouin [76]. Veselago [77] theoretically investigated the electrodynamic consequences of a medium both ε and μ negative. He concluded that such a material would be propagative, but show dramatically different propagation characteristics, including negative refractive
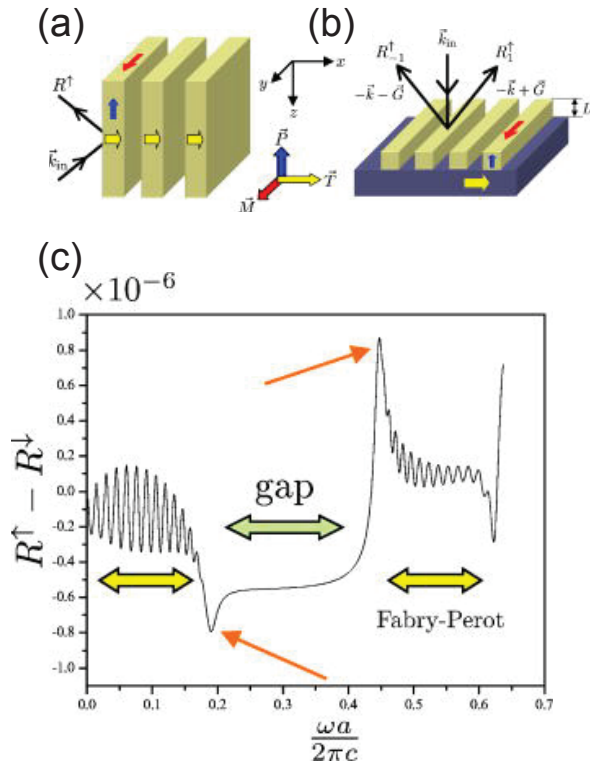
Figure 5. Enhancement of directional birefringence using photonic crystals. Schematic illustration of (a) a magnetochiral multilayer and (b) a stripe structure whose constituent materials are multiferroics and air. (c) Frequency dependence of calculated reflectivity for the normal incidence. Reprinted from [38], with the permission of AIP Publishing.

index, reversal of Doppler shift and Cherenkov radiation, and even reversal of radiation pressure to radiation tension. In contrast to ordinary "right-handed" (not in terms of chirality) materials with positive n, such materials were originally termed "left-handed" materials, where $\vec{E}$, $\vec{H}$, and $\vec{k}$ form the left-handed configuration. However, in this Topical Review, we refer to the left-handed material as a negative-refractive-index material for avoiding the confusion with the chirality.

A recipe for the negative-refractive-index materials was described by Pendry and co-workers [39, 40, 78]. They showed theoretically how to prepare an artificial photonic material consisting of metallic thin wires in which the effective plasma frequency is depressed by up to six orders of magnitude, leading to effectively negative ε in microwave frequencies [39]. Furthermore, they introduced a periodic array of nonmagnetic, for example, Cu, conducting units, referred to as split-ring resonators (SRRs), whose dominant behavior can be interpreted as having an effective μ in microwave region [40]. By making the SRRs resonant, the magnitude of effective μ is enhanced considerably, leading to negative effective μ near the high frequency side of the resonance. For human being, these artificial structures look similar to electric circuits rather than materials. Indeed, the SRR resonance is interpreted as a LC resonance in the ring-shaped circuit
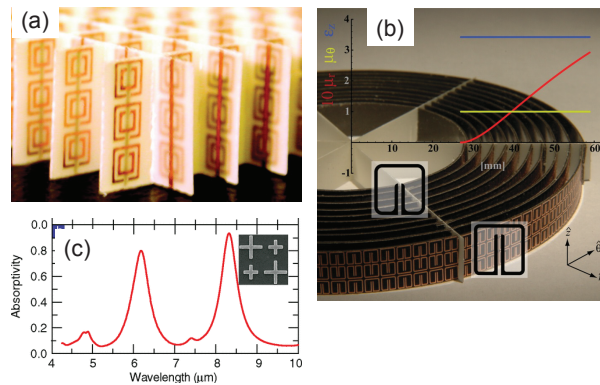
Figure 6. (a) Negative-refractive-index metamaterials at microwave frequency from [42]. Reprinted with permission from AAAS. (b) Metamaterial invisible cloak for microwaves form [93]. Reprinted with permission from AAAS. (c) Absorptivity spectrum of metamaterial perfect absorbers in the infrared region. Reprinted figure with permission from [99], copyright (2011) by the American Physical Society.

[79]. However, as far as external electromagnetic radiation is concerned, these structures appear as a homogeneous dielectric medium having effective ε and μ.

Schultz, Smith, and co-workers [41] constructed a metamaterial by integrating the well-designed Cu SRRs with Cu thin wires, resulting in an overlap between negative μ and ε at a microwave frequency. When the deflection of a beam of microwave radiation was measured as the beam passed through the prism-shaped sample, a negative refractive index was experimentally verified [42]. After this discovery, metamaterials are intensively studied toward optical frequencies by miniaturizing the constituent units [79, 80, 81, 82, 83, 84, 85, 86]. Moreover, a variety of exotic phenomena were predicted and implemented by metamaterials; for example, a high-performance plano-concave lens [87], perfect [88] /super [89] / hyper [90] lenses, electromagnetic cloaks for invisibility [91, 92, 93, 94, 95, 96], and perfect absorbers [97, 98, 99]. Recent progresses of electromagnetic metamaterials are summarized in these literatures [43, 100, 101, 102, 103, 104, 105, 106, 107, 108, 109, 110, 111, 112, 113, 114, 115, 116, 117].

2.5.1. Metamaterial concept A key concept of metamaterials is the assignment of distinct functions to different units, called meta-atoms or metamolecules, mimicking an intriguing property for light. When realizing negative index of refraction by metamaterials, for example, one may assign magnetic resonance to Cu SRRs and electric response to Cu thin wires [41]. In this way, light "feels" the medium consisting of these constituents as an effective medium. In other words, negative-refractive-index metamaterials are realized by controlling independently ε and μ. This independent control is caused by the absence of an intrinsic electronic interaction between effective ε and μ in the metamaterials. Even without the interaction, electromagnetic waves feel ε and μ combined together as a fictitious interaction: $n = \sqrt{\varepsilon}\sqrt{\mu}$ [42].

Let us examine another example, metamaterial perfect absorbers [97]. We define

T and R as transmission and reflection of electromagnetic waves, respectively. The absorption A is then calculated to be $A = 1 - T - R$. Hence, if $T = R = 0$ is obtained, A becomes unity, resulting in perfect absorption. Zero transmission is rather easy to be obtained. Contrastingly, $R = 0$ is tough to be achieved using natural materials because R is relevant to the wave impedance $\eta = \sqrt{\mu\mu_0/\varepsilon\varepsilon_0}$ and we cannot change μ and ε independently. However, metamaterials enable us to control independently effective μ and ε, leading to two media with different n but identical η, i.e., $R = 0$ and $A = 1$ [97, 98, 99]. This concept, independent control of materials parameters, is applicable in a broad range of physics in atoms, molecules, and condensed matter. Here we are going to import this concept into the MCh effect research via ξ and κ by decoupling, tuning, and integrating OA and the MO effect in one metamaterial.

In addition to the "job-sharing" in metamaterials, what we could learn from the metamaterials history aforementioned is that microwave metamaterials are good playgrounds for testing new physical concepts and phenomena, like the MCh effect. The reason is twofold: an intrinsic one and practical one. As the intrinsic reason, at microwave frequencies, metallic elements are perfect conductors so that electromagnetic losses, i.e., imaginary parts of effective ε and μ, are not dominant in propagations. Second, microwaves are practically human-scale electromagnetic waves. For example, the X-band microwave around a frequency of 10 GHz corresponds to wavelength of 30 mm in vacuum, which is very similar to the human scale. This enables us to manufacture the well-designed metamaterials. Therefore, we study the MCh metamaterials at microwave frequencies in this Review. Before moving on to the MCh metamaterials, we give brief reviews on metamaterials solely with magnetism in 2.5.2 and with chirality in 2.5.3.

2.5.2. Metamaterial with magnetism In this part we take a look at an quick overview of metamaterials with magnetism. The SRRs response to ac magnetic fields of electromagnetic waves, leading to magnetic resonances by structured nonmagnetic materials. In this way, the SRRs are usually referred to as magnetic metamaterials [118]. However, this is not the case in this part. Here metamaterials with magnetism are assigned to structured metamaterials consisting of ferromagnetic metals, for example, Fe, Ni, and FeNi alloy (permalloy; Py), or insulating ferro/ferrimagnet, for example, $Y_3Fe_5O_{12}$ (YIG) ferrite and $La_{0.89}Sr_{0.11}MnO_3$ (LSMO). Initially, the magnetic metamaterials have attracted interest from a view point of an alternative route to negative-refractive-index metamaterials without SRRs.

In magnetic materials, μ becomes intrinsically negative at the high frequency side of a ferromagnetic resonance (FMR) frequency of electron spins, normally in microwave region [119]. Since the FMR frequency is dependent on the external magnetic fields, metamaterials with magnetism are anticipated to bring about negative-refractive-index metamaterials with an operation frequency tunable by the external fields. The eddy current loss is, however, dominant in bulk ferromagnetic metal; the negative real part of μ is smeared out by the large imaginary part. Because the eddy
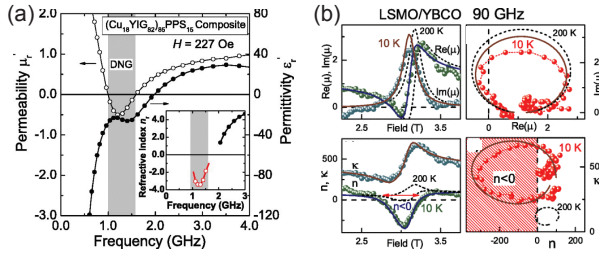
Figure 7. (a) Composite materials consisting of YIG and Cu granules. Reprinted from [131], with the permission of AIP Publishing. (b) Alternative multilayers of LSMO and YBCO layers. Reprinted figure with permission from [132], copyright (2005) by the American Physical Society.

current loss is inversely scaled with the magnetic metals volume, miniaturization is a possible address to suppress the eddy current losses. Therefore, composite and granular materials consisting of magnetic metal nanoparticles embedded in nonmagnetic insulating matrices have been considered theoretically to realize negative-refractive-index metamaterials at microwave frequency [120]. Indeed micromagnetics simulation indicated that negative μ was obtained by the Ni nanocomposites around FMR frequencies [121, 122, 123, 124]. The ferromagnetic composite materials consisting of nanoparticles were synthesized and studied using electron spin resonance and microwave transmission [125, 126, 127, 128, 129]. Moreover, it is theoretically predicted that exchange spin-wave resonances in thin magnetic films with surface pinning bring about the negative real part of μ at higher frequencies of several hundred GHz [130]. Nevertheless, the large imaginary part is still an issue.

Another possible address for suppressing the eddy current losses is insulating ferro/ferrimagnets with low electric conductivities. Composite materials consisting of YIG and Cu granules have reported to have negative μ and ε simultaneously at microwave frequencies under dc magnetic fields [131] as shown in Fig. 7(a). Moreover, as shown in Fig. 7(b), alternative multilayers of LSMO and superconducting $YBa_2Cu_3O_7$ (YBCO) under dc magnetic fields show both μ and ε to be negative value simultaneously for millimeter waves at 90 GHz [132]. Furthermore, magnetic composites consisting of gold nanoparticles embedded in YIG matrices [52, 133] are of interest from the view point of magnetoplasmonics [134].

Beside the above-mentioned researches on composite nanomaterials, the use of negative μ in ferrite materials [135, 136] was proposed to realize non-reciprocal negative-refractive-index metamaterials with the help of microwave circuit technologies. Non-reciprocal transmission lines with negative effective n were demonstrated by employing microstrip lines on a YIG polycrystalline substrate, which is magnetized perpendicular to the microwave propagation direction for the negative μ condition [137]. The microstrip lines consist of periodically loaded with series capacitances and shunt inductive stubs for the application to isolators. Even without insertion of the series capacitances [Fig. 8(a)], negative μ in the ferrite substrate supports wave propagation
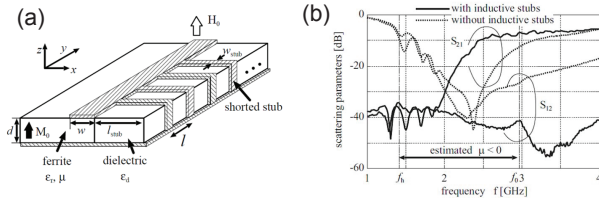
Figure 8. (a) Geometries of non-reciprocal negative-refractive-index transmission lines using normally magnetized ferrite microstrip lines without capacitances. (b) Measured S-parameters validating that the insertion of inductive stubs for negative ε creates a passband only for S_{21} in the single negative μ stopband due to the ferrite material. Reprinted figures with permission (17RA0048) from [138], copyright (2006) by IEICE.

1 along with inductive stubs for negative ε as shown in Fig. 8(b) [138].

2   Other configurations were based on a metallic rectangular waveguide periodically
3 loaded with transversely magnetized ferrite slabs and neighboring dielectric regions [139]
4 and a uniform ferrite waveguide with one side wall open, which supports a gap-less
5 forward and backward mode only in one propagation direction [140]. Several recent
6 works [141, 142, 143, 144, 145] on ferrite-based magnetic metamaterials were devoted to
7 controlling non-reciprocal phase gradient of the field profile for applications to antennas
8 and sensing technologies. Phase-shifting non-reciprocity enhancement [146, 147] and
9 optimal dispersion design, such as dispersion-less non-reciprocity [148] will open up new
10 applications of non-reciprocal metamaterials.

11 *2.5.3. Metamaterial with chirality* This part gives a brief review of metamaterials
12 with chirality. A prototype of chiral metamaterials that show OA for electromagnetic
13 radiation is known from the pioneering work using twisted fiber jute bundles by Bose
14 [149] in 1898. Chiral structures were studied in terms of helical antenna for radiation
15 [150] and model system using microwaves for understanding OA in chiral molecules
16 [151].

17   Modern chiral metamaterials or photonic crystal [152, 153, 154, 155, 156, 157]
18 with quasi-2D planar gammadion-shaped nanostructures showed giant optical activity
19 in visible [158] and near-IR region [159]. The giant polarization effect arises from the
20 light-matter interaction enhancement through surface plasmons. This planar chirality
21 is caused by the three-dimensional (3D) character of the structure, i.e., from the
22 presence of the air-metal and substrate-metal interfaces. Additionally, as shown in Fig.
23 9(a), circularly-polarized infrared light emission was observed from InAs quantum dots
24 embedded in the GaAs-based 2D chiral photonic crystal waveguide [160]. When the wave
25 impedance and wavenumber of the chiral medium composed of chiral meta-atoms are
26 equal to the corresponding parameters of vacuum, one of the circularly-polarized light
27 is transmitted to the medium without reflection or refraction for all angles of incidence;
28 that is to say, chiral vacuum [161], leading to a circular polarizing beam splitter.

29   Since OA is a first-order spatial dispersion effect originating from the non-local

light-matter interaction, a large 3D spatial variation in the chiral structures, like helices, is preferable for obtaining larger OA. Chiral metamaterials consisting of 3D gold helices arranged on a 2D square lattice were fabricated using direct laser writing into a photoresist followed by electrochemical gold deposition [162]. The structure blocks the circular polarization with the same handedness as the helices, whereas it transmits the other in a broadband, for a frequency range exceeding one octave in the few-μm wavelength range. To realize enantiomeric switching ability, a micro-electromechanical systems (MEMS) chiral metamaterial was demonstrated to be facilitated by a deformable 3D chiral structure with the ability to switch between mirror images as shown in Fig. 9(b) [163].

A new twist to the story of modern chiral metamaterials appeared in 2004. Pendry [164] suggested chiral metamaterials exhibiting strong OA as a potential candidate for achieving negative refraction. The refractive index becomes negative for one circular polarization even if both ε and μ have positive values [165]. There are several implementation of negative refraction using chiral metamaterial: by using circuit-board printing technology in GHz range [Fig. 9(c)] [166] and by employing standard lithographic technique in THz range [167].

3. Experiment on magnetochiral metamolecule for X-band microwave

In this section 3, we demonstrate our direct experimental observation of MCh effects at X-band microwave frequencies by a single metamolecule in waveguide at room temperature. Subsection 3.1 describes experimental procedures in metamolecule preparation and microwave measurement. After a brief introduction of microwave transmission spectra of chiral and magnetic meta-atoms in 3.2, we detail microwave transmission spectra by the MCh metamolecule under weak (3.3) and strong magnetic fields (3.5). Non-reciprocal refractive index difference due to the MCh effect under weak magnetic fields are evaluated in 3.4.

3.1. Sample preparation and microwave measurement

An MCh metamolecule has been embodied by using a Cu chiral structure (chiral meta-atom) and YIG ferrite rod/cylinder (magnetic meta-atom). Figure 10(a) shows a photograph of an MCh metamolecule in this study. A Cu wire 0.55 mm in diameter was coiled clockwise four times round the thread groove of the right-handed screw to form the right-handed Cu chiral meta-atom, as illustrated in the left part of Fig. 10(a). As shown in the right-hand side in Fig. 10(a), the cross-section and length of the ferrite rod were 1.5 mm × 1.5 mm and 15 mm, respectively. Note that a ferrite square pillar was replaced by a ferrite cylinder with diameter and length of 2 mm and 15 mm, respectively, in the measurements under strong magnetic field in 3.5. However, this change in the magnetic meta-atom shape does not affect the experimental results and underlying physics. The ferrite square/round pillars are well insulating. The magnetic
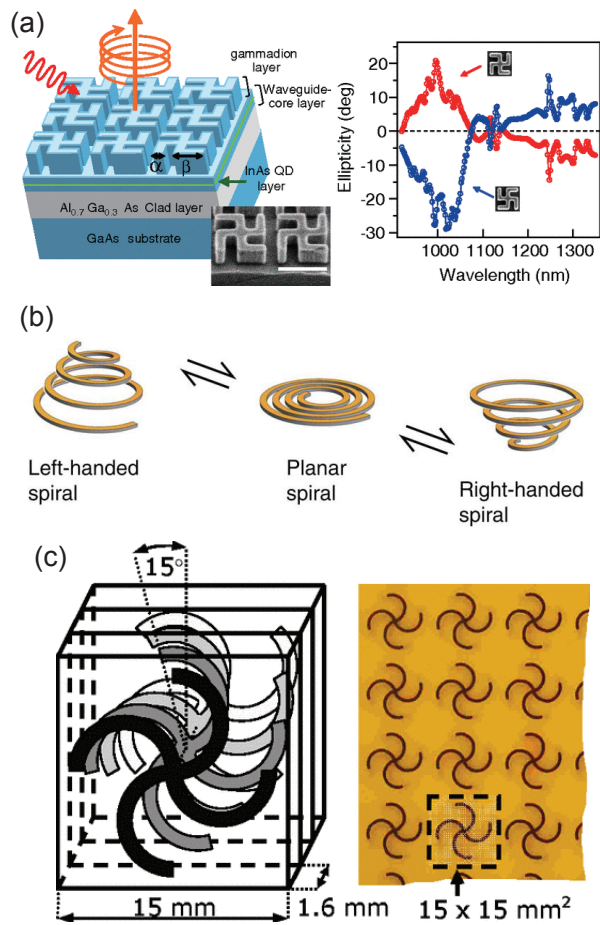
Figure 9. (a) Circularly-polarized infrared light emission observed from InAs quantum dots embedded in the GaAs-based 2D chiral photonic crystal waveguide. Reprinted figure with permission from [160], copyright (2011) by the American Physical Society. (b) MEMS spiral metamaterial from [163], copyright (2015) by Macmillan Publishers Ltd. (c) Chiral metamaterials as a candidate for achieving negative refraction. Reprinted figure with permission from [166], copyright (2009) by the American Physical Society.

meta-atom was inserted in the chiral meta-atom and the metamolecule was fixed in a thermal-contraction tube as shown in Fig. 10(a).

Figure 11 shows magnetization of the MCh metamolecule measured by a magnetometer as a function of the dc magnetic field applied in the direction parallel to the ferrite rod. Spontaneous magnetization and the soft magnetic nature of the ferrite rod in the metamolecule were observed. The magnetization is saturated by applying dc magnetic fields of approximately 50 mT.

A single metamolecule was put into a WR-90 waveguide, which was terminated at both ends by Agilent 281A adaptors. Microwave propagating direction is along parallel/anti-parallel to the chiral axis as illustrated in Fig. 10(b). Because ac magnetic fields of microwaves in the waveguide are parallel to the chiral axis of the MCh metamolecule, chiral resonance can be excited. Two adaptors were connected via the
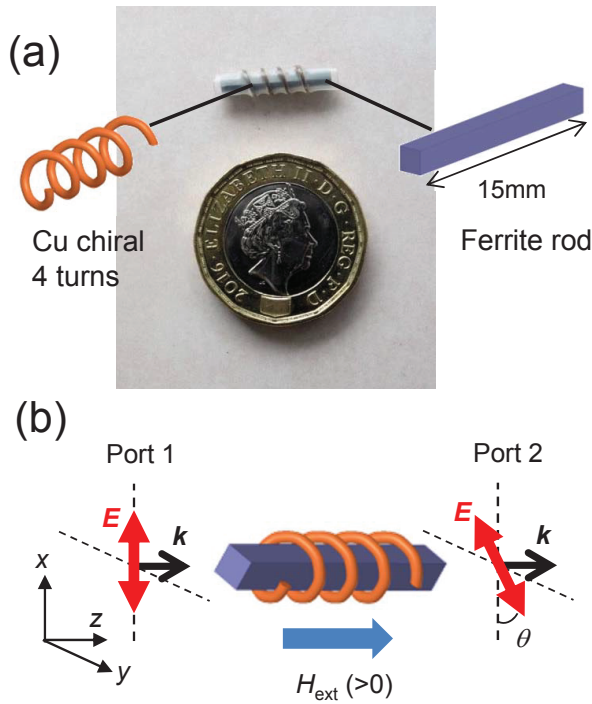
Figure 10. (a) Center: A photograph of the MCh metamolecule. Diameter of the coin in the photo is 23.1 mm. Illustrations of Cu chiral structure (left) and YIG ferrite rod (right). (b) A schematic of configurations in the microwave measurements of S_{21} of the MCh metamolecule.
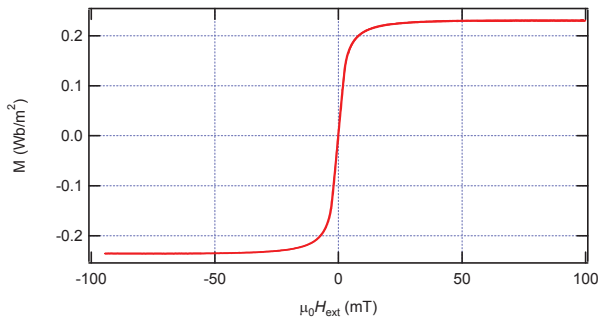
Figure 11. Magnetization of the MCh metamolecule as a function of the dc magnetic field applied in the direction parallel to the ferrite square rod.

waveguide so that the polarization plane of an electric field of the fundamental TE_{10} mode in an adaptor was parallel to that in the other adaptor. The sample in the waveguide was placed between two poles in an electromagnet. The dc magnetic fields $\mu_0 H_{ext}$ was applied up to $\pm$ 400 mT, which is enough to saturate magnetization of magnetic meta-atom, in a direction parallel/anti-parallel to the microwave propagation. The $\mu_0 H_{ext}$ was monitored by using a gauss meter equipped with a Hall element. The $\mu_0 H_{ext} > 0$ ($\mu_0 H_{ext} < 0$) corresponds to magnetic field direction from port 1 to port 2 (port 2 to port 1). An X-band microwave source was an Agilent PNA N5224
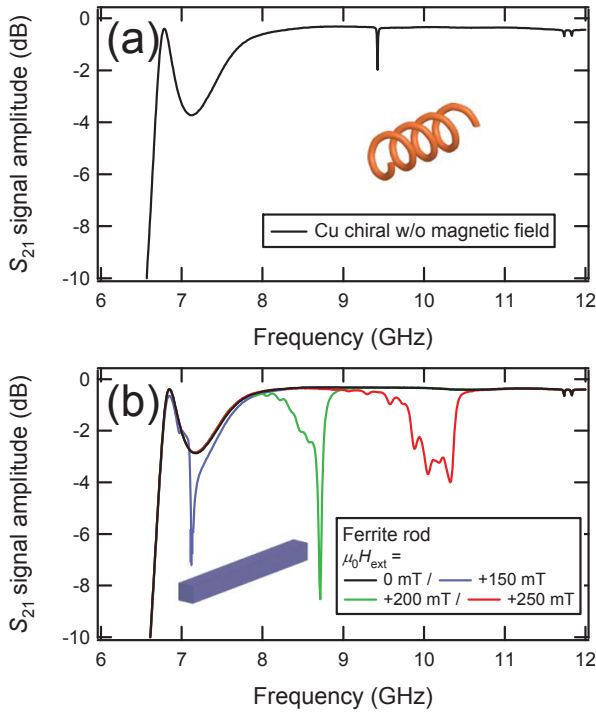
Figure 12. Transmission S_{21} amplitude spectra of (a) Cu chiral structure without the external magnetic field, and of (b) ferrite rod without the dc field (black), with + 150 mT (blue), + 200 mT (green), and + 250 mT (red). Reprinted figure with permission from [44], copyright (2014) by the American Physical Society.

1 vector network analyzer. We measured S-parameters of S_{21} and S_{12} corresponding
2 respectively to transmission coefficients from port 1 to port 2 and from port 2 to port
3 1, simultaneously. All measurements were carried out at room temperature.

4 *3.2. Transmission spectrum of meta-atom*

5 Figure 12(a) shows an amplitude spectrum of S_{21} in frequencies between 6 to 12 GHz
6 through only the Cu chiral meta-atom without the dc magnetic field. The measurements
7 are valid in the pass-band above 6.6 GHz, which is the cut-off frequency of the waveguide.
8 We observe a notch at 9.4 GHz, which is traced back to resonance of the chiral meta-
9 atom. The chiral meta-atom rotates the polarization plane of electric field of microwaves
10 and the microwaves do not transmit due to the parallel configuration of the adaptors
11 at the end of the waveguide. In this way, the chiral meta-atom gives rise to the optical
12 activity and enhances the activity by resonance [168]. The spectrum for the chiral
13 meta-atom under the applied magnetic field is the same as that shown in Fig. 12(a).

14   Amplitude spectra of S_{21} of the YIG ferrite magnetic meta-atom are shown in Fig.
15 12(b). Without the external dc magnetic field, a feature-less spectrum (black curve) is
16 obtained between 7 to 12 GHz. Contrastingly, a large notch emerges at 7.1 GHz when
17 the dc field of + 150 mT is applied in a direction parallel to the ferrite rod by using the
18 electromagnet (blue curve). This notch shifts to a higher frequency at approximately
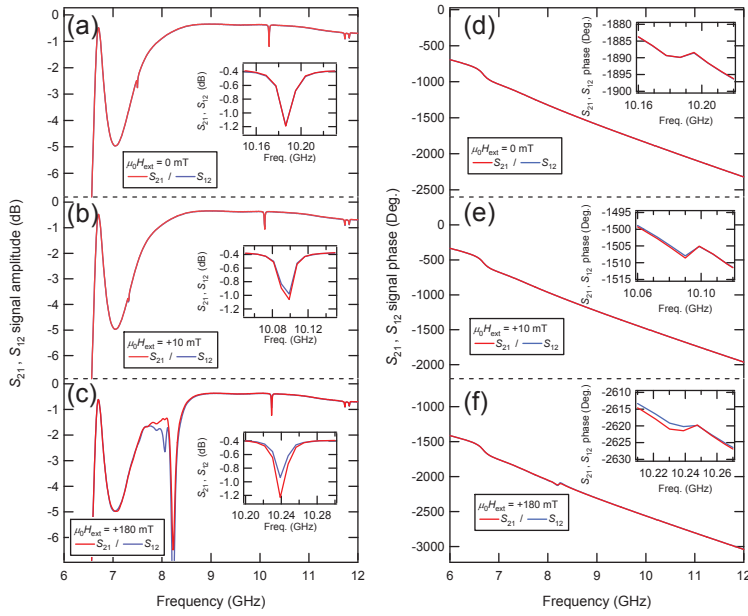
Figure 13. Transmission S_{21} (red) and S_{12} (blue) amplitude spectra (a)-(c) and phase spectra (d)-(f) of the single MCh metamolecule under the external dc magnetic fields of 0 mT [(a) and (d)], + 10 mT [(b) and (e)], and + 180 mT [(c) and (f)]. Insets: enlarged spectra at the resonant optical activity around 10 GHz. Reprinted figure with permission from [44], copyright (2014) by the American Physical Society.

8.7 GHz and 10.3 GHz, with an increase in the magnetic field to + 200 mT (green curve) and + 250 mT (red curve), respectively. The features shifting upward with an increase in the magnetic field originate from FMR due to precession of electron spins in the YIG ferrite magnetic meta-atom.

3.3. MCh effect under weak magnetic field

By combining the Cu chiral meta-atom with the YIG ferrite magnetic meta-atom, and applying the dc magnetic field, we can break both space-inversion and time-reversal symmetries. This simultaneous breaking leads to emergence of the MCh effects as demonstrated in Fig. 13. Figures 13(a)-13(c) show amplitude spectra of S_{21} (red curves) and S_{12} (blue curves) of the metamolecule under the dc magnetic fields of 0 mT, + 10 mT, and + 180 mT, respectively. Figures 13(d)-13(f) are corresponding phase spectra. At 0 mT, we observe a salient notch at 10.2 GHz and additional weak notch at 7.5 GHz in Fig. 13(a). The phase spectra in Fig. 13(d) show weak dispersion-type features at these frequencies. These are resonant optical activities due to the Cu chiral meta-atom. The signals show a dispersion-type shape in the phase spectra due to the Kramers-Kronig relation. The insets in Figs. 13(a) and 13(d) correspond to enlarged spectra at the resonant optical activity at approximately 10 GHz. The inset clearly shows that S_{21} and S_{12} spectra are identical at 0 mT, namely in the presence of the time-reversal symmetry.

1   The MCh effect is manifest in the difference of the transmission amplitude and
2   phase spectra, i.e., difference between S_{21} and S_{12} spectra. Indeed, with the applied
3   dc magnetic field of + 10 mT, transmission S_{21} (red) and S_{12} (blue) spectra at the
4   resonant optical activity are not identical in the inset in Figs. 13(b) and 13(e), whether
5   the incident directions of microwaves are parallel or anti-parallel to the dc magnetic
6   field. This is an emergence of the MCh effect by the metamolecule. Notably FMR is
7   located at a very low frequency of about 1 GHz for + 10 mT. Nevertheless, a finite
8   difference between S_{21} and S_{12} spectra is observed at the resonant optical activity in
9   Figs. 13(b) and 13(e).

10   Figures 13(c) and 13(f) show transmission S_{21} (red) and S_{12} (blue) spectra with the
11   dc field of + 180 mT. We notice in the inset that the difference in the spectra around 10
12   GHz increases. Additionally, complicated features due to FMR in the ferrite magnetic
13   meta-atom emerge at approximately 8 GHz, which shifts to a higher frequency with a
14   further increase in the dc field. The MCh effect manifests itself in a significant difference
15   in amplitude and phase spectra between S_{21} and S_{12} at the FMR frequency in Fig. 13(c).
16   The significant difference due to FMR is investigated in detail in 3.5. Therefore in this
17   part, we focus on the MCh effects at the resonant optical activity around 10 GHz.

18   Further evidence of the MCh effects by the metamolecule is shown in Fig. 14.
19   Plotted are differences in phases [Fig. 14(a)] and amplitudes [Fig. 14(b)] between S_{21}
20   and S_{12} under dc magnetic fields from 0 mT to ±200 mT. In Fig. 14(a), a feature-less
21   spectrum is obtained with 0 mT (black line). With + 1 mT, a signal with Lorentz-type
22   dispersion due to the MCh effect emerges at a frequency of the resonant optical activity
23   around 10 GHz. Interestingly, a very weak magnetic field of + 1 mT is enough to
24   induce the MCh effects. The MCh effect around 10 GHz becomes large and shifts with
25   an increase in the magnetic field. Differential spectra for the reversed direction of the
26   external dc magnetic field ($H_{ext} < 0$) are also shown in the lower half of Fig. 14. The
27   appearance and frequency shift of the MCh effects are very similar to those in $H_{ext} > 0$,
28   while the polarity of MCh effects is flipped with the direction of the magnetic field.

29   *3.4. Refractive index difference*

30   In Fig. 15(a), we plotted the phase difference $\Delta\phi$ due to the MCh effect evaluated as
31   a half value of the peak-to-peak variation at the resonant optical activity around 10
32   GHz in Fig. 14(a), as a function of $\mu_0 H_{ext}$. In Fig. 15(b), the amplitude difference ΔI
33   is also plotted. Orange (green) marks correspond to the MCh effects under $H_{ext} > 0$
34   ($H_{ext} < 0$). The MCh effects appear at 1 mT, rapidly grow with the magnetic field up to
35   10 mT, and monotonically increase with the magnetic field. It is reasonable to consider
36   that the MO effect is proportional to the effective magnetization of the metamolecule
37   [169]. Under the unsaturated regime, the magnetization is a function of the applied dc
38   magnetic field. A rapid increase in the MCh effects at a very low magnetic field below
39   10 mT is thus caused by the soft magnetic nature of the magnetic meta-atom in the
40   metamolecule that was observed in Fig. 11. Given Figs. 11 and 15, we notice that the
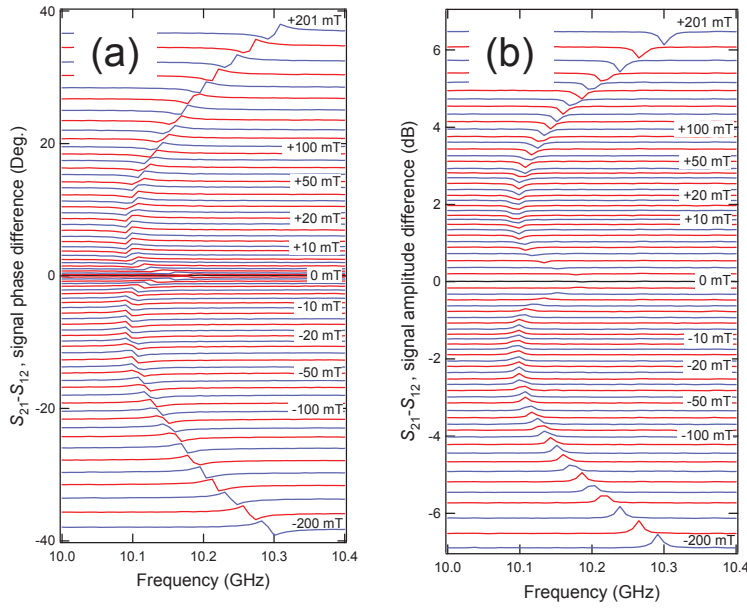
Figure 14. Differences in (a) phases and (b) amplitudes between S_{21} and S_{12} around 10 GHz of the MCh metamolecule under dc magnetic fields from 0 mT to ± 200 mT. Reprinted figure with permission from [44], copyright (2014) by the American Physical Society.

MCh effects increase as $\mu_0 H_{\text{ext}}$ is further increased after the magnetization saturation. The increase in the MCh effects after the saturation is likely to be caused by an increase in the effective μ in the WR-90 waveguide due to the magnetic resonance, which will be discussed in 5.2.

We evaluate the difference in refractive indices obtained by the MCh effects. The phase and amplitude differences in the transmission coefficients, as shown in Fig. 15, can be converted to the non-reciprocal differences in the real and imaginary parts of refractive indices $\Delta n'$ and $\Delta n''$, respectively. Given that the one-dimensional structure is composed of the single metamolecule inserted in a rectangular waveguide, we describe $\Delta n'$ and $\Delta n''$ between forward (S_{21}) and reverse (S_{12}) propagations of unpolarized waves as

$$\Delta n = n_{1 \to 2} - n_{2 \to 1} = \Delta n' + i \Delta n''. \tag{22}$$

Δn is a Lorentz-type function of the operational frequency, and is relevant to the phase and amplitude of the complex transmission coefficients as follows,

$$\Delta n' = -\frac{c}{2\pi f l} \Delta \phi \simeq -47.7 \times \frac{\Delta \phi}{f l}, \tag{23}$$

$$\Delta n'' = -\frac{c}{40\pi (\log_{10} e) f l} \Delta I \simeq -5.50 \times \frac{\Delta I}{f l}, \tag{24}$$

where $\Delta \phi$ denotes the phase difference $\angle S_{21} - \angle S_{12}$ in radian, and ΔI denotes the amplitude difference $|S_{21}| - |S_{12}|$ in decibel at the MCh effects. The frequency f is
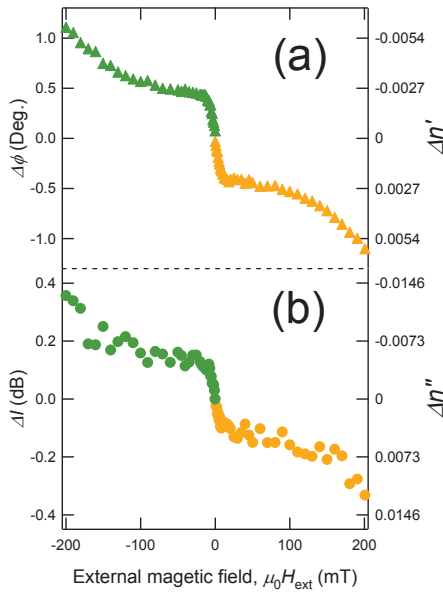
Figure 15. Differences in (a) phases and (b) amplitudes are plotted as a function of $\mu_0 H_{\text{ext}}$. Evaluated differences in the index of refraction are also indicated from the right axes. Reprinted figure with permission from [44], copyright (2014) by the American Physical Society.

1 measured in GHz, and l represents the total length of the metamolecule measured in
2 millimeters.

3   At $+ 200$ mT, Figs. 15(a) and 15(b) show that the maximum values of $\Delta\phi$ and ΔI
4 were $\Delta\phi \sim - 1.0$ degree $= - 0.017$ radian and $\Delta I \sim - 0.4$ dB. From Eqs. (22)-(24), with
5 $l = 15$ mm and $f = 10$ GHz, we evaluated $\Delta n' \simeq 5.4 \times 10^{-3}$ and $\Delta n'' \simeq 1.5 \times 10^{-2}$ maxima
6 as indicated from the right axes of Figs. 15(a) and 15(b). In the present experiment,
7 we have succeeded in directory observing the MCh effects thanks to several advantages
8 for the MCh metamolecule in microwave regions: the optical activity is enhanced in the
9 Cu chiral meta-atom [168], the magnetic response of the ferrite magnetic meta-atom is
10 large in microwave regions [145], and the microwave phase and amplitude are directly
11 measured using the network analyzer. The manifestation of the real part of the non-
12 reciprocal index difference $\Delta n'$ and the monotonic increase with the applied magnetic
13 field verifies the MCh effect. The values of $\Delta n'$ and $\Delta n''$ of the single metamolecule
14 are not yet considerably large. However, by using resonances in the meta-atoms, much
15 larger MCh effects are expected as observed in the next subsection.

16 *3.5. MCh effect under strong magnetic field*

17 Previously we observed MCh effects for the X-band microwaves by a single metamolecule
18 under weak dc magnetic fields below 200 mT. However, interaction of the chiral
19 resonance by the Cu chiral meta-atom with FMR by the ferrite magnetic meta-atom
20 remains to be addressed. By applying strong magnetic fields up to 400 mT, the magnetic
21 meta-atom FMR frequency approaches the chiral resonance frequencies. This motivates
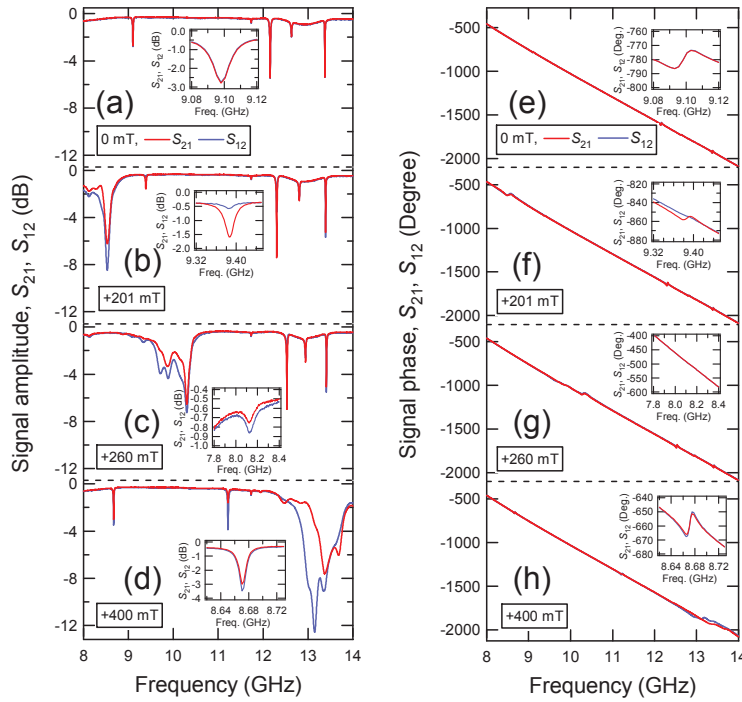
Figure 16. Transmission S_{21} (red curves) and S_{12} (blue curves) amplitude spectra (a)-(d) and phase spectra (e)-(h) of single MCh metamolecule under external dc magnetic fields of 0 mT [(a) and (e)], + 201 mT [(b) and (f)], + 260 mT [(c) and (g)], and + 400 mT [(d) and (h)]. Insets illustrate enlarged spectra for S_{21} (red) and S_{12} (blue) of chiral resonance originally appeared at 9.1 GHz. Reprinted figure with permission from [45], copyright (2017) by the American Physical Society.

1   a further enhancement of the MCh effects.

2   Figures 16(a)-16(d) illustrate transmission amplitude spectra for S_{21} (red curves)
3   and S_{12} (blue curves) of the metamolecule at various magnetic fields. Figures 16(e)-
4   16(h) are corresponding phase spectra. Note that a YIG ferrite cylinder with diameter
5   and length of 2 mm and 15 mm, respectively, was utilized as a magnetic meta-atom
6   in the measurements. In Fig. 16(a), when $\mu_0 H_{\text{ext}} = 0$ mT, we observe salient dips
7   at 9.1, 12.2, and 13.4 GHz. Additional small dip is observed at 12.6 GHz. The dips
8   are traced back to chiral resonances corresponding to enhanced optical activities due
9   to resonance in the chiral meta-atom. The inset shows enlarged spectra for S_{21} (red)
10 and S_{12} (blue) at the chiral resonance at approximately 9 GHz. When $\mu_0 H_{\text{ext}} = 0$ mT,
11 the S_{21} spectrum is identical with the S_{12} spectrum at the chiral resonance frequency.
12 Phase spectra exhibit dispersion-type signals at the chiral resonance when $\mu_0 H_{\text{ext}} = 0$
13 mT although they are too weak to be observed in Fig. 16(e). The inset corresponds to
14 the enlarged phase spectra for S_{21} (red) and S_{12} (blue) around 9.1 GHz. The S_{21} and
15 S_{12} phase spectra are identical when $\mu_0 H_{\text{ext}} = 0$ mT as well as amplitude spectra.

16   When applying $\mu_0 H_{\text{ext}}$ of + 201 mT [Fig. 16(b)], an appearance of another large
17 dip is seen at 8.5 GHz. The dispersion-type signal is exhibited in corresponding phase
18 spectra [Fig. 16(f)]. The signals are shifted to higher frequencies as $\mu_0 H_{\text{ext}}$ is increased.

1 In this way, the signals are traced back to FMR in the ferrite magnetic meta-atom. In
2 Fig. 16(b), S_{21} (red) and S_{12} (blue) highlight a difference at FMR; the blue dip is much
3 deeper than the red one, indicating the MCh effect due to FMR. Notably, the MCh
4 effect can be obtained by FMR even in the absence of the chiral resonance since the
5 space-inversion symmetry of the system is broken.

6 The appearance of FMR is accompanied by slight shifts of the chiral resonances.
7 Moreover, as shown in the insets in Figs. 16(b) and 16(f), S_{21} and S_{12} spectra at the
8 chiral resonance at approximately 9 GHz are not identical due to MCh effects. In Fig.
9 16(b), the dips in S_{21} (red) at signals at approximately 9 GHz is deeper than those in
10 S_{12} (blue).

11 When $\mu_0 H_{ext}$ is further increased up to $+ 260$ mT as shown in Figs. 16(c) and 16(g),
12 FMR moves to approximately 10 GHz and overtakes the chiral resonance originally
13 at 9.1 GHz. Notably in the inset of Fig. 16(c), the chiral resonance appears at a
14 lower frequency approximately 8.1 GHz after being passed by FMR. Interestingly, as
15 demonstrated in the inset, dip in S_{12} (blue) is deeper than that in S_{21} (red), indicating
16 that the MCh effect at the chiral resonance flips the polarity.

17 As $\mu_0 H_{ext}$ is increased up to $+ 400$ mT as shown in Figs. 16(d) and 16(h), FMR
18 shifts to a higher frequency at approximately 13 GHz and demonstrates very large MCh
19 effect. After overtaking by FMR, the chiral resonance originally at 12.2 GHz is shifted
20 to a lower frequency of 11.2 GHz. The chiral resonance at a lower frequency moves to
21 a higher frequency of 8.7 GHz, which is close to the initial frequency of the signal.

22 Figure 17 demonstrates differences between S_{21} and S_{12}, i.e., MCh signals in phases
23 at various magnetic fields from 0 mT to ± 400 mT. Figure 18 shows corresponding
24 amplitude difference spectra. A feature-less spectrum is obtained with $\mu_0 H_{ext} = 0$ mT
25 (a black line). The upper halves of Figs. 17 and 18 highlight signals due to MCh effects
26 with $\mu_0 H_{ext} > 0$. When $\mu_0 H_{ext} = + 11$ mT in Fig. 17, a weak dispersion-type signal due
27 to the chiral resonance emerged at 8.9 GHz. A dip is observed at the same frequency
28 in Fig. 18. An increase in $\mu_0 H_{ext}$ leads to a blue shift of the MCh signal at the chiral
29 resonances.

30 When $\mu_0 H_{ext} = + 201$ mT, the MCh effect due to FMR appears at approximately
31 8.5 GHz in Figs. 17 and 18. As $\mu_0 H_{ext}$ is increased, the signal shifts to higher frequencies
32 and becomes larger. Under $\mu_0 H_{ext} = + 250$ mT, FMR is overlapped with the chiral
33 resonance, causing a disappearance in the chiral resonance. At $\mu_0 H_{ext} = + 280$ mT, a
34 signal is observed at approximately 8.3 GHz, a slightly lower frequency below 9 GHz.
35 The signal polarity of the MCh effect due to the chiral resonance is inverted. The
36 MCh signal due to the other chiral resonance shows a very similar behavior. These
37 results indicate that, after being passed by FMR, the chiral resonance jumps to a lower
38 frequency and the polarity of the MCh effect at the chiral resonance frequencies is
39 inverted. The MCh signals due to FMR in Figs. 17 and 18 become significantly large
40 at $+ 400$ mT.

41 Differential spectra for the reversed direction of the external dc magnetic field
42 ($\mu_0 H_{ext} < 0$) are also illustrated in the lower halves of Figs. 17 and 18. While the
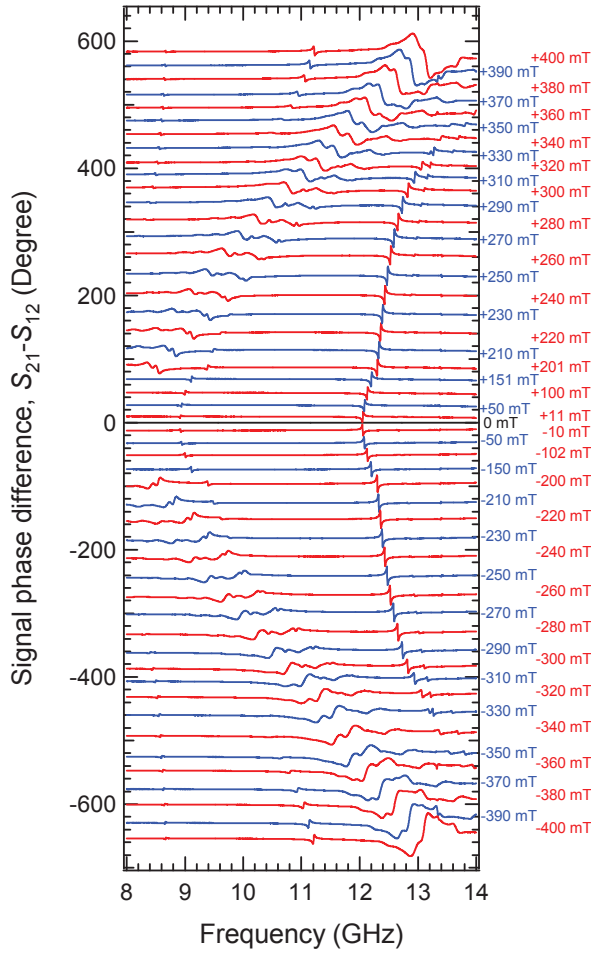
Figure 17. Differences in phase between S_{21} and S_{12} from 8 GHz to 14 GHz of MCh metamolecule under dc magnetic fields from 0 mT to ± 400 mT. Reprinted figure with permission from [45], copyright (2017) by the American Physical Society.

1 appearance and frequency shift of MCh signals are very similar to those in $\mu_0 H_{ext} > 0$,
2 the polarity is flipped with the direction of the magnetic field. Figures 17 and 18
3 demonstrate that the signals at FMR and chiral resonances are odd with respect to
4 $\mu_0 H_{ext}$.

5   The MCh effect due to FMR brings about the maximum values of phase and
6 amplitude differences as 20.8 degree and 9.11 dB, respectively, experimentally observed
7 at approximately 13 GHz under $\mu_0 H_{ext} = + 400$ mT . In the present experiments, from
8 Eqs. (22)-(24) with $l = 15$ mm and $f = 13$ GHz, we evaluated $\Delta n' \simeq -8.9 \times 10^{-2}$ and
9 $\Delta n'' \simeq -2.6 \times 10^{-1}$ maxima at $\mu_0 H_{ext} = + 400$ mT. The previous subsection reported
10 that $\Delta n' \simeq 5.4 \times 10^{-3}$ and $\Delta n'' \simeq 1.5 \times 10^{-2}$ maxima at $\mu_0 H_{ext} = + 200$ mT in the
11 MCh effect by the chiral resonances under lower dc magnetic fields. Thus the MCh effect
12 enhanced by FMR is one order magnitude greater than that by the chiral resonances.
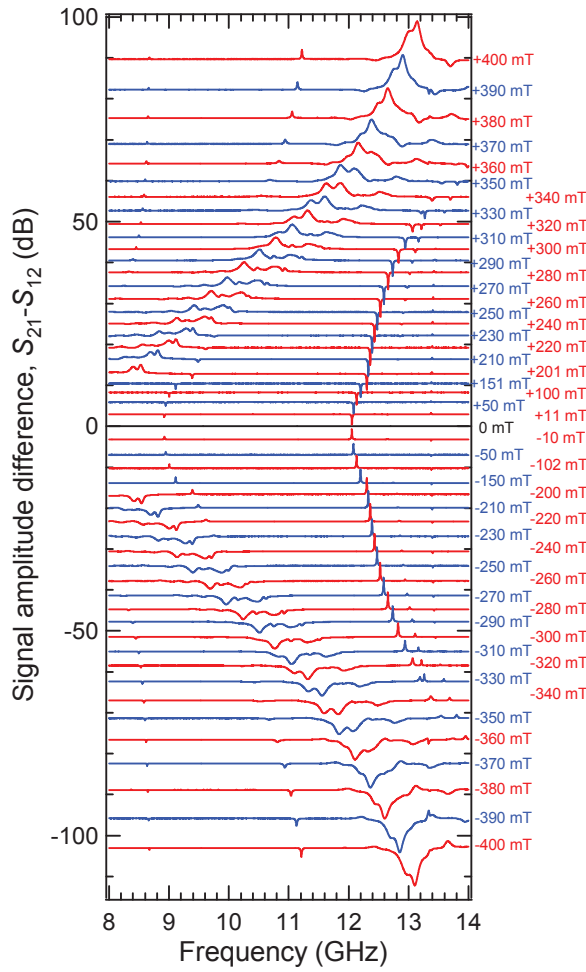
Figure 18. Differences in amplitude between S_{21} and S_{12} from 8 GHz to 14 GHz of MCh metamolecule under dc magnetic fields from 0 mT to ± 400 mT. Reprinted figure with permission from [45], copyright (2017) by the American Physical Society.

4. Numerical calculation

In this section 4, we conduct numerical simulation to reproduce the experimental results. External magnetic fields and direction dependence is investigated numerically in 4.2. Furthermore, MCh signals at a much higher magnetic field are addressed. Subsection 4.3 is devoted to studies for chirality dependence of the MCh signals.

4.1. Numerical setup

We performed numerical calculations based on a finite element method by a commercial software (COMSOL MULTIPHYSICS). Figure 19 illustrates the calculation configuration. The metamolecule is placed at the center of a WR-90 waveguide filled with air. The structural parameters of the metamolecule and the waveguide are identical to those in the experiments. The surfaces of the chiral meta-atom and the waveguide are set to be perfect electric conductors. Both ports of the waveguide are terminated
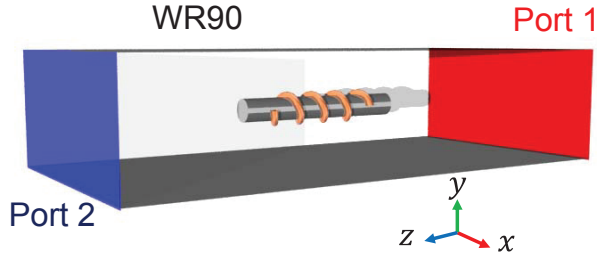
Figure 19. Setup for numerical calculation. Metamolecule is put at the center of WR-90 waveguide. The waveguide is terminated with perfectly matched layers.

with perfectly matched layers.

We implemented the material parameters for the ferrite cylinder as follows. The ε of the ferrite is set to $14.5 + 0.0029i$ [170]. When an external dc magnetic field is applied in the $+z$-direction, the ferrite with $\hat{\mu}$ is magnetized in the $+z$-direction as Eq. (4), where

$$\kappa = i\chi^{\mathrm{m}}_{xy}, \tag{25}$$

$$\mu_{xx} = \mu_{yy} = \mu = 1 + \chi^{\mathrm{m}}_{xx}, \tag{26}$$

$$\mu_{zz} = \mu_0. \tag{27}$$

On the off-diagonal component, κ is proportional to the external magnetic field and gives the MO activities such as the Faraday effect.

The magnetic susceptibility tensor χ^{m} is given by

$$\chi^{\mathrm{m}}_{xx} = \frac{\omega_0\omega_{\mathrm{m}}\left(\omega_0^2 - \omega^2\right) + \omega_0\omega_{\mathrm{m}}\omega^2\alpha^2}{[\omega_0^2 - \omega^2(1+\alpha^2)]^2 + 4\omega_0^2\omega^2\alpha^2} + i\frac{\alpha\omega\omega_{\mathrm{m}}[\omega_0^2 + \omega^2(1+\alpha^2)]}{[\omega_0^2 - \omega^2(1+\alpha^2)]^2 + 4\omega_0^2\omega^2\alpha^2} \tag{28}$$

$$\chi^{\mathrm{m}}_{xy} = \frac{2\omega_0\omega_{\mathrm{m}}\omega^2\alpha}{[\omega_0^2 - \omega^2(1+\alpha^2)]^2 + 4\omega_0^2\omega^2\alpha^2} - i\frac{\omega\omega_{\mathrm{m}}[\omega_0^2 - \omega^2(1+\alpha^2)]}{[\omega_0^2 - \omega^2(1+\alpha^2)]^2 + 4\omega_0^2\omega^2\alpha^2} \tag{29}$$

where $\omega_0 = \gamma\mu_0 H_{\mathrm{ext}}$, $\omega_{\mathrm{m}} = \gamma\mu_0 M_{\mathrm{s}}$, and $\alpha = \gamma\mu_0\Delta H/(2\omega)$. Here, ω_0 is the Larmor frequency at $\mu_0 H_{\mathrm{ext}}$. The Larmor frequency at the saturation magnetization M_{s} is ω_{m}. The loss factor, or the Gilbert damping factor, of the ferrite is α, and the corresponding line width is ΔH. The gyromagnetic ratio of the electron is γ. Note that we used the specific parameters for the ferrite from the literature [170]; the material parameters of the ferrite used in our numerical calculation are not the same as those in the experiment. The difference in the parameters between the experiment and the numerical calculation influences the resonance frequencies. However, it does not affect the physics behind the phenomena. Under these conditions, we calculated transmission coefficients, S_{21} and S_{12}, of microwaves with TE_{10} mode.

4.2. External magnetic field strength and direction dependence

Figure 20(a) shows the calculated differential spectra in phase between S_{21} and S_{12} of the MCh metamolecule under various $\mu_0 H_{\mathrm{ext}}$. Figure 20(b) shows the corresponding amplitude spectra. The $\mu_0 H_{\mathrm{ext}}$ was varied from $+ 100$ mT to $+ 600$ mT with steps of
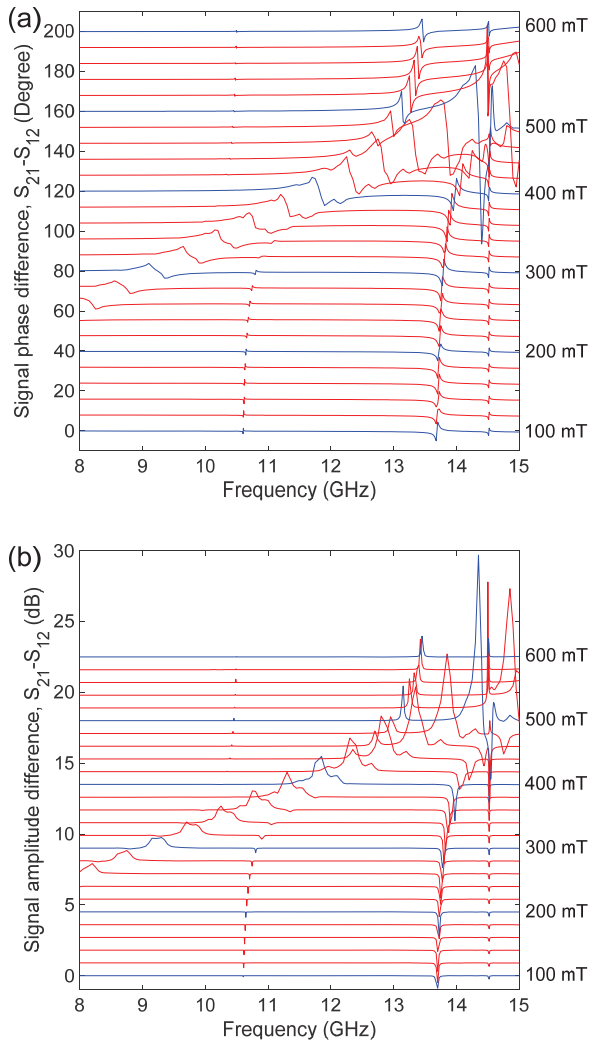
Figure 20. Differences between S_{21} and S_{12} in calculated (a) phase and (b) amplitude spectra for MCh metamolecule in range from 8 GHz to 15 GHz under dc magnetic fields from + 100 to + 600 mT. Reprinted figure with permission from [45], copyright (2017) by the American Physical Society.

1 20 mT. The chirality of the chiral meta-atom is set to be right-handed, which is the
2 same as the experiments. While we show spectra only with $\mu_0 H_{ext} > 0$ in Fig. 20, flip
3 in magnetic field direction ($\mu_0 H_{ext} < 0$) causes the polarity reversal in the spectra very
4 similar to the experimental results in Figs. 17 and 18.

5   The spectra in Figs. 20(a) and (b) highlight three features. The first feature is an
6 MCh signal with broad linewidth, for example, at approximately 9 GHz with $\mu_0 H_{ext} =$
7 + 300 mT, due to FMR of the ferrite meta-atom in the metamolecule. This signal shifts
8 to a higher frequency and becomes larger as $\mu_0 H_{ext}$ is increased.

9   The second is MCh signals with narrow linewidth at approximately 10.6 and
10 13.7 GHz when $\mu_0 H_{ext} =$ + 100 mT, which are due to the chiral resonances in the
11 metamolecule. As $\mu_0 H_{ext}$ is increased and FMR of the ferrite magnetic meta-atom

approaches to the chiral resonance, the signals due to chiral resonances slightly shift to higher frequencies. The MCh signals flip the polarity after being passed by FMR. These two features are very similar to those observed in the experiment [Figs. 17 and 18].

The last feature is an MCh signal with narrow linewidth at approximately 14.5 GHz in Fig. 20. This signal is associated with the chiral resonance. The behavior of the signal is, however, quite different from those of other chiral resonances at lower frequencies. The signal does not shift to a higher frequency as $\mu_0 H_{\text{ext}}$ is increased. More importantly, the MCh signal is strongly enhanced as FMR approaches under $\mu_0 H_{\text{ext}} = + 500$ mT. Notably, this signal is not observed in the experiment [Figs. 17 and 18] and predicted first by the numerical simulation.

In order to investigate the strong enhancement of the MCh signal in more detail, we carried out numerical calculations with varying $\mu_0 H_{\text{ext}}$ in the vicinity of $+ 500$ mT. Figure 21(a) shows the calculated phase difference of S_{21} and S_{12} as $\mu_0 H_{\text{ext}}$ is varied from $+ 495$ to $+ 510$ mT with steps of 5 mT. Figure 21(b) shows the corresponding amplitude spectra. The non-reciprocity signal is extremely enhanced with $\mu_0 H_{\text{ext}}$ of $+ 505$ mT. Additionally, in Fig. 21(b), the symmetric dispersive shape of the signal under 495 mT transforms to the asymmetric peak shape under $+ 505$ mT. Figures 21(a) and 21(b) demonstrate that, when $\mu_0 H_{\text{ext}} = + 505$ mT, the phase and amplitude differences at 14.446 GHz are evaluated to be 166.8 degree and 48.26 dB, respectively. These values correspond to $\Delta n' \simeq -6.6 \times 10^{-1}$ and $\Delta n'' \simeq 1.26$.

In order to show the external magnetic field dependence of the spectra more clearly, we illustrate the pseudo color plot for the calculated differences in phase spectra between S_{21} and S_{12}. In Fig. 22, the pseudo color plot of $\log[|\arg(S_{21}) - \arg(S_{12})|]$ is shown in order to make weak chiral resonances more visible. The vertical axis is the frequency in the range from 8 to 15 GHz, whereas the horizontal axis is $\mu_0 H_{\text{ext}}$ from $+ 100$ to $+ 600$ mT. We find three chiral resonances at 10.6, 13.7, and 14.5 GHz together with FMR, of which the frequency depends linearly on $\mu_0 H_{\text{ext}}$. The pseudo color plot demonstrates that the chiral resonances have anti-crossing features in the vicinity of FMR of the ferrite magnetic meta-atom. The anti-crossing nature of the chiral resonances initially at 10.6 and 13.7 GHz is caused by the hybridization with FMR [171]. Contrastingly, the pseudo color plot in Fig. 22 highlights that the chiral resonance at approximately 14.5 GHz is independent of $\mu_0 H_{\text{ext}}$ and does not show an anti-crossing feature. The origin of the giant MCh effect is addressed using the eigenmode analysis in 5.3.

4.3. Chirality dependence

We investigate the chirality dependence of the MCh signals numerically, since it is difficult to prepare enantiometric chiral meta-atoms reproducibly and precisely in experiments. In the calculation, the metamolecule chirality was switched by changing the chirality of the chiral meta-atom. Figure 23(a) illustrates the amplitude difference spectra between S_{21} and S_{12} of the metamolecule with the right-handed chiral meta-atom, while Fig. 23(b) illustrates those of the metamolecule with the left-handed chiral
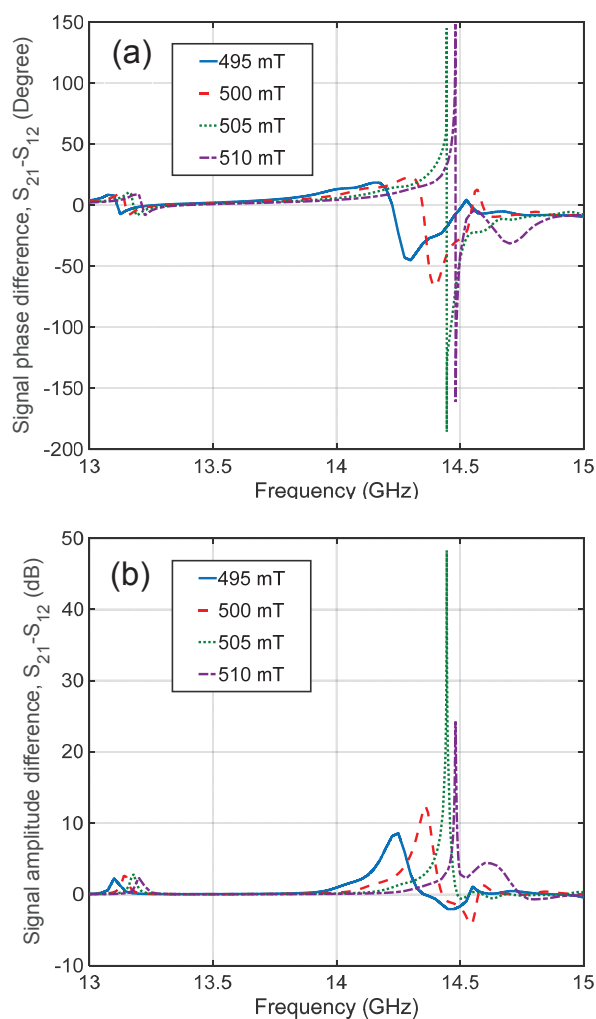
Figure 21. Calculated differential spectra between S_{12} and S_{21} of (a) phase and (b) amplitude in vicinity of $\mu_0 H_{\text{ext}} = +500$ mT. The $\mu_0 H_{\text{ext}}$ is varied from $+495$ to $+510$ mT with steps of 5 mT. Reprinted figure with permission from [45], copyright (2017) by the American Physical Society.

1 meta-atom. In these figures, $\mu_0 H_{\text{ext}}$ is increased from $+100$ to $+600$ mT with steps
2 of 50 mT. Figures 23(a) and 23(b) show that the sign of the MCh response at the
3 chiral resonance frequency of 10.6 GHz flips its polarity depending on the meta-atom's
4 chirality. Furthermore, the MCh signal polarity due to FMR, e.g., at 10.5 GHz under
5 $\mu_0 H_{\text{ext}} = +350$ mT, also depends on the chirality. The polarity of phase differential
6 spectra also flips depending on the chirality of the chiral meta-atom (not shown here).
7   Through this calculation, we confirmed that the MCh signal was odd with respect
8 to the chirality. The signal is also odd with respect to the external magnetic field.
9 Furthermore, neither only chiral meta-atom nor magnetic meta-atom exhibited MCh
10 signals in the numerical calculation although not shown here. We also confirmed in
11 the numerical calculation that $\hat{\mu}$ without the off-diagonal parts (i.e., $\kappa = 0$) of the
12 metamolecule resulted in an absence of the MCh signals. These chirality and magnetic
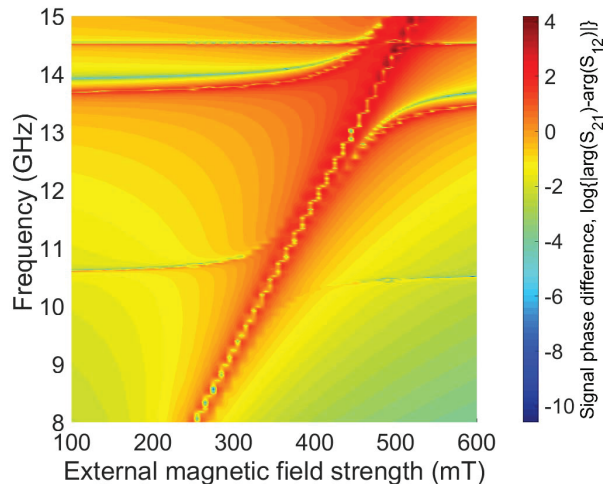
Figure 22. Pseudo color plot for difference between S_{21} and S_{12} in calculated phase in range from 8 GHz to 15 GHz. The $\mu_0 H_{\text{ext}}$ is varied from + 100 to + 600 mT. Reprinted figure with permission from [45], copyright (2017) by the American Physical Society.
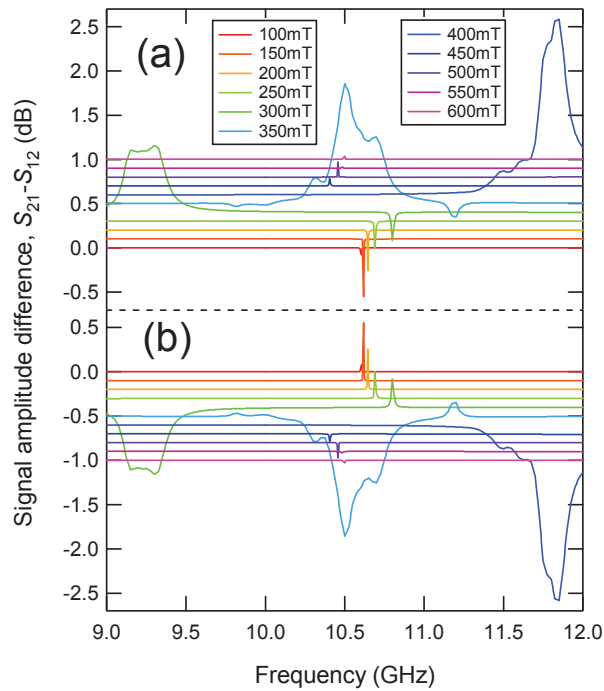
Figure 23. Differences between S_{21} and S_{12} in calculated amplitude spectra in range from 9 GHz to 12 GHz of (a) right- and (b) left-handed MCh metamolecules. The $\mu_0 H_{\text{ext}}$ is varied from + 100 to + 600 mT with steps of 50 mT. Reprinted figure with permission from [45], copyright (2017) by the American Physical Society.

1 field direction dependence is consistent with the fact that the MCh signal originates
2 from the product of ξ and κ.

5. Enhanced and giant MCh effects

In this section 5, eigenmodes of the MCh signals observed in experiments and simulations are investigated. We study eigenmodes without a coupling of FMR and chiral resonances in 5.1, eigemodes of the enhanced MCh effects in 5.2, and the giant MCh effects in 5.3. By visualizing the electromagnetic fields, an insight into the physics underlying the interplay between magnetism and chirality can be gained for the enhanced and giant MCh effects by the metamolecule. Subsection 5.4 describes possible fine tuning of the giant MCh effects.

5.1. Eigenmode without coupling of FMR and chiral resonances

Let us start with eigenmodes without coupling of FMR and chiral resonances. The eigenmodes are numerically calculated using the eigenmode solver of the COMSOL MULTIPHYSICS. Figures 24(a)-(c) illustrate electric field distributions calculated at 10.6, 13.7, and 14.5 GHz under $\mu_0 H_{\text{ext}} = +$ 100 mT, respectively. The cones and pseudo-color plots represent the electric field vectors and intensities, respectively. Since FMR by the magnetic meta-atom is far below the chiral resonance frequency at $\mu_0 H_{\text{ext}} = +$ 100 mT, there is no coupling of FMR and chiral resonance.

The electric field at chiral resonance around 10.6 GHz in Fig. 24(a) exhibits spatially symmetric distribution with respect to the center of the metamolecule. By contrast, the electric field at the chiral resonance around 13.7 GHz is antisymmetric as illustrated in Fig. 24(b). This difference in the spatial symmetry is caused by the charge distributions as schematically illustrated in the insets. Under these field distributions, the chiral resonances exhibit anti-crossing behaviors in the vicinity of FMR of the ferrite meta-atom. In addition to the spatial mode patterns, we characterize those modes by a quality (Q) factor. The Q factors of the modes at 10.6 and 13.7 GHz are evaluated to be 1578 and 213, respectively. The chiral resonance at 14.5 GHz that does not exhibit anti-crossing shows, however, completely different electric field distributions as shown in Fig. 24(c).

Figures 24(c) and 24(d) depict the electric fields at the chiral resonance at 14.5 GHz in the y-z and z-x planes, respectively. Figure 24(c) demonstrates that the electric fields are excluded from the metamolecule. The electric field exclusion is more clearly seen in the field distribution in the z-x plane as highlighted in Fig. 24(d). The inset in Fig. 24(d) highlights the electric charge distribution pattern corresponding to the field distribution. Because the electric fields induced by the surface charge (green arrows) are antiphase to the applied electric fields by microwave (purple arrows), the electric fields in the metamolecule are canceled out. This is the reason why the electric fields are excluded from the metamolecule at the chiral resonance around 14.5 GHz. The Q factor of this mode is evaluated to be 1773, which is the highest Q factor among the three chiral resonances. The mode characteristics are summarized in Table 1.

Since the exclusive chiral resonance at 14.5 GHz is quite different from the other modes, we conducted a further numerical investigation. The WR-90 waveguide was
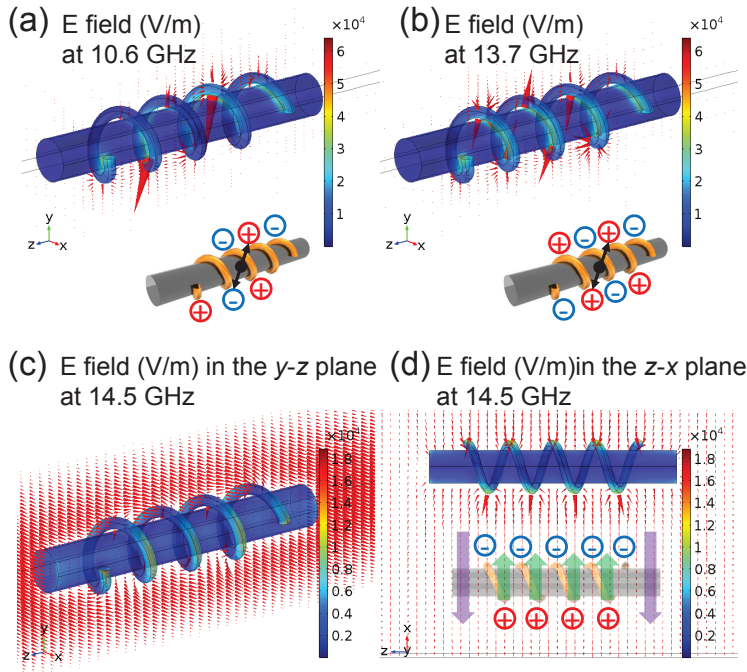
Figure 24. Electric field distributions of three chiral resonances under + 100 mT. Resonance frequencies are 10.6 (a), 13.7 (b), and 14.5 GHz [(c) and (d)], respectively. Cones and pseudo-color plots indicate electric field vectors and intensities, respectively. Vector fields in y-z plane are illustrated in (a)-(c), whereas those in z-x plane are illustrated in (d). Insets illustrate electric charge distributions. Purple arrows in (d) are applied electric fields on metamolecule, whereas green arrows are electric fields induced by charge distribution by electric charge on chiral meta-atom. Reprinted figure with permission from [45], copyright (2017) by the American Physical Society.

Table 1. Characteristics of three chiral resonances.

Frequency	10.6 GHz	13.7 GHz	14.5 GHz
Spatial mode	Anti-symmetric	Symmetric	Exclusive
Q factor	1,578	213	1,773

removed and the boundary was set to be free space. Under this situation, we were not able to find this exclusive chiral resonance while we found other chiral modes. This result indicates that the exclusive chiral resonance is characteristic to the metamolecule in the WR-90 waveguide.

5.2. Eigenmode of enhanced MCh effect

Experimental and numerical results demonstrate that the MCh effects are enhanced at chiral resonance frequencies and FMR frequency. The MCh signals due to the chiral resonance except for the exclusive chiral resonance begin to shift to higher frequencies as FMR approaches. After being passed by FMR, the MCh signals revive at lower
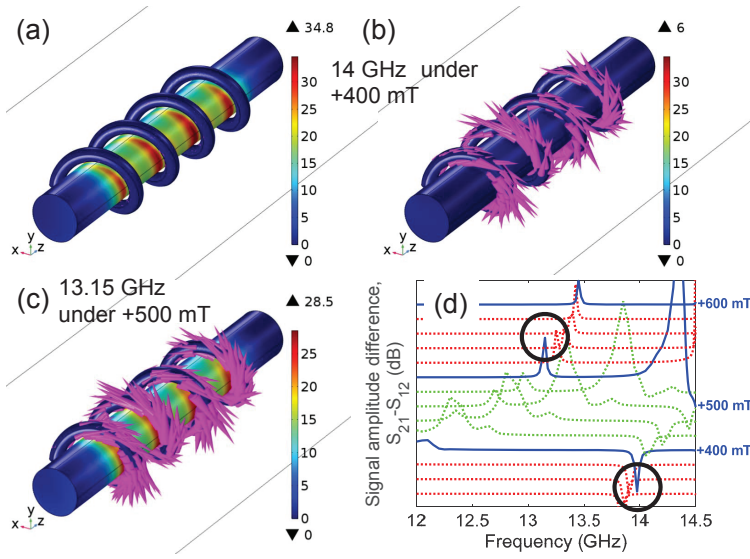
Figure 25. Intensity of magnetization (pseudo color) and vector field of surface current density (cones) in vicinity of FMR of ferrite magnetic meta-atom at (a, b) 14 GHz under + 400 mT and (c) 13.15 GHz under + 500 mT. (d): Enlarged spectra of Fig. 20(b). Length of cone is proportional to an amplitude of surface current density.

1 frequencies with an opposite polarity. The shift is explained by the effective μ in the
2 WR-90 waveguide, which is described by $\mu \pm \kappa$. Besides $\mu - \kappa$, $\mu + \kappa$ has a singularity
3 as a function of $\mu_0 H_{\text{ext}}$. As $\mu_0 H_{\text{ext}}$ is increased below the singularity, the positive $\mu + \kappa$
4 increases, bringing about a shift in the chiral resonance frequency to a higher frequency.
5 Above the singularity, $\mu + \kappa$ becomes negative and increases with $\mu_0 H_{\text{ext}}$, leading to
6 the significant red-shift of the chiral resonance frequency. With a further increase in
7 $\mu_0 H_{\text{ext}}$, the chiral resonance moves to a higher frequency and arrives at the initial chiral
8 resonance frequency.

9 The polarity reversal after being passed by FMR is further evidence of the MCh
10 effect, which is proportional to the product of ξ and κ. The κ flips its sign in the vicinity
11 of FMR of the ferrite magnetic meta-atom. Following the sign inversion, the MCh signal
12 polarity is reversed. In order to elaborate the physics underlying the sign reversal, the
13 eigenmode is calculated in the vicinity of FMR of the ferrite magnetic meta-atom as
14 shown in Fig. 25. In Fig. 25, the pseudo color indicates strength of the magnetization,
15 whereas the cones show the surface current density flowing on the chiral meta-atom.

16 Figures 25(a) and 25(b) correspond to the enhanced MCh effect before being passed
17 by FMR. The field intensity of the magnetization becomes maximum when the current
18 density responsible for the chiral resonance is minimum as in Fig. 25(a), and vice versa
19 as in Fig. 25(b). Namely, the chiral resonances are out-of-phase before being passed
20 by FMR ‡. On the other hand, Fig. 25(c), corresponding to the enhanced MCh effect

‡ See supplementary data (Figs. S1 and S2) at http://iopscience.iop.org/article/ for animation of the enhanced MCh effects. Figures S1 and S2 correspond to animations of Figs. 25(b) and 25(c), respectively.

after being passed by FMR, shows that both the magnetization and current density are on resonance, indicating that these resonances are in-phase. These calculation results demonstrate that the chiral resonance splits into two modes in the vicinity of FMR: one is the in-phase mode of the magnetic and chiral resonances, and the other is the out-of-phase one. These modes have different eigen-energies and exhibit a splitting feature in the spectra [see Fig. 25(d)]. Due to the hybridization of the resonances, the FMR and chiral resonances are simultaneously excited, leading to the enhancement of the MCh effects. Polarity inversion of these MCh signals is elucidated from the phase of the modes. There is a phase difference between the magnetic and chiral resonances before being passed by FMR, whereas there is no difference after begin passed by FMR. The phase difference gives rise to the reversal of Poynting vector flow compared with the resonance after being passed by FMR, causing the polarity inversion. In this way, the enhanced MCh effects originate from the hybridization of the magnetic and chiral resonances.

5.3. Eigenmode of giant MCh effect

Let us focus on the eigenmodes of the giant MCh effects. We calculated the field distribution of magnetization and surface current density responsible for the giant MCh effect. In Fig. 26, the pseudo color and magenta cones indicate respectively magnetization intensity and field distribution of surface current density. An incident microwave with $\vec{k}$ propagates from port 1 to port 2, i.e., S_{21}, in Fig. 26(a), whereas that from port 2 to port 1, i.e., S_{12}, in Fig. 26(b). Figures 26(a) and 26(b) show that the FMR and chiral resonances are simultaneously excited. While this is a common feature, a significant difference in the strength of the resonance is found between Figs. 26(a) and 26(b).

When excited from port 1, the FMR and chiral resonances destructively interfere, which brings about weak resonances in the metamolecule §. In particular, the chiral resonance is quite weak due to the the interference. On the other hand, when excited from port 2, those two resonances constructively interfere, leading to strong resonances in the metamolecule. The field distributions of these modes are different from those of enhanced MCh effects. This difference is attributed to the Q factor, which is a key parameter on the interaction between two modes. The Q factor of the exclusive chiral resonance that is responsible for the giant MCh effect, has the highest value among the three chiral resonances. Owing to the high Q factor, the interaction strength between chiral resonance and magnetic resonance is different from that of the enhanced MCh effect. In this way, the giant MCh effect exhibits the Fano-like resonance while the enhanced MCh effect shows the mode splitting.

The non-reciprocal Fano-like resonance in spectra is numerically confirmed. In Fig. 27, the calculated amplitude spectra for S_{21} and S_{12} under $\mu_0 H_{\text{ext}} = + 505$ mT are

§ See supplementary data (Figs. S3 and S4) at http://iopscience.iop.org/article/ for animation of the giant MCh effects. Figures S3 and S4 correspond to animations of Figs. 26(a) and 26(b), respectively.
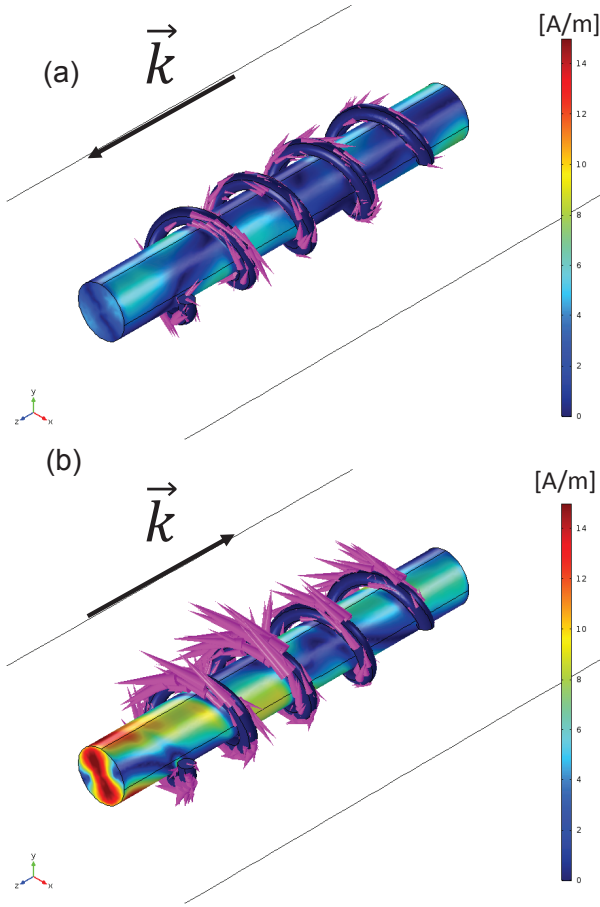
Figure 26. Magnetization intensity (pseudo color) and surface current density (cones) distributions at 14.446 GHz under $\mu_0 H_{\text{ext}} = +505$ mT. Incident waves in (a) and (b) are from ports 1 and 2, respectively.

drawn by red and blue solid curves, respectively. A green dashed curve corresponds to the calculated amplitude spectrum for S_{21} with only magnetic meta-atom as a control. The green dashed curve has a broad dip at approximately 14.6 GHz, which is caused by FMR of the ferrite meta-atom. In the vicinity of FMR, there is the exclusive chiral resonance at 14.5 GHz indicated by a vertical black dashed line. The interaction between the magnetic and chiral resonance brings about the Fano-resonance feature in the amplitude spectra, which is found in the sharp dip in the S_{12} spectrum (blue). On the other hand, we can find a quite weak chiral resonance on the S_{21} spectrum (red) due to the destructive interference.

The interference can be interpreted as an electromagnetic induction modulated by the MO effect. The magnetic meta-atom gives rise to the magnetization described as $\vec{M} = \chi_{xx}^{\text{m}} \vec{H} + i\vec{\kappa} \times \vec{H}$, where the second term represents the MO effect. In the presence of the magnetization $\vec{M}$, the MO effect modulates the magnetic flux density $\vec{B}$ as, $\vec{B} = \mu\vec{H} + i\vec{\kappa} \times \vec{H}$. As a result, the magnetic flux Φ through the chiral meta-atom is affected by the MO effect: $\Phi = \vec{B} \cdot \vec{S} = (\mu\vec{H} + i\vec{\kappa} \times \vec{H}) \cdot \vec{S}$, where $\vec{S}$ is the cross section of the chiral meta-atom for induction. Since this flux modulated by the MO effects
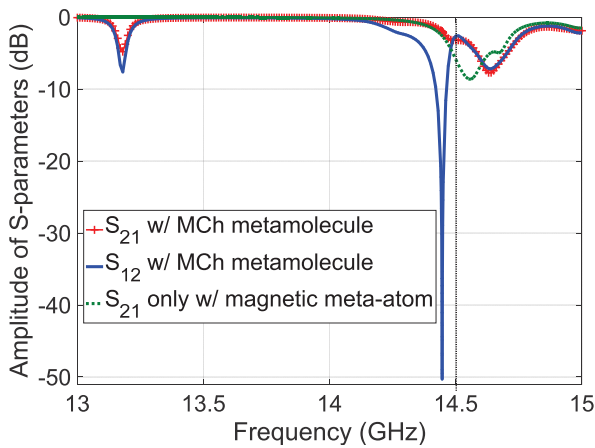
Figure 27. Calculated amplitude spectra for S_{21} (red) and S_{12} (blue) of MCh metamolecule between 13 and 15 GHz under $\mu_0 H_{\text{ext}} = +505$ mT. Amplitude spectrum of S_{21} calculated only with magnetic meta-atom is plotted also by a green dashed curve as reference. Third chiral resonance frequency is indicated by a vertical black dashed line. Reprinted figure with permission from [45], copyright (2017) by the American Physical Society.

causes the optical activity, the MCh effects with non-reciprocal directional birefringence are significantly enhanced by the Fano-like interference between chiral resonance and magnetic resonance. An opposite process also brings about the same result. The chiral meta-atom induces a magnetic flux density in the magnetic meta-atom. In the presence of the chirality-induced magnetic flux, the magnetization precession is modulated, leading to the MCh effects. Through these coupling processes, the interference between the magnetic and chiral resonances causes strong Fano interference when excited from port 2, whereas that from port 1 causes quite weak one. This non-reciprocity in the interference leads to the large amplitude difference. In other words, the metamolecule strongly absorbs the incident microwaves when excited from port 2, whereas it is almost transparent to the incident microwaves when excited from port 1. Namely, one-way transparency is realized in the MCh metamolecule.

Very similar phenomena have been reported in natural materials at low temperature and/or under very strong magnetic field: in chiral-lattice magnet Cu_2OSeO_3 for microwaves [21, 56] and multiferroic CuB_2O_4 for near-infrared light [34]. In the multiferroic materials, the one-way transparency is traced back to the interference between the $E1$ and $M1$ transitions under the condition that the two transitions have nearly the same amplitude. Similarly the interaction between FMR and chiral resonance gives rise to the one-way transparency in the MCh metamolecule. Following the large amplitude difference caused by the one-way transparency, the phase difference between S_{21} and S_{12} becomes larger due to the Kramers-Kronig relation. We conclude that the giant MCh effect observed in the present study originates from the one-way transparency caused by the non-reciprocal Fano interference in the metamolecule.
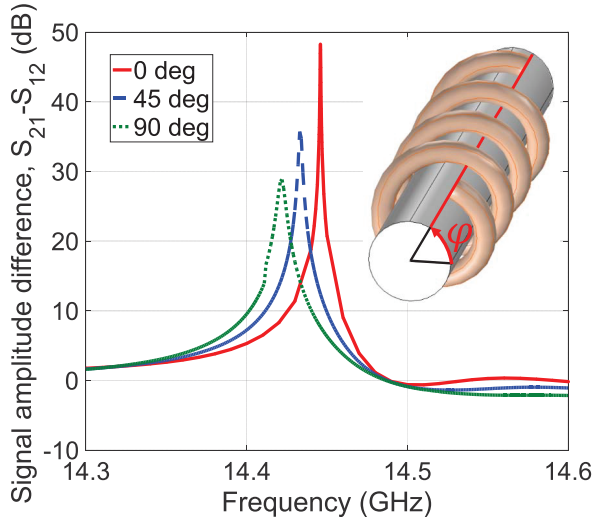
Figure 28. Differential spectra between S_{21} and S_{12} in amplitudes of MCh metamolecule under $\mu_0 H_{\mathrm{ext}}$ of $+$ 505 mT at various φ. The inset shows definition of the angle φ.

5.4. Fine tuning of giant MCh effect

The giant MCh effect originates from the non-reciprocal Fano interference. The Fano resonance consists of FMR with a low Q factor, which leads to a direct coupling of the mode to the electromagnetic wave (so-called bright mode), and the chiral resonance with a high Q factor (dark mode). Because of the high Q factor, metamolecule microwave response is quite sensitive to a variation in structure parameters. In this subsection, we examine a possible fine tuning of the giant MCh effect by changing the structure parameters, for example, chiral meta-atom rotation (5.4.1), and magnetic meta-atom position and length (5.4.2).

5.4.1. Rotation dependence of chiral meta-atom The chiral meta-atom has a rotation degree of freedom around the z-axis. As depicted in the inset of Fig. 28, the angle φ is defined as an angle between the horizontal direction and the starting point of the chiral structure. In the numerical calculations so far, φ was fixed to be $0°$. However, we consider here the variation in φ and numerically investigate how the giant MCh effect depends on φ. Figure 28 shows the differential spectra in amplitudes between S_{21} and S_{12} of the metamolecule under $\mu_0 H_{\mathrm{ext}}$ of $+$ 505 mT at φ of $0°$, $45°$, and $90°$. The giant MCh signal amplitude decreases with an increase in θ. The interaction strength between the chiral and magnetic meta-atoms varies with the rotation of the chiral meta-atom. This variation affects the Fano resonance responsible for the giant MCh effect. The decrease in signal is caused by the de-tuning to the Fano resonance.

5.4.2. Position and length dependence of magnetic meta-atom While we placed the magnetic meta-atom just at the center of the chiral meta-atom so far, we investigate
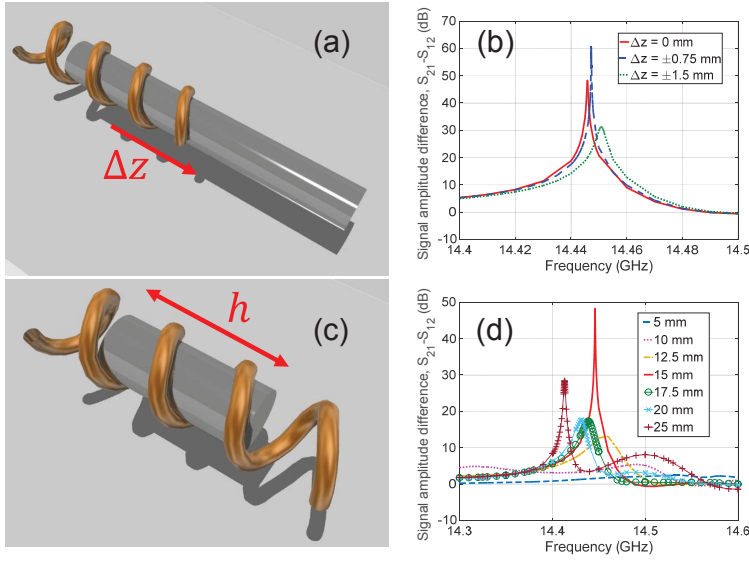
Figure 29. Definition of the ferrite rod position (a) and length (c). Position (b) and length (d) dependence of differential amplitude spectra.

₁ here the position dependence of the magnetic meta-atom on the giant MCh effect. Figure
₂ 29(a) illustrates that the magnetic meta-atom is moved to the z direction. The position
₃ shift Δz was changed from $-$ 1.5 mm to $+$ 1.5 mm with steps of 0.75 mm. The signal
₄ amplitude differences calculated under $+$ 505 mT are shown in Fig. 29(b). The giant
₅ MCh signals exhibited symmetric response to the shift along the z direction owing to
₆ the symmetry in the z direction. The MCh signal becomes maximum when the position
₇ shift is $\pm$ 0.75 mm. This maximum point is the consequence of the fine tuning of the
₈ position to the Fano resonance. The maximum amplitude difference was 60.8684 dB,
₉ which is the largest MCh signal among those of our previous reports.

₁₀ We also changed the magnetic meta-atom length as shown in Fig. 29(c) while
₁₁ keeping the position at the center. Figure 29(d) shows that the giant MCh signal is
₁₂ quite sensitive to the magnetic meta-atom length. When the magnetic meta-atom is
₁₃ short and embedded in the chiral meta-atom ($h = 5$ and 10 mm), the MCh signals are
₁₄ quite weak and have no explicit peak structure. This is caused by the fact that the chiral
₁₅ meta-atom with the exclusive resonance screens the incident microwave and decreases
₁₆ the coupling with the magnetic meta-atom. With increase of the length of the magnetic
₁₇ meta-atom ($h = 12.5$, 15, 17.5, and 20 mm), the metamolecule begins to exhibit the Fano
₁₈ resonance feature. However, only the case that $h = 15$ mm exhibits the giant MCh effect,
₁₉ indicating that the Fano resonance was fine-tuned in the previous numerical simulation.
₂₀ When the magnetic meta-atom length is 25 mm, the MCh spectrum has a sharp peak
₂₁ around 14.42 GHz, indicating the Fano resonance is fine tuned. However, the strength
₂₂ is much weaker than that of 15 mm. Through the calculations, we revealed that precise
₂₃ position control of the meta-atoms is important in realization of the giant MCh effect.
₂₄ In particular, we found that a further enhancement of the giant MCh effect can be
₂₅ achieved by the fine-tuning of the magnetic meta-atom position along the z direction.

6. Miniaturization of MCh metamolecule

Since the metamolecule operational frequency scales with size, miniaturization is required for the directional birefringence realization at higher frequencies, for example, millimeter waves and THz waves. Nevertheless, owing to their 3D structures, micrometer-sized MCh metamolecules are difficult to prepare using only standard micro-processing with photolithography and etching. In this section, miniaturization of MCh metamolecules is demonstrated. We show in 6.1 that strain-driven self-coiling is a powerful technique for preparing 3D MCh metamolecules. The single Py metamolecule is studied using cavity (6.2) and coplanar waveguide (CPW) FMR (6.3), leading to the evaluations of metamolecule's g-factor, effective magnetization, and Gilbert damping in 6.4. Finally, subsection 6.5 details magnetization configuration in the metamolecule, which is essential information for obtaining MCh effects by the miniaturized metamolecules.

6.1. Strain-driven self-coiling technique

Micrometer-sized and free-standing Py MCh metamolecules were fabricated using the strain-driven self-coiling technique [172, 173, 174, 175, 176, 177, 178, 179, 180, 181, 182]. The fabrication processes and sample cross-sections are illustrated in Figs. 30(a)-30(d). SU8 3005 photoresist (Nippon Kayaku) of 5 μm thickness was spin-coated on a Si substrate. Inverse s-shaped strips were patterned on the resist using photolithography [Fig. 30(a)]. The strip length was 1.1 mm and the strip width was 9 μm. Py was deposited on the sample using a magnetron sputtering technique with an argon gas pressure of 4.2×10^{-3} Torr [Fig. 30(b)]. The Py deposition rate was 0.1 nm/s as calibrated by X-ray reflectometer. The Py layer thickness was 60 nm. By dipping the sample into N-methyl-2-pyrrolidone (NMP), the strips coiled spontaneously, leading to the formation of free-standing Py MCh metamolecules [Fig. 30(c)]. The free-standing metamolecules were transferred to another Si substrate using tweezers and fixed by grease [Fig. 30(d)].

Figure 30(e) shows an optical microscopic image of the metamolecule fixed by grease on the Si substrate after transfer. As in Fig. 30(e), the strip coils up six times, and the metamolecule length and diameter are about 50 μm. The coiling direction is clockwise, indicating that the strip coils up toward the outside of the curvature as we previously reported [46]. We have succeeded in controlling the coiling direction using s-shape or inversed s-shape. Additionally, the Py thin films are supported by the rigid SU8 resist strips having 5 μm in thickness so that a procedure to preserve the micro structures (e.g., critical point drying) is unnecessary. Py volume in the single metamolecule is calculated at approximately 6.1×10^{-16} m^3. Magnetization curves of the metamolecules obtained by alternating gradient magnetometer with external magnetic field parallel to the chiral axis shows spontaneous magnetization with a small coercivity. Saturation magnetization is approximately 850 mT, which is slightly smaller than the saturation magnetization of metallic Py thin film (1.05 T) given in the literature [183]. These results indicate that
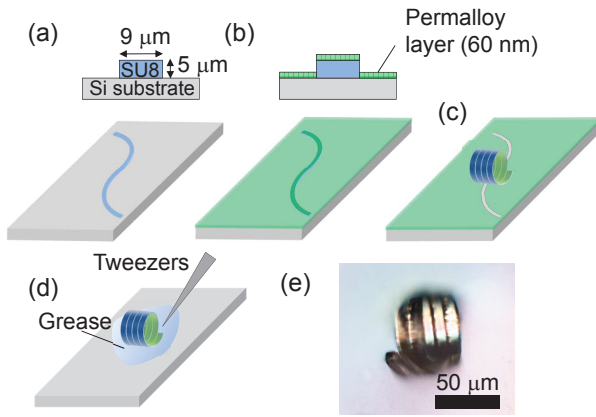
Figure 30. (a)-(d) Fabrication procedures of Py MCh metamolecule using strain-driven self-coiling technique. (e) Optical microscopic image of single metamolecule fixed by grease on silicon substrate. Reprinted figure with permission from [47], copyright (2016) by the American Physical Society.

the metamolecules retain the soft magnetic nature of metallic Py.

6.2. Cavity ferromagnetic resonance (FMR)

A single Py metamolecule transferred to the Si substrate was studied by the angle-resolved FMR with varying applied H_{ext} direction. The chiral axis was set to be perpendicular to the substrate plane. Angle-resolved FMR of the metamolecule in a TE_{011} cavity for the X-band microwave of 9.8 GHz was carried out using an electron spin resonance (ESR) spectrometer (JEOL JES-FA100N) equipped with an electromagnet for H_{ext}. The inset of Fig. 31 depicts the H_{ext} configuration in the measurement. The H_{ext} angle (θ_{H}) was varied in the x-z plane. The measurements were carried out at room temperature.

Figure 31 illustrates angle-resolved FMR spectra of the single Py metamolecule in the cavity. The angle increments were 15°. The $\theta_{\mathrm{H}} = 0°$ and $\theta_{\mathrm{H}} = 90°$ correspond to H_{ext} applied parallel and perpendicular to the chiral axis, respectively. The direction of the X-band microwave ac magnetic field in the TE_{011} cavity was parallel to the y-axis; in other words, perpendicular to both the metamolecule chiral axis and H_{ext}. Signal intensities were normalized using an ESR signal from manganese ions as the standard sample between 320 mT and 360 mT.

Figure 31 highlights two-types of resonance: one shifts slightly to a lower field and the other shifts significantly to a higher field as θ_{H} is increased. A strong resonance at 106 mT is seen when $\theta_{\mathrm{H}} = 0°$. As θ_{H} is increased, the resonance signal at 106 mT shifts very slightly to a lower field and the signal intensity becomes weaker. The resonance field shifts to its lowest, about 97 mT, at $\theta_{\mathrm{H}} = 75°$. The resonance moves back to a higher field accompanied by an increase in intensity when θ_{H} is further increased.

At $\theta_{\mathrm{H}} = 15°$, additional weak resonance signals are observed at 117 mT and 134 mT. In contrast to the resonance at 106 mT, these resonances shift significantly to higher
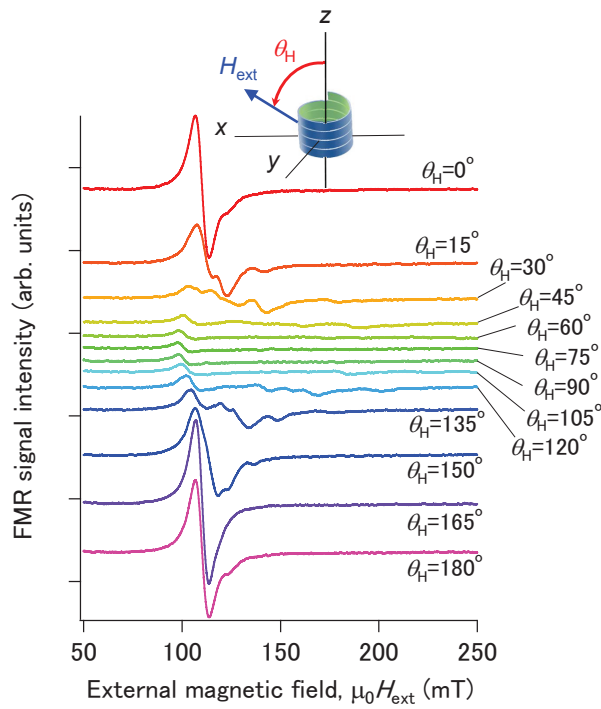
Figure 31. Angle-resolved FMR signals of single Py metamolecule in cavity. Inset illustrates definition of H_{ext} angle (θ_H). Reprinted figure with permission from [47], copyright (2016) by the American Physical Society.

1 fields as θ_H is increased. At $\theta_H = 30°$, three weak resonance signals are observed at 114,
2 136, and 170 mT. These resonances disappear from the dc magnetic field measurement
3 range (0 - 650 mT) when θ_H is between 60° and 90°. At $\theta_H = 120°$, the weak resonances
4 are observed again at 136, 152, 161, and 190 mT. The weak resonances shift to lower
5 fields as θ_H is increased and merge with the resonance of 106 mT at $\theta_H = 165°$. The
6 metamolecules show the weak FMR when the magnetic field direction is oblique to the
7 chiral axis while a Py plain film does not show the weak resonances (not shown here).
8 The weak resonances are caused by the metamolecule shape, whereas the metamolecule
9 chirality does not affect the angle-resolved FMR signals.

10 In the present preparation processes, we did not use two-step lithography followed
11 by lift-off processes [46]. Such improvements enable us to realize the Py MCh
12 metamolecule sample without any residual Py films on the substrates. Indeed, when the
13 H_{ext} angle (ϕ_H) is varied in the x-y plane, the FMR signals are identical at any ϕ_H. A
14 resonance is seen at 94 mT and this resonance does not shift while ϕ_H is increased. No
15 additional resonances emerge with an increase in ϕ_H. These results prove an absence of
16 the residual Py films on the substrates.

17 *6.3. Coplanar-waveguide FMR*

18 As illustrated in Fig. 32 (a), CPW consisting of a Au signal line with 82 μm in width and
19 1 mm in length sandwiched with two Au ground lines were fabricated using standard
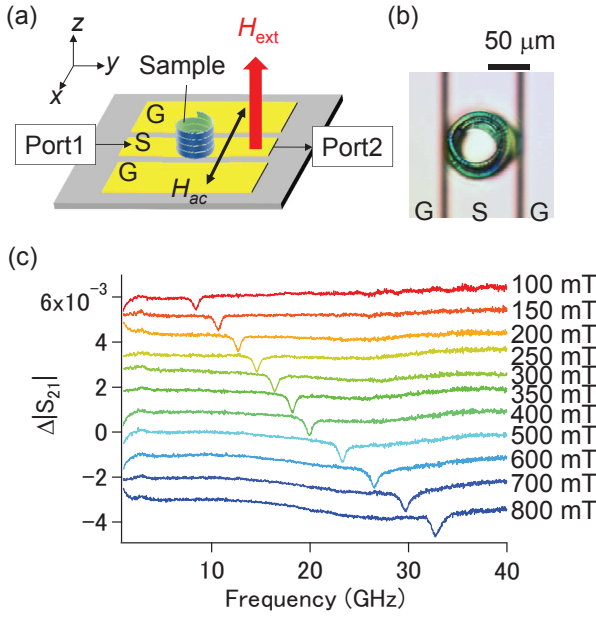
Figure 32. (a) Schematic and (b) optical microscope image of single Py MCh metamolecule placed on coplanar waveguide (S: signal line, G: ground line) in CPW-FMR measurement. Py MCh metamolecule's chiral axis is parallel to external dc magnetic field (H_{ext}). The ac magnetic field (H_{ac}) generated by microwaves is perpendicular to chiral axis and H_{ext}. (c) Microwave transmission spectra of single Py metamolecule on CPW. Reprinted figure with permission from [47], copyright (2016) by the American Physical Society.

photolithography together with Au deposition and lift-off processes. The gap between the signal and ground lines was 9 μm. A single Py metamolecule was placed at the center of the signal line as shown in Figs. 32(a) and 32(b). The $\mu_0 H_{\text{ext}}$ up to 1.35 T was applied using an electromagnet. The $\mu_0 H_{\text{ext}}$ direction was parallel to the z-axis (i.e., parallel to the chiral axis). The microwaves propagated in the y direction from port 1 to port 2 in the signal line. The ac magnetic field generated by the microwave is in the x-axis direction, which is perpendicular to the chiral axis and $\mu_0 H_{\text{ext}}$ (the z direction), and microwave propagating direction (the y direction). The microwaves transmission coefficients from port 1 to port 2 corresponding to the S parameter of S_{21} were measured using a vector network analyzer (VNA; Agilent E8363C) at room temperature. Microwave frequency was swept from 1 GHz to 40 GHz.

Since the single metamolecule FMR signal is quite small, we derive $\Delta|S_{21}|$ as

$$\Delta|S_{21}| = |S_{21}^{\text{raw}}| - |S_{21}^{\text{bg}}|, \tag{30}$$

where S_{21}^{raw} corresponds to S_{21} under a specific non-zero $\mu_0 H_{\text{ext}}$ and S_{21}^{bg} to S_{21} under zero $\mu_0 H_{\text{ext}}$. S_{21}^{bg} was measured just before every measurement of S_{21}^{raw}. Figure 32(c) illustrates transmission spectra $\Delta|S_{21}|$ at various $\mu_0 H_{\text{ext}}$. When $\mu_0 H_{\text{ext}} = 100$ mT, a dip appears at approximately 8.3 GHz. The dip shifts to a higher frequency as $\mu_0 H_{\text{ext}}$ is increased and finally reaches to 32.7 GHz when $\mu_0 H_{\text{ext}} = 800$ mT.

As a control, a 60 nm thick Py strip having 9 μm in width and 700 μm in length

1 was prepared on another CPW using a standard photolithography followed by the Py

2 deposition and the lift-off process. The longitudinal strip is placed at the signal line

3 edge in CPW-FMR measurements because the sensitivity is the highest at the edge. The

4 $\mu_0 H_{\text{ext}}$ is applied in the direction parallel to the z-axis. Although not shown here, an

5 FMR signal appears at much higher $\mu_0 H_{\text{ext}}$ above 1.1 T owing to the demagnetization

6 field in the Py strip, and shifts with an increase in $\mu_0 H_{\text{ext}}$.

7 *6.4. g-factor, effective magnetization, and Gilbert damping of metamolecule*

8 The resonance frequency f_0 and full width at the half maximum (FWHM) Δf of the

9 dip in the $\Delta|S_{21}|^2$ spectra [Fig. 32(c)] were evaluated by the fitting to the Lorentz

10 function. The least square method was employed in the fitting so that errors correspond

11 to standard deviation. The single Py metamolecule's f_0 are plotted as a function of

12 $\mu_0 H_{\text{ext}}$ in Fig. 33(a) (open circles). Since the standard deviations in f_0 are quite small,

13 error bars cannot be seen in Fig. 33(a).

14 The most likely origin of the resonance observed in Fig. 32(c) is the Kittel mode

15 FMR corresponding to uniform precession of electron spins in Py films [184]. Hence the

16 f_0 plot in Fig. 33(a) is fitted using the Kittel formula. When $\mu_0 H_{\text{ext}}$ is applied in an

17 oblique direction to the film surface with an angle of Θ_{H}, the Kittel formula is written

18 as [185]

$$19 \quad \left(\frac{\omega_0}{\gamma}\right)^2 = (\mu_0 H_0 + \mu_0 M_{\text{eff}} \cos 2\Theta_{\text{H}})(\mu_0 H_0 - \mu_0 M_{\text{eff}} \sin^2 \Theta_{\text{H}}), \tag{31}$$

20 where $\omega_0 = 2\pi f_0$ is the resonance angular frequency, $\gamma = g_{\text{eff}}(\mu_{\text{B}}/\hbar)$ is gyromagnetic

21 ratio, $\mu_0 H_0$ is the resonance magnetic field, and $\mu_0 M_{\text{eff}}$ is the effective saturation

22 magnetization including magnetic anisotropies [186], for example, the surface and

23 interface magnetic anisotropy. The g_{eff} represents the effective g-factor. The μ_{B} and $\hbar$

24 correspond to the Bohr magneton and the Planck constant divided by 2π, respectively.

25 In Eq. (31), $\Theta_{\text{H}} = 0°$ and $180°$ are assigned to $\mu_0 H_{\text{ext}}$ parallel to the film plane whereas

26 $\Theta_{\text{H}} = 90°$ is assigned to that perpendicular to the film plane. Because $\mu_0 H_{\text{ext}}$ is applied

27 perpendicular to the CPW (i.e., parallel to the chiral axis of the metamolecule on

28 the CPW), the present CPW-FMR measurement for the metamolecule corresponds to

29 $\Theta_{\text{H}} = 0°$. Therefore, after substituting $\Theta_{\text{H}} = 0°$ into Eq. (31), we use the Kittel formula

30 written as

$$31 \quad \left(\frac{\omega_0}{\gamma}\right)^2 = \mu_0^2 H_0(H_0 + M_{\text{eff}}), \tag{32}$$

32 in the fitting.

33 The red solid line in Fig. 33(a) corresponds to the fitting curve by Eq. (32). The

34 fitting procedure gives g_{eff} of 2.1590 ± 0.0082 and $\mu_0 M_{\text{eff}}$ of 681.77 ± 9.01 mT. The errors

35 represent standard deviation in the fitting. The $\mu_0 M_{\text{eff}}$ of 681.77 ± 9.01 mT evaluated

36 from the CPW-FMR is smaller than the saturation magnetization of 850 mT evaluated

37 from the magnetization curve. Because $\mu_0 M_{\text{eff}}$ obtained by the CPW-FMR is more

38 appropriate for discussing dynamical magnetic properties, 681.77 ± 9.01 mT of $\mu_0 M_{\text{eff}}$
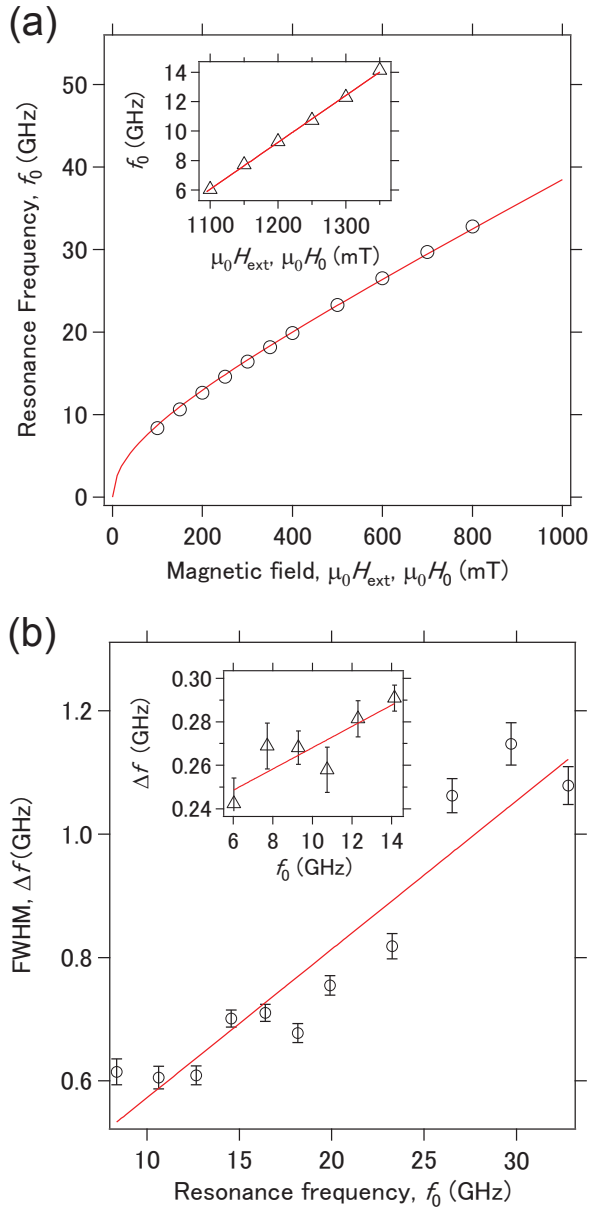
Figure 33. (a) FMR frequencies of Py metamolecule (open circles) and Py strip (open triangles in inset) measured using VNA are plotted as a function of $\mu_0 H_{ext}$. Red solid line corresponds to fitting curve by Kittel formula. (b) Full width at half maximum of FMR signals of Py metamolecule and strip (inset) is plotted as a function of resonance frequency. Red solid line corresponds to linear fitting line. Reprinted figure with permission from [47], copyright (2016) by the American Physical Society.

is utilized in the following. The fitting curve in Fig. 33(a) highlights that microwave frequency of 9.8 GHz used in the cavity-FMR gives the resonance field of 120 mT. The resonance magnetic field of 120 mT is very similar to 106 mT observed in the cavity-FMR at $\theta_H = 0$ as shown in Fig. 31. This result proves that the Kittel mode is observed in both the CPW-FMR and cavity-FMR.

The inset in Fig. 33(a) shows f_0 plotted as a function of $\mu_0 H_{ext}$ for the control

Table 2. Parameters evaluated from fitting in Figs. 33(a) and 33(b) using Eqs. (32) and (33). Reproduced table with permission from [47], copyright (2016) by the American Physical Society.

	Py metamolecule	Py strip
g_{eff}	2.1590 ± 0.0082	2.2800
$\mu_0 M_{\text{eff}}$	681.77 ± 9.01	910.45
α_{eff}	0.0120 ± 0.0014	0.0024 ± 0.0007
Δf^{ext}	0.3316 ± 0.0589	0.2192 ± 0.0155

1 Py strip fabricated on the CPW. The f_0 and Δf were obtained by fitting the dip in
2 the $\Delta|S_{21}|^2$ spectra to the Lorentz function. Since $\mu_0 H_{\text{ext}}$ is applied in the direction
3 perpendicular to the CPW, $\Theta_{\text{H}} = 90°$ is substituted into Eq. (31) and the Kittel
4 formula is obtained to be

$$\left(\frac{\omega_0}{\gamma}\right)^2 = \mu_0^2 (H_0 - M_{\text{eff}})^2. \tag{33}$$

6 The red solid line represents the fitting curve. After the fitting, g_{eff} and $\mu_0 M_{\text{eff}}$
7 were evaluated to be 2.2800 and 910.45 mT, respectively. The CPW-FMR results
8 demonstrate that g_{eff} and $\mu_0 M_{\text{eff}}$ decrease for the metamolecule.

9   Figure 33(b) illustrates a plot of Δf versus f_0 for the Py metamolecule. The inset
10 is the corresponding plot for the Py strip as a control. The error bars in Fig. 33(b)
11 represent standard deviations of experimentally evaluated Δf by the fitting using the
12 Lorentz function. The effective Gilbert damping factor α_{eff} is obtained by

$$\Delta f = 2\alpha_{\text{eff}} f_0 + \Delta f^{\text{ext}}, \tag{34}$$

14 where Δf^{ext} is the extrinsic increase in FWHM caused by defects and anisotropy
15 dispersion in the Py films [187, 188]. The red line represents the fitting curve using
16 Eq. (34). The fitting brings about α_{eff} of 0.0120 ± 0.0014 for the Py metamolecule and
17 of 0.0024 ± 0.0007 for the Py strip. The Δf^{ext} of the Py metamolecule and strip are
18 0.3316 ± 0.0589 and 0.2192 ± 0.0155, respectively. The α_{eff} and Δf^{ext} increase for the
19 metamolecule.

20   Parameters evaluated from the CPW-FMR measurements are summarized in Table
21 2. Table 2 highlights that the Py metamolecule has smaller g_{eff} and $\mu_0 M_{\text{eff}}$ and larger
22 α_{eff} and Δf^{ext} than those of the Py strip. The smaller $\mu_0 M_{\text{eff}}$ indicates surface and
23 interface anisotropies due to unsaturated spins in the Py films on the SU8 film for the
24 Py metamolecule. These unsaturated spins at the Py surface may reduce g_{eff} [189].
25 Additionally, the difference in g_{eff} might be due to the limited frequency and field range
26 in the CPW-FMR measurements.

27   Another possible origin for a decrease in g_{eff} is inhomogeneity in ac magnetic fields
28 perpendicular (H_{ac}^z) and parallel (H_{ac}^x) to the signal line generated by the microwaves.
29 However, this possibility is unlikely because H_{ac}^z, which is parallel to the dc magnetic
30 field, does not contribute to FMR. Moreover, the inhomogeneity in H_{ac}^x does not give

any changes on f_0 owing to sufficiently small H_{ac}^x (less than 0.05 mT) in the linear approximation of the Landau-Lifshitz-Gilbert equation. While the inhomogeneous ac field does not influence g_{eff}, it may cause an increase in the FWHM Δf in the FMR spectra, for example, by two-magnon scattering due to magnetization inhomogeneities [187, 188]. Furthermore, anisotropy dispersions, that is to say, magnetostriction anisotropy [190, 191] and magnetic surface/interface anisotropy [189], induced by the coiling as well as the strain, mechanical cracks, and defects in the films give rise to magnetization inhomogeneities, leading to an increase in Δf^{ext}.

6.5. Magnetization configuration in metamolecule

If the magnetic moment is oriented in-plane and orthogonal to the strip axis, the coiling process brings about a hollow-bar-magnetized structure [175]. Otherwise, if the magnetic moment is oriented in-plane but parallel to the strip axis, a corkscrew-magnetized helix coil structure is expected. The magnetization configuration in the metamolecule is essential information for obtaining MCh effects by the miniaturized metamolecules. Therefore, in the following, angle-resolved cavity-FMR with varying θ_H reveals the magnetization configuration in the metamolecule.

The cavity-FMR signals experimentally obtained in Fig. 31 are re-drawn in 2D in Fig. 34. White and blue colors correspond to high and low intensities in the derivative FMR signals, respectively. If $\theta_H = 0°$ and $180°$, the magnetic field is applied uniformly to all portions in the Py MCh metamolecule as illustrated in the lower inset of Fig. 34. The magnetization curves indicate that the Py metamolecule magnetization is easily saturated in this configuration. In this way, the Py metamolecule becomes a magnetic single domain structure, causing a single resonance of the Kittel mode at around 106 mT excited at $\theta_H = 0°$ and $180°$.

If magnetic field direction is oblique to the chiral axis ($0° < \theta_H < 180°$), the 2D plotted experimental results show two types resonances: one is shifted slightly to a lower field but excited around 100 mT at any angles, and the other is shifted significantly to a higher field as the angle θ_H is increased. Because the Py metamolecule is the 3D structure, how the magnetic field is applied to the Py film is different in each portion of the metamolecule. When θ_H is $15°$, the metamolecule's two aspects, which are parallel to the x-z plane, are parallel to the magnetic field (see inset in Fig. 34). In these two aspects, the magnetization direction follows the magnetic field direction and the magnetization is easily saturated. The Kittel mode resonance is thus observed around 100 mT at any angles. Contrastingly, magnetization in another portions, which are parallel to the y-z plane, is not parallel to the magnetic field (see inset in Fig. 34). Kittel mode FMR in these portions is an origin of the resonance significantly shifted to a higher field with an increase in θ_H.

The Kittel mode resonance fields in a thin film calculated using Eq. (31) are plotted as a function of Θ_H in Fig. 34 (open circles). In the calculation, we used g_{eff} of 2.16 and $\mu_0 M_{eff}$ of 681 mT evaluated from the Py metamolecule CPW-FMR results. At
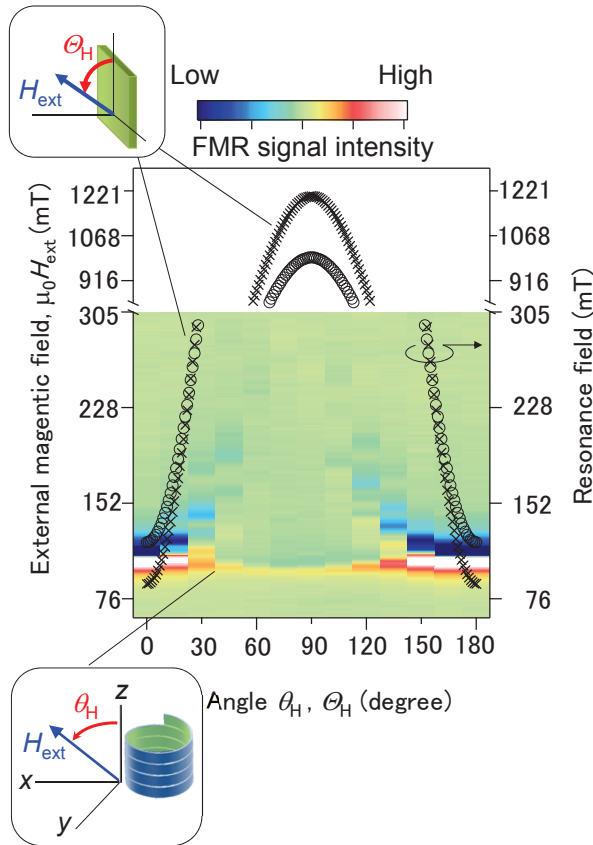
Figure 34. The two-dimensional plot shows the FMR signal intensity of a single Py metamolecule obtained in Fig. 31 as a function of angle (θ_H and Θ_H) and external dc magnetic field ($\mu_0 H_{ext}$). Angle θ_H (Θ_H) is defined in lower (upper) inset. Open circles and crosses correspond to resonance fields calculated by Kittel formula with plane Py thin film model. Reprinted figure with permission from [47], copyright (2016) by the American Physical Society.

1   $\Theta_H = 0°$ the calculated resonance field is 121 mT. As Θ_H increases, the resonance shifts
2   to a higher field owing to an increase in the demagnetization field. After reaching the
3   maximum field of approximately 994 mT at $\Theta_H = 90°$, the resonance shifts to a lower
4   field. Crosses correspond to the calculated resonance fields of the Kittel mode in a thin
5   film, but g_{eff} and $\mu_0 M_{eff}$ are the values experimentally evaluated from the Py strip CPW-
6   FMR. At $\Theta_H = 0°$ the calculated resonance field is 88 mT, which is smaller than the
7   experimental value (106 mT) and previously calculated value (121 mT). At $\Theta_H = 90°$
8   the calculated resonance field is 1203 mT, which is higher than the calculated field using
9   metamolecules' g_{eff} and $\mu_0 M_{eff}$. The resonance fields shifting to a higher field with an
10 increase in θ_H in the experiment have been reproduced qualitatively by the calculation
11 of the Kittel-mode FMR for a plane film with a magnetic moment oriented in-plane.
12 Therefore the magnetization configuration in the metamolecule at $\theta_H = 0°$ and 180° is
13 most likely to be the hollow-bar type [175]. This is very promising for obtaining optical
14 MCh effects at millimeter wave and THz frequencies.

Whereas the resonance field shift is reproduced qualitatively by the calculation, the shift amount in experiments is much smaller than those calculated using Eq. (31). The difference between calculation and experiment is likely to be due to the calculation model. In the calculation, we assume a Py thin film with g_{eff} and $\mu_0 M_{\mathrm{eff}}$ evaluated from the CPW-FMR measurements. However, the Py metamolecule consists of the Py facets, which are parallel to the x-z plane or y-z plane, and the facets are connected to each other. The connecting curved regions between the facets are likely to be an origin of the contradiction.

The inhomogeneous magnetization in the connecting curved regions is indicated by the sifting Kittel mode resonance signal in the angle-resolved cavity-FMR. Figure 34 demonstrates that the shifting resonance by a oblique magnetic field direction is accompanied by additional weak resonances at higher fields. In the aspects parallel to the y-z plane connected to curved regions, the magnetization is not saturated. It was reported that unsaturated regions in ring [192] and tubular [193] structures of magnetic thin film exhibit the inhomogeneous magnetization configuration named a onion-like state. The onion-like state shows multiple resonance signals due to the localized resonance modes. Therefore multiple resonance signals accompanied with the Kittel mode FMR observed in the metamolecule are traced back to the localized resonance modes due to the inhomogeneous magnetization configuration, which is also indicated in the CPW-FMR results.

As θ_{H} approaches $90°$, the resonance almost independent of θ_{H} shifts very slightly to a lower field. The tiny shift of the resonance can be explained by the shape anisotropy of the Py strip in the metamolecules. The Py strip is magnetized in the direction of the strip width of 9 μm when $\theta_{\mathrm{H}} = 0°$. On the other hand, when $\theta_{\mathrm{H}} = 90°$, the Py film is easily magnetized in the direction of the strip length that is much larger than the width. This leads to a very small shift of the Kittel mode resonance at 106 mT to a lower field of 97 mT. Such a small shift can be revealed in the present study since the residual Py films are absent on the substrate and the resonance signal is attributed only to the single Py metamolecule.

7. Conclusions and perspective

This Topical Review has presented an overview on electromagnetism in structured metamaterials with magnetism and chirality. Specifically, the review has focused on the optical MCh effect, i.e., directional birefringence independent of polarizations. The optical MCh effect is a combination of the MO effect and OA, and usually very tiny, but can be enhanced by the resonance in the metamaterials by several orders of magnitude greater than that of natural materials. A metamolecule was implemented using a Cu chiral structure (chiral meta-atom) for OA and YIG ferrite rod/cylinder (magnetic meta-atom) for the MO effect, and studied at the X-band microwave frequency at room temperature. Enhanced MCh effects were observed at a chiral resonance frequency around 10 GHz to be $\Delta n' \simeq 5.4 \times 10^{-3}$ and $\Delta n'' \simeq 1.5 \times 10^{-2}$ under + 200 mT and at

an FMR frequency to be $\Delta n' \simeq -8.9 \times 10^{-2}$ and $\Delta n'' \simeq -2.6 \times 10^{-1}$ under $+$ 400 mT.

Numerical calculations have successfully reproduced these experimental observations and revealed that the enhanced MCh effects are traced back to the hybridization of FMR and chiral resonances. Furthermore, a giant MCh effect with $\Delta n' \simeq -6.6 \times 10^{-1}$ and $\Delta n'' \simeq 1.26$ was predicted by numerical simulation. We indicated a fine-tuning of the giant MCh effect by the rotation angle of the chiral meta-atom, and position and length of the magnetic meta-atom. Notably, our concept of interplay between magnetism and chirality in metamaterials is applicable to other regions of the spectrum including the visible region.

For a higher frequency operation than microwave, MCh metamolecule miniaturization was conducted using a strain-driven self-coiling technique. A micrometer-sized free-standing Py chiral metamolecule was studied by cavity- and CPW-FMR, bringing about an effective g factor of 2.1590 and Gilbert damping of 0.0120. Finally, we conclude that the magnetization configuration in the Py chiral metamolecule is most likely to be the hollow-bar type. This is very promising for obtaining optical MCh effects using the metamolecule at millimeter wave and THz frequencies and a direct observation of the MCh effect at a high frequency is now underway in our group. However, many challenges remain within the optical region. To reach the optical region, the MCh metamolecule must be miniaturized to the nanometer-scale, and losses need to be reduced significantly. The former issue can be addressed by using supramolecules or biomolecules; for example, viruses [194], proteins [195], and α-helical coiled peptide [196].

In this work, we have demonstrated that a metamolecule boosted MCh effects by several orders of magnitude compared to natural molecules. The enhanced and giant MCh effects thus open a door toward the realization of synthetic gauge fields [22, 23, 24, 25, 26, 27, 28, 29]; for example, an effective magnetic field for electromagnetic waves. However, the values of non-reciprocal refractive index differences owing to the MCh effects by the single metamolecule were not yet large. While numerical simulation predicted the giant MCh effect, it was relevant to a characteristic electromagnetic mode in the waveguide. Hence, implementation of the giant MCh effect without waveguide is of great importance. Additionally, larger responses would be obtained by assembling metamolecules into metamaterials. The "Lorentz force" by synthetic gauge fields for light is expected to be observed in non-uniform metamaterials consisting of the MCh metamolecules.

MCh metamolecules embodied in the present study offer an ideal starting point for the proof-of-concept study relevant to MCh effects. For example, an inverse effect of the MCh effect is still under debate. When electromagnetic waves of arbitrary polarization travel in a medium of randomly oriented chiral molecule, it is predicted to induce a constant magnetization parallel or antiparallel to the propagation direction. This phenomenon is the inverse effect of the MCh effect, and thus referred to as the inverse MCh effect by Wagnière [197]. The inverse MCh effect is one of the second-order nonlinear optical effects, which include also a similar effect in achiral media, named inverse Faraday effect [198]. In the inverse Faraday effect the circularly-polarized

light induces a static magnetic moment parallel or antiparallel to the propagation direction; induced magnetization direction depends on the circularly polarization direction. Contrastingly to the inverse Faraday effect dependent on the polarization, the inverse MCh effect is independent of the light polarization, but it has opposite sign for enantiomers. While the inverse Faraday effect has been experimentally verified [199], the inverse MCh effect remains to be observed [200] probably owing to the very weak induced magnetization. Therefore, direct observation of the inverse MCh effects using metamaterials is of great interest.

Whereas an optical MCh metamaterial is investigated in this Topical Review, MCh metamaterials for another wave phenomena, for example, magnonic, phononic, and acoustic waves, are also of great interest. When we succeed in preparing nanometer-scaled MCh metamolecules, it may grant access to chiral domains predicted in magnetic nanotube structures [201] and Berry phase of magnons in textured ferromagnets [202]. Furthermore, another symmetry, for example, translational symmetry, can be broken in quasi-periodic metamaterials [203, 204, 205]. From this point of view, metamaterials with broken time-reversal and translational symmetries simultaneously, very similar to quasi-periodic magnonic crystals [206, 207, 208, 209, 210, 211], remain attractive to researchers in the field of magnetic metamaterials.

Simultaneous breaking of time-reversal and space-inversion symmetries has generated considerable interest not only in wave phenomena but also in diffusion phenomena, for example, thermal transport and electrical transport. Because the MCh effect is the direct consequence of the simultaneous breaking, the MCh effects are fundamental and universal. In this way, the symmetry arguments used for electromagnetism may also be applied to the electrical charge transport. Electric counterpart of the optical MCh effect is referred to as the electrical MCh effect, which was first studied theoretically and experimentally by Rikken and co-workers [212]. On the basis of symmetry arguments [213, 214, 215], the electrical MCh effect by a chiral conductor subject to a dc magnetic field manifests itself in nonlinear resistivity.

The two-terminal electrical MCh effect of Bi helices, prepared by injecting molten Bi into helical molds followed by annealing, was experimentally observed using standard phase-sensitive detection technique [212]. Furthermore, straight Bi wires containing screw dislocations were prepared by a torsional deformation. Electrical MCh effects at low temperature in single-walled carbon nanotubes [216] and in a bulk chiral organic conductor based on an enantiopure tetrathiafulvalene derivative [217] were also reported. The microscopic mechanisms for the electrical MCh effects is still unclear although several mechanisms were proposed: namely, the magnetic self-field effect, chiral scattering [212], and enantioselective current- and field-dependent differences in Fermi velocity and density of states at the Fermi level [218]. Very recently, it has been reported that thermal and quantum spin fluctuations in the chiral magnet MnSi give rise to asymmetric electron scattering, leading to a large electrical MCh effect at low temperature [219]. Metamaterials may yield an enhanced electrical MCh effect, which can be observed at room temperature.

OA in optical systems is analogous to spin-orbit interaction in electronics, whereas the MO effect is to Zeeman splitting for electrons [29]. Even metamaterials solely with OA or the MO effect can be expected to contain rich physics. For example, unidirectional backscattering-immune propagation of surface waves, referred to as electromagnetic edge modes, was observed at the boundary between two different photonic crystals: one comprising a photonic crystal with broken time-reversal symmetry using a ferromagnetic medium, and the other with time-reversal symmetry [220]. Even in a time-reversal invariant system, photonic crystals with broken space-inversion symmetry with chirality show a similar phenomenon [26]. However, little is known about the edge modes at the operation frequencies far below the photonic bandgap [221]. This new avenue of analogy between lights and electrons opens a door toward a new science; namely, meta material-science.

8. Acknowledgment

References

[1] F. Englert and R. Brout. Broken symmetry and the mass of gauge vector mesons. *Phys. Rev. Lett.*, 13:321–323, Aug 1964.

[2] P. W. Higgs. Broken symmetries and the masses of gauge bosons. *Phys. Rev. Lett.*, 13:508–509, Oct 1964.

[3] H. E. Stanley. *Introduction to Phase Transitions and Critical Phenomena*. Oxford Univ. Press, New York, 1988.

[4] E. Hecht. *Optics*. Pearson Education Limited, Harlow, 2013.

[5] N. Berova, K. Nakanishi, and R. W. Woody, editors. *Circular dichroism : principles and applications*. Wiley-VCH, New York, 2nd edition, 2000.

[6] J. A. Kong. *Electromagnetic wave theory*. EMW Publishing, Cambridge, 2005.

[7] M Wegener and S. Linden. Giving light yet another new twist. *Physics*, 2:3, 2009.

[8] N.B. Baranova, Yu.V. Bogdanov, and B.Ya. Zel'Dovich. Electrical analog of the faraday effect and other new optical effects in liquids. *Optics Communications*, 22(2):243 – 247, 1977.

[9] V. A. Markelov, M. A. Novikov, and A. A. Turkin. Experimental observation of a new nonreciprocal magneto-optical effect. *JETP Lett.*, 25:378, 1977.

[10] G. Wagnière and A. Meier. The influence of a static magnetic field on the absorption coefficient of a chiral molecule. *Chemical Physics Letters*, 93(1):78 – 81, 1982.

[11] L. D. Barron and J. Vrbancich. Magneto-chiral birefringence and dichroism. *Molecular Physics*, 51(3):715–730, 1984.

[12] G. L. J. A. Rikken and E. Raupach. Observation of magneto-chiral dichroism. *Nature (London)*, 390:493, 1997.

[13] P. Kleindienst and G. H. Wagnière. Interferometric detection of magnetochiral birefringence. *Chemical Physics Letters*, 288(1):89 – 97, 1998.

[14] G. L. J. A. Rikken and E. Raupach. Enantioselective magnetochiral photochemistry. *Nature (London)*, 405:932, 2000.

[15] M. Vallet, R. Ghosh, A. Le Floch, T. Ruchon, F. Bretenaker, and J.-Y. Thépot. Observation of magnetochiral birefringence. *Phys. Rev. Lett.*, 87:183003, Oct 2001.

[16] V. A. Sautenkov, Y. V. Rostovtsev, H. Chen, P. Hsu, G. S. Agarwal, and M. O. Scully. Electromagnetically induced magnetochiral anisotropy in a resonant medium. *Phys. Rev. Lett.*, 94:233601, Jun 2005.

[17] M. Saito, K. Ishikawa, K. Taniguchi, and T. Arima. Magnetic control of crystal chirality and the existence of a large magneto-optical dichroism effect in cub_2o_4. *Phys. Rev. Lett.*, 101:117402, Sep 2008.

[18] C. Train, R. Gheorghe, V. Krstič, L.-M. Chamoreau, N. S. Ovanesyan, G. L. J. A. Rikken, M. Gruselle, and M. Verdaguer. Strong magneto-chiral dichroism in enantiopure chiral ferromagnets. *Nature Materials*, 7:729, 2008.

[19] S. Bordàcs, I. Kézsmárki, D. Szaller, L. Demkó, N. Kida, H. Murakawa, Y. Onose, R. Shimano, T. Rõõm, U. Nagel, S. Miyahara, N. Furukawa, and Y. Tokura. Chirality of matter shows up via spin excitations. *Nature Physics*, 8:734, 2012.

[20] S. Kibayashi, Y. Takahashi, S. Seki, and Y. Tokura. Magnetochiral dichroism resonant with electromagnons in a helimagnet. *Nature Communications*, 5:4583, 2014.

[21] Y. Okamura, F. Kagawa, S. Seki, M. Kubota, M. Kawasaki, and Y. Tokura. Microwave magnetochiral dichroism in the chiral-lattice magnet cu_2oseo_3. *Phys. Rev. Lett.*, 114:197202, May 2015.

[22] K. Sawada and N. Nagaosa. Optical magnetoelectric effect in multiferroic materials: Evidence for a lorentz force acting on a ray of light. *Phys. Rev. Lett.*, 95:237402, Dec 2005.

[23] K. Fang, Z. Yu, and S. Fan. Realizing effective magnetic field for photons by controlling the phase of dynamic modulation. *Nature Phtonics*, 6:782, 2012.

[24] M. Hafezi, E. A. Demler, M. D. Lukin, and J. M. Taylor. Robust optical delay lines with topological protection. *Nature Physics*, 7:907, 2011.

[25] M. Hafezi, S. Mittal, J. Fan, A. Migdall, and J. M. Taylor. Imaging topological edge states in silicon photonics. *Nature Photonics*, 7:1001, 2013.

[26] A. B. Khanikaev, S. Hossein Mousavi, W.-K. Tse, M. Kargarian, A. H. MacDonald, and G. Shvets. Photonic topological insulators. *Nature Materials*, 12:233, 2013.

[27] L. Lu, L. Fu, J. D. Joannopoulos, and M. Soljačić. Weyl points and line nodes in gyroid photonic crystals. *Nature Photonics*, 7:294, 2013.

[28] H. Kurosawa and K. Sawada. Artificial gauge field for a light ray. *Phys. Rev. A*, 95:063846, Jun 2017.

[29] S. Tomita, K. Sawada, S. Nagai, A. Sanada, N. Hisamoto, and T. Ueda. Microwave analog of stern-gerlach effects using nonuniform chiral metamaterials. *Phys. Rev. B*, 96:165425, Oct 2017.

[30] M. Saito, K. Taniguchi, and T. Arima. Gigantic optical magnetoelectric effect in $cub2o4$. *Journal of the Physical Society of Japan*, 77(1):013705, 2008.

[31] I. Kézsmárki, N. Kida, H. Murakawa, S. Bordács, Y. Onose, and Y. Tokura. Enhanced directional dichroism of terahertz light in resonance with magnetic excitations of the multiferroic $ba_2coge_2o_7$ oxide compound. *Phys. Rev. Lett.*, 106:057403, Feb 2011.

[32] M. Mochizuki and S. Seki. Magnetoelectric resonances and predicted microwave diode effect of the skyrmion crystal in a multiferroic chiral-lattice magnet. *Phys. Rev. B*, 87:134403, Apr 2013.

[33] I. Kézsmárki, D. Szaller, S. Bordàcs, V. Kocsis, Y. Tokunaga, Y. Taguchi, H. Murakawa, Y. Tokura, H. Engelkamp, T. Rõõm, and U. Nagel. One-way transparency of four-coloured spin-wave excitations in multiferroic materials. *Nature Communications*, 5:3203, Feb 2014.

[34] S. Toyoda, N. Abe, S. Kimura, Y. H. Matsuda, T. Nomura, A. Ikeda, S. Takeyama, and T. Arima. One-way transparency of light in multiferroic cub$_2$o$_4$. *Phys. Rev. Lett.*, 115:267207, Dec 2015.

[35] N. Kida, T. Yamada, M. Konoto, Y. Okimoto, T. Arima, K. Koike, H. Akoh, and Y. Tokura. Optical magnetoelectric effect in a submicron patterned magnet. *Phys. Rev. Lett.*, 94:077205, Feb 2005.

[36] N. Kida, Y. Kaneko, J. P. He, M. Matsubara, H. Sato, T. Arima, H. Akoh, and Y. Tokura. Enhanced optical magnetoelectric effect in a patterned polar ferrimagnet. *Phys. Rev. Lett.*, 96:167202, Apr 2006.

[37] N. Kida, H. Yamada, H. Sato, T. Arima, M. Kawasaki, H. Akoh, and Y. Tokura. Optical magnetoelectric effect of patterned oxide superlattices with ferromagnetic interfaces. *Phys. Rev. Lett.*, 99:197404, Nov 2007.

[38] K. Sawada and N. Nagaosa. Gigantic enhancement of magnetochiral effect in photonic crystals. *Applied Physics Letters*, 87(4):042503, 2005.

[39] J. B. Pendry, A. J. Holden, W. J. Stewart, and I. Youngs. Extremely low frequency plasmons in metallic mesostructures. *Phys. Rev. Lett.*, 76:4773–4776, Jun 1996.

[40] J. B. Pendry, A. J. Holden, D. J. Robbins, and W. J. Stewart. Magnetism from conductors and enhanced nonlinear phenomena. *IEEE Transactions on Microwave Theory and Techniques*, 47(11):2075–2084, Nov 1999.

[41] D. R. Smith, W. J. Padilla, D. C. Vier, S. C. Nemat-Nasser, and S. Schultz. Composite medium with simultaneously negative permeability and permittivity. *Phys. Rev. Lett.*, 84:4184–4187, May 2000.

[42] R. A. Shelby, D. R. Smith, and S. Schultz. Experimental verification of a negative index of refraction. *Science*, 292(5514):77–79, 2001.

[43] D. R. Smith, J. B. Pendry, and M. C. K. Wiltshire. Metamaterials and negative refractive index. *Science*, 305(5685):788–792, 2004.

[44] S. Tomita, K. Sawada, A. Porokhnyuk, and T. Ueda. Direct observation of magnetochiral effects through a single metamolecule in microwave regions. *Phys. Rev. Lett.*, 113:235501, Dec 2014.

[45] S. Tomita, H. Kurosawa, K. Sawada, and T. Ueda. Enhanced magnetochiral effects at microwave frequencies by a single metamolecule. *Phys. Rev. B*, 95:085402, Feb 2017.

[46] T. Kodama, S. Tomita, N. Hosoito, and H. Yanagi. Fabrication and ferromagnetic resonance of cobalt chiral meta-molecule arrays. *Applied Physics A*, 122(1):41, 2016.

[47] T. Kodama, S. Tomita, T. Kato, D. Oshima, S. Iwata, S. Okamoto, N. Kikuchi, O. Kitakami, N. Hosoito, and H. Yanagi. Ferromagnetic resonance of a single magnetochiral metamolecule of permalloy. *Phys. Rev. Applied*, 6:024016, Aug 2016.

[48] L. D. Barron. Chirality, magnetism and light. *Nature (London)*, 405:895–896, 2000.

[49] S. Mühlbauer, B. Binz, F. Jonietz, C. Pfleiderer, A. Rosch, A. Neubauer, R. Georgii, and P. Böni. Skyrmion lattice in a chiral magnet. *Science*, 323(5916):915–919, 2009.

[50] S. Tomita, Y. Kosaka, H. Yanagi, and K. Sawada. Chiral meta-interface: Polarity reversal of ellipticity through double layers consisting of transparent chiral and absorptive achiral media. *Phys. Rev. B*, 87:041404, Jan 2013.

[51] S. Tretyakov, I. Nefedov, A. Sihvola, S. Maslovski, and C. Simovski. Waves and energy in chiral nihility. *Journal of Electromagnetic Waves and Applications*, 17(5):695–706, 2003.

[52] S. Tomita, T. Kato, S. Tsunashima, S. Iwata, M. Fujii, and S. Hayashi. Magneto-optical kerr effects of yttrium-iron garnet thin films incorporating gold nanoparticles. *Phys. Rev. Lett.*, 96:167402, Apr 2006.

[53] P. Riego, S. Tomita, K. Murakami, T. Kodama, N. Hosoito, H. Yanagi, and A. Berger. Enhanced magneto-optical kerr effects in py/ag/bi trilayers. *Journal of Physics D: Applied Physics*, 50(19):19LT01, 2017.

[54] G. L. J. A. Rikken and E. Raupach. Pure and cascaded magnetochiral anisotropy in optical absorption. *Phys. Rev. E*, 58:5081–5084, Oct 1998.

[55] Y. Kitagawa, T. Miyatake, and K. Ishii. Magneto-chiral dichroism of artificial light-harvesting

antenna. *Chem. Commun.*, 48:5091–5093, 2012.

[56] M. Mochizuki. Microwave magnetochiral effect in cu$_2$oseo$_3$. *Phys. Rev. Lett.*, 114:197203, May 2015.

[57] C. Koerdt, G. Düchs, and G. L. J. A. Rikken. Magnetochiral anisotropy in bragg scattering. *Phys. Rev. Lett.*, 91:073902, Aug 2003.

[58] S. Eslami, J. G. Gibbs, Y. Rechkemmer, J. van Slageren, M. Alarc´n-Correa, T.-C. Lee, A. G. Mark, G. L. J. A. Rikken, and P. Fischer. Chiral nanomagnets. *ACS Photonics*, 1(11):1231–1236, 2014.

[59] Q. Cheng and T. J. Cui. Negative refractions in uniaxially anisotropic chiral media. *Phys. Rev. B*, 73:113104, Mar 2006.

[60] D. L. Portigal and E. Burstein. Magneto-spatial dispersion effects on the propagation of electromagnetic radiation in crystals. *Journal of Physics and Chemistry of Solids*, 32(3):603 – 608, 1971.

[61] M. Born, W. Heisenberg, and P. Jordan. Zur quantenmechanik ii. *Z. Phys.*, 35:557, 1926.

[62] P. A. M. Dirac. The quantum theory of the emission and absorption of radiation. *Proc. Roy. Soc. Lond.*, A114:243, 1927.

[63] H. B. G. Casimir. On the attraction between two perfectly conducting plates. *Proc. K. Ned. Akad. Wet.*, 51:793, 1948.

[64] H. B. G. Casimir and D. Polder. The influence of retardation on the london-van der waals forces. *Phys. Rev.*, 73:360–372, Feb 1948.

[65] P. W. Milonni. *The quantum vacuum: an introduction to quantum electrodynamics*. Academic Press, San Diego, 1993.

[66] J. Babington and B. A. van Tiggelen. Casimir momentum of magneto-chiral matter. *EPL (Europhysics Letters)*, 93(4):41002, 2011.

[67] M. Donaire, B. A. van Tiggelen, and G. L. J. A. Rikken. Casimir momentum of a chiral molecule in a magnetic field. *Phys. Rev. Lett.*, 111:143602, Oct 2013.

[68] B. A. van Tiggelen, G. L. J. A. Rikken, and V. Krstić. Momentum transfer from quantum vacuum to magnetoelectric matter. *Phys. Rev. Lett.*, 96:130402, Apr 2006.

[69] J. Li and C. T. Chan. Double-negative acoustic metamaterial. *Phys. Rev. E*, 70:055602, Nov 2004.

[70] S. H. Lee, C. M. Park, Y. M. Seo, Z. G. Wang, and C. K. Kim. Composite acoustic medium with simultaneously negative density and modulus. *Phys. Rev. Lett.*, 104:054301, Feb 2010.

[71] S. Brûlé, E. H. Javelaud, S. Enoch, and S. Guenneau. Experiments on seismic metamaterials: Molding surface waves. *Phys. Rev. Lett.*, 112:133901, Mar 2014.

[72] S. Narayana and Y. Sato. Heat flux manipulation with engineered thermal materials. *Phys. Rev. Lett.*, 108:214303, May 2012.

[73] M. Kadic, T. Bückmann, R. Schittny, and M. Wegener. Metamaterials beyond electromagnetism. *Reports on Progress in Physics*, 76(12):126501, 2013.

[74] H. Lamb. On group - velocity. *Proceedings of the London Mathematical Society*, s2-1(1):473–479, 1904.

[75] H. C. Pocklington. Growth of a wave-group when the group-velocity is negative. *Nature (London)*, 71:607–608, 1905.

[76] L. Brillouin. *Wave propagation and group velocity*. Academic Press, New York, 1960.

[77] V. G. Veselago. The electrodynamics of substances with simultaneously negative values of ϵ and μ. *Soviet Physics Uspekhi*, 10(4):509, 1968.

[78] Pendry. J. B. Negative refraction. *Contemporary Physics*, 45(3):191–202, 2004.

[79] S. Linden, C. Enkrich, M. Wegener, J. Zhou, T. Koschny, and C. M. Soukoulis. Magnetic response of metamaterials at 100 terahertz. *Science*, 306(5700):1351–1353, 2004.

[80] C. G. Parazzoli, R. B. Greegor, K. Li, B. E. C. Koltenbah, and M. Tanielian. Experimental verification and simulation of negative index of refraction using snell's law. *Phys. Rev. Lett.*, 90:107401, Mar 2003.

[81] A. A. Houck, J. B. Brock, and I. L. Chuang. Experimental observations of a left-handed material that obeys snell's law. *Phys. Rev. Lett.*, 90:137401, Apr 2003.

[82] T. J. Yen, W. J. Padilla, N. Fang, D. C. Vier, D. R. Smith, J. B. Pendry, D. N. Basov, and X. Zhang. Terahertz magnetic response from artificial materials. *Science*, 303(5663):1494–1496, 2004.

[83] G. Dolling, C. Enkrich, M. Wegener, C. M. Soukoulis, and S. Linden. Simultaneous negative phase and group velocity of light in a metamaterial. *Science*, 312(5775):892–894, 2006.

[84] L. Peng, L. Ran, H. Chen, H. Zhang, J. A. Kong, and T. M. Grzegorczyk. Experimental observation of left-handed behavior in an array of standard dielectric resonators. *Phys. Rev. Lett.*, 98:157403, Apr 2007.

[85] Q. Zhao, L. Kang, B. Du, H. Zhao, Q. Xie, X. Huang, B. Li, J. Zhou, and L. Li. Experimental demonstration of isotropic negative permeability in a three-dimensional dielectric composite. *Phys. Rev. Lett.*, 101:027402, Jul 2008.

[86] J. Valentine, S. Zhang, T. Zentgraf, E. Ulin-Avila, D. A. Genov, G. Bartal, and X. Zhang. Three-dimensional optical metamaterial with a negative refractive index. *Nature (London)*, 455:376–379, Sep 2008.

[87] C. G. Parazzoli, R. B. Greegor, J. A. Nielsen, M. A. Thompson, K. Li, A. M. Vetter, M. H. Tanielian, and D. C. Vier. Performance of a negative index of refraction lens. *Applied Physics Letters*, 84(17):3232–3234, 2004.

[88] J. B. Pendry. Negative refraction makes a perfect lens. *Phys. Rev. Lett.*, 85:3966–3969, Oct 2000.

[89] N. Fang, H. Lee, C. Sun, and X. Zhang. Sub-diffraction-limited optical imaging with a silver superlens. *Science*, 308(5721):534–537, 2005.

[90] Z. Liu, H. Lee, Y. Xiong, C. Sun, and X. Zhang. Far-field optical hyperlens magnifying sub-diffraction-limited objects. *Science*, 315(5819):1686–1686, 2007.

[91] U. Leonhardt. Optical conformal mapping. *Science*, 312(5781):1777–1780, 2006.

[92] J. B. Pendry, D. Schurig, and D. R. Smith. Controlling electromagnetic fields. *Science*, 312(5781):1780–1782, 2006.

[93] D. Schurig, J. J. Mock, B. J. Justice, S. A. Cummer, J. B. Pendry, A. F. Starr, and D. R. Smith. Metamaterial electromagnetic cloak at microwave frequencies. *Science*, 314(5801):977–980, 2006.

[94] J. Li and J. B. Pendry. Hiding under the carpet: A new strategy for cloaking. *Phys. Rev. Lett.*, 101:203901, Nov 2008.

[95] J. Valentine, J. Li, T. Zentgraf, G. Bartal, and X. Zhang. An optical cloak made of dielectrics. *Nature Materials*, 8:568–571, Apr 2009.

[96] H. Chen, C. T. Chan, and P. Sheng. Transformation optics and metamaterials. *Nature Materials*, 9:387–396, Apr 2010.

[97] N. I. Landy, S. Sajuyigbe, J. J. Mock, D. R. Smith, and W. J. Padilla. Perfect metamaterial absorber. *Phys. Rev. Lett.*, 100:207402, May 2008.

[98] X. Liu, T. Starr, A. F. Starr, and W. J. Padilla. Infrared spatial and frequency selective metamaterial with near-unity absorbance. *Phys. Rev. Lett.*, 104:207403, May 2010.

[99] X. Liu, T. Tyler, T. Starr, A. F. Starr, N. M. Jokerst, and W. J. Padilla. Taming the blackbody with infrared metamaterials as selective thermal emitters. *Phys. Rev. Lett.*, 107:045901, Jul 2011.

[100] C. M. Soukoulis, S. Linden, and M. Wegener. Negative refractive index at optical wavelengths. *Science*, 315(5808):47–49, 2007.

[101] V. M. Shalaev. Optical negative-index metamaterials. *Nature Photonics*, 1:41–48, 2007.

[102] A. Sihvola. Metamaterials in electromagnetics. *Metamaterials*, 1(1):2 – 11, 2007.

[103] A. De Baas, editor. *Nanostructured metamaterials*. Publication Office of the European Union, Luxembourg, 2010.

[104] N. I Zheludev and Y. S. Kivshar. From metamaterials to metadevices. *Nature Materials*, 11:917924, 2012.

[105] G. V. Eleftheriades and K. G. Balmain, editors. *Negative-Refraction Metamaterials: Fundamental Principles and Applications*. Wiley - IEEE. Wiley - IEEE, New Jersey, 2005.

[106] N. Engheta and R. W. Ziolkowski. *Metamaterials: Physics and Engineering Explorations*. Wiley - IEEE, New Jersey, 2006.

[107] A. K. Sarychev and V. M. Shalaev. *Electrodynamics of Metamaterials*. World Scientific, Singapore, 2007.

[108] R. Marqués, F. Martín, and M. Sorolla. *Metamaterials with Negative Parameters: Theory, Design, and Microwave Applications*. Wiley Series in Microwave and Optical Engineering. Wiley, New Jersey, 2008.

[109] S. A. Ramakrishna and T. M. Grzegorczyk. *Physics and Applications of Negative Refractive Index Materials*. SPIE press monograph: SPIE. Taylor & Francis, Boca Raton, 2009.

[110] T. J. Cui, D. R. Smith, and R. Liu, editors. *Metamaterials: Theory, Design, and Applications*. Springer, New York, 2010.

[111] B. Banerjee. *An Introduction to Metamaterials and Waves in Composites*. Taylor & Francis, Boca Raton, 2011.

[112] A. A. Maradudin, editor. *Structured Surfaces as Optical Metamaterials*. Cambridge Univ. Press, Cambridge, 2011.

[113] A. Andreone, A. Cusano, A. Cutolo, and V. Galdi, editors. *Selected Topics in Photonic Crystals and Metamaterials*. World Scientific, Singapore, 2011.

[114] G. Shvets and I. Tsukerman, editors. *Plasmonics and Plasmonic Metamaterials: Analysis and Applications*. World Scientific series in nanoscience and nanotechnology. World Scientific Publishing, Singapore, 2012.

[115] A. V. Zayats and S. Maier, editors. *Active Plasmonics and Tuneable Plasmonic Metamaterials*. A Wiley-Science Wise Co-Publication. Wiley, New Jersey, 2013.

[116] D. H. Werner and D. H. Kwon, editors. *Transformation Electromagnetics and Metamaterials: Fundamental Principles and Applications*. Springer, London, 2014.

[117] I. V. Shadrivov, M. Lapine, and Y. S. Kivshar, editors. *Nonlinear, Tunable and Active Metamaterials*. Springer Series in Materials Science. Springer, Cham, 2015.

[118] C. Enkrich, M. Wegener, S. Linden, S. Burger, L. Zschiedrich, F. Schmidt, J. F. Zhou, Th. Koschny, and C. M. Soukoulis. Magnetic metamaterials at telecommunication and visible frequencies. *Phys. Rev. Lett.*, 95:203901, Nov 2005.

[119] S. Chikazumi. *Physics of Ferromagnetism*. Oxford Univ. Press, Oxford, 1997.

[120] S. T. Chui and L. Hu. Theoretical investigation on the possibility of preparing left-handed materials in metallic magnetic granular composites. *Phys. Rev. B*, 65:144407, Mar 2002.

[121] C. Mitsumata and S. Tomita. Negative permeability of magnetic nanocomposite films for designing left-handed metamaterials. *Applied Physics Letters*, 91(22):223104, 2007.

[122] C. Mitsumata, S. Tomita, M. Hagiwara, and K. Akamatsu. Electron magnetic resonance in interacting ferromagnetic-metal nanoparticle systems: experiment and numerical simulation. *Journal of Physics: Condensed Matter*, 22(1):016005, 2010.

[123] C. Mitsumata and S. Tomita. Control of gilbert damping using magnetic metamaterials. *Phys. Rev. B*, 84:174421, Nov 2011.

[124] C. Mitsumata and S. Tomita. Analytic solution of gilbert damping in landau-lifshitz-gilbert equation in magnetic resonance due to spin torque oscillation. *Journal of the Magnetics Society of Japan*, 36(4):301–303, 2012.

[125] S. Tomita, M. Hagiwara, T. Kashiwagi, C. Tsuruta, Y. Matsui, M. Fujii, and S. Hayashi. Ferromagnetic resonance study of diluted fe nanogranular films. *Journal of Applied Physics*, 95(12):8194–8198, 2004.

[126] K. Akamatsu, H. Shinkai, S. Ikeda, S. Adachi, H. Nawafune, and S. Tomita. Controlling interparticle spacing among metal nanoparticles through metal-catalyzed decomposition of surrounding polymer matrix. *Journal of the American Chemical Society*, 127(22):7980–7981, 2005. PMID: 15926799.

[127] S. Tomita, K. Akamatsu, H. Shinkai, S. Ikeda, H. Nawafune, C. Mitsumata, T. Kashiwagi, and M. Hagiwara. Tuning magnetic interactions in ferromagnetic-metal nanoparticle systems. *Phys. Rev. B*, 71:180414, May 2005.

[128] S. Tomita, P. E. Jönsson, K. Akamatsu, H. Nawafune, and H. Takayama. Controlled magnetic properties of ni nanoparticles embedded in polyimide films. *Phys. Rev. B*, 76:174432, Nov 2007.

[129] K. Akamatsu, S. Adachi, T. Tsuruoka, S. Ikeda, S. Tomita, and H. Nawafune. Nanocomposite polymeric microspheres containing ni nanoparticles with controlled microstructures. *Chemistry of Materials*, 20(9):3042–3047, 2008.

[130] R. V. Mikhaylovskiy, E. Hendry, and V. V. Kruglyak. Negative permeability due to exchange spin-wave resonances in thin magnetic films with surface pinning. *Phys. Rev. B*, 82:195446, Nov 2010.

[131] T. Tsutaoka, K. Fukuyama, H. Kinoshita, T. Kasagi, S. Yamamoto, and K. Hatakeyama. Negative permittivity and permeability spectra of cu/yttrium iron garnet hybrid granular composite materials in the microwave frequency range. *Applied Physics Letters*, 103(26):261906, 2013.

[132] A. Pimenov, A. Loidl, P. Przyslupski, and B. Dabrowski. Negative refraction in ferromagnet-superconductor superlattices. *Phys. Rev. Lett.*, 95:247009, Dec 2005.

[133] S. Tomita, M. Fujii, S. Hayashi, A. Terai, and N. Nabatova-Gabain. Spectroscopic ellipsometry of yttriumiron garnet thin films containing gold nanoparticles. *Japanese Journal of Applied Physics*, 46(11L):L1032, 2007.

[134] G. Armelles, A. Cebollada, A. García-Martín, and M. U. González. Magnetoplasmonics: Combining magnetic and plasmonic functionalities. *Advanced Optical Materials*, 1(1):10–35, 2013.

[135] G. H. B. Thompson. Unusual waveguide characteristics associated with the apparent negative permeability obtainable in ferrites. *Nature (London)*, 175:1135 – 1136, 1955.

[136] P. Thibaudeau and J. Tranchida. Frequency-dependent effective permeability tensor of unsaturated polycrystalline ferrites. *Journal of Applied Physics*, 118(5):053901, 2015.

[137] M. Tsutsumi and T. Ueda. Nonreciprocal left-handed microstrip lines using ferrite substrate. In *2004 IEEE MTT-S International Microwave Symposium Digest (IEEE Cat. No.04CH37535)*, volume 1, pages 249–252 Vol.1, June 2004.

[138] T. Ueda and M. Tsutsumi. Left-handed transmission characteristics of ferrite microstrip lines without series capacitive loading. *IEICE TRANSACTIONS on Electronics*, E89-C(9):1318–1323, 2006.

[139] T. Ueda and M. Tsutsumi. Left-handed transmission characteristics of rectangular waveguides periodically loaded with ferrite. *IEEE Transactions on Magnetics*, 41(10):3532–3537, Oct 2005.

[140] T. Kodera and C. Caloz. Uniform ferrite-loaded open waveguide structure with crlh response and its application to a novel backfire-to-endfire leaky-wave antenna. *IEEE Transactions on Microwave Theory and Techniques*, 57(4):784–795, April 2009.

[141] T. Ueda, K. Horikawa, M. Akiyama, and M. Tsutsumi. Nonreciprocal phase-shift composite right/left handed transmission lines and their application to leaky wave antennas. *IEEE Transactions on Antennas and Propagation*, 57(7):1995–2005, July 2009.

[142] T. Ueda and M. Akiyama. Nonreciprocal phase-shift composite right/left handed microstrip lines using ferrite-rod-embedded substrate. *IEEE Transactions on Magnetics*, 45(10):4203–4206, Oct 2009.

[143] T. Ueda and H. Kishimoto. Pseudo-traveling-wave resonator based on nonreciprocal phase-shift composite right/left handed transmission lines. In *2010 IEEE MTT-S International Microwave Symposium*, pages 41–44, May 2010.

[144] H. Kishimoto, T. Ueda, and Y. Kado. Experimental demonstration of nonreciprocal phase-shift composite right/left handed transmission lines using a ferrite-rod-embedded substrate. *IEEE Transactions on Magnetics*, 47(10):3724–3727, Oct 2011.

[145] T. Ueda, S. Yamamoto, Y. Kado, and T. Itoh. Pseudo-traveling-wave resonator with magnetically tunable phase gradient of fields and its applications to beam-steering antennas. *IEEE Transactions on Microwave Theory and Techniques*, 60(10):3043–3054, Oct 2012.

[146] A. Porokhnyku, T. Ueda, Y. Kado, and T. Itoh. Mode analysis of phase-constant nonreciprocity in ferrite-embedded crlh metamaterials. *IEICE TRANSACTIONS on Electronics*, E96-C(10):1263–1272, 2013.

[147] A. Porokhnyuk, T. Ueda, Y. Kado, and T. Itoh. Phase-constant-nonreciprocal composite right/left-handed metamaterials based on coplanar waveguides. *Journal of Applied Physics*, 115(17):17E519, 2014.

[148] T. Ueda, K. Ninomiya, K. Yoshida, and Itoh. T. Design of dispersion-free phase-shifting non-reciprocity in composite right/left handed metamaterials. In *2016 IEEE MTT-S International Microwave Symposium (IMS)*, pages 1–4, May 2016.

[149] J. C. Bose. On the rotation of plane of polarisation of electric waves by a twisted structure. *Proc. R. Soc. Lond.*, 63:146–152, 1898.

[150] J. D. Kraus. The helical antenna. *Proceedings of the IRE*, 37(3):263–272, March 1949.

[151] I. Tinoco Jr. and R. W. Woody. Optical rotation of oriented helices. iv. a free electron on a helix. *The Journal of Chemical Physics*, 40(1):160–165, 1964.

[152] Y. Svirko, N. Zheludev, and M. Osipov. Layered chiral metallic microstructures with inductive coupling. *Applied Physics Letters*, 78(4):498–500, 2001.

[153] A. S. Schwanecke, A. Krasavin, D. M. Bagnall, A. Potts, A. V. Zayats, and N. I. Zheludev. Broken time reversal of light interaction with planar chiral nanostructures. *Phys. Rev. Lett.*, 91:247404, Dec 2003.

[154] A. V. Rogacheva, V. A. Fedotov, A. S. Schwanecke, and N. I. Zheludev. Giant gyrotropy due to electromagnetic-field coupling in a bilayered chiral structure. *Phys. Rev. Lett.*, 97:177401, Oct 2006.

[155] F. Miyamaru and M. Hangyo. Strong optical activity in chiral metamaterials of metal screw hole arrays. *Applied Physics Letters*, 89(21):211105, 2006.

[156] M. Decker, M. W. Klein, M. Wegener, and S. Linden. Circular dichroism of planar chiral magnetic metamaterials. *Opt. Lett.*, 32(7):856–858, Apr 2007.

[157] V. K. Valev, J. J. Baumberg, C. Sibilia, and T. Verbiest. Chirality and chiroptical effects in plasmonic nanostructures: Fundamentals, recent progress, and outlook. *Advanced Materials*, 25(18):2517–2534, 2013.

[158] M. Kuwata-Gonokami, N. Saito, Y. Ino, M. Kauranen, K. Jefimovs, T. Vallius, J. Turunen, and Y. Svirko. Giant optical activity in quasi-two-dimensional planar nanostructures. *Phys. Rev. Lett.*, 95:227401, Nov 2005.

[159] E. Plum, V. A. Fedotov, A. S. Schwanecke, N. I. Zheludev, and Y. Chen. Giant optical gyrotropy due to electromagnetic coupling. *Applied Physics Letters*, 90(22):223113, 2007.

[160] K. Konishi, M. Nomura, N. Kumagai, S. Iwamoto, Y. Arakawa, and M. Kuwata-Gonokami. Circularly polarized light emission from semiconductor planar chiral nanostructures. *Phys. Rev. Lett.*, 106:057402, Feb 2011.

[161] Y. Tamayama, T. Nakanishi, K. Sugiyama, and M. Kitano. An invisible medium for circularly polarized electromagnetic waves. *Opt. Express*, 16(25):20869–20875, Dec 2008.

[162] J. K. Gansel, M. Thiel, M. S. Rill, M. Decker, K. Bade, V. Saile, G. von Freymann, S. Linden, and M. Wegener. Gold helix photonic metamaterial as broadband circular polarizer. *Science*, 325(5947):1513–1515, 2009.

[163] T. Kan, A. Isozaki, N. Kanda, N. Nemoto, K. Konishi, H. Takahashi, M. Kuwata-Gonokami, K. Matsumoto, and I. Shimoyama. Enantiomeric switching of chiral metamaterial for terahertz polarization modulation employing vertically deformable mems spirals. *Nature Communications*, 6:8422, 2015.

[164] J. B. Pendry. A chiral route to negative refraction. *Science*, 306(5700):1353–1355, 2004.

[165] J. Kästel, M. Fleischhauer, S. F. Yelin, and R. L. Walsworth. Tunable negative refraction without

absorption via electromagnetically induced chirality. *Phys. Rev. Lett.*, 99:073602, Aug 2007.

[166] E. Plum, J. Zhou, J. Dong, V. A. Fedotov, T. Koschny, C. M. Soukoulis, and N. I. Zheludev. Metamaterial with negative index due to chirality. *Phys. Rev. B*, 79:035407, Jan 2009.

[167] S. Zhang, Y.-S. Park, J. Li, X. Lu, W. Zhang, and X. Zhang. Negative refractive index in chiral metamaterials. *Phys. Rev. Lett.*, 102:023901, Jan 2009.

[168] K. F. Lindman. Über eine durch ein isotropes system von spiralförmigen resonatoren erzeugte rotationspolarisation der elektromagnetischen wellen. *Annalen der Physik*, 368(23):621–644, 1920.

[169] C. L. Hogan. The ferromagnetic faraday effect at microwave frequencies and its applications: The microwave gyrator. *The Bell System Technical Journal*, 31(1):1–31, Jan 1952.

[170] D. M. Pozar. *Microwave Engineering*. Wiley, New York, 2004.

[171] G. B. G. Stenning, G. J. Bowden, L. C. Maple, S. A. Gregory, A. Sposito, R. W. Eason, N. I. Zheludev, and P. A. J. de Groot. Magnetic control of a meta-molecule. *Opt. Express*, 21(2):1456–1464, Jan 2013.

[172] F. Balhorn, S. Mansfeld, A. Krohn, J. Topp, W. Hansen, D. Heitmann, and S. Mendach. Spin-wave interference in three-dimensional rolled-up ferromagnetic microtubes. *Phys. Rev. Lett.*, 104:037205, Jan 2010.

[173] E. J. Smith, Z. Liu, Y. Mei, and O. G. Schmidt. Combined surface plasmon and classical waveguiding through metamaterial fiber design. *Nano Letters*, 10(1):1–5, 2010. PMID: 19368372.

[174] M. Huang, F. Cavallo, F. Liu, and M. G. Lagally. Nanomechanical architecture of semiconductor nanomembranes. *Nanoscale*, 3:96–120, 2011.

[175] E. J. Smith, D. Makarov, S. Sanchez, V. M. Fomin, and O. G. Schmidt. Magnetic microhelix coil structures. *Phys. Rev. Lett.*, 107:097204, Aug 2011.

[176] E. J. Smith, D. Makarov, and O. G. Schmidt. Polymer delamination: towards unique three-dimensional microstructures. *Soft Matter*, 7:11309–11313, 2011.

[177] C. Müller, C. C. Bof Bufon, M. E. Navarro Fuentes, D. Makarov, D. H. Mosca, and O. G. Schmidt. Towards compact three-dimensional magnetoelectronicsmagnetoresistance in rolled-up co/cu nanomembranes. *Applied Physics Letters*, 100(2):022409, 2012.

[178] Ch. Strelow, C. M. Schultz, H. Rehberg, M. Sauer, H. Welsch, A. Stemmann, Ch. Heyn, D. Heitmann, and T. Kipp. Light confinement and mode splitting in rolled-up semiconductor microtube bottle resonators. *Phys. Rev. B*, 85:155329, Apr 2012.

[179] R. Streubel, J. Lee, D. Makarov, M.-Y. Im, D. Karnaushenko, L. Han, R. Schäfer, P. Fischer, S.-K. Kim, and O. G. Schmidt. Magnetic microstructure of rolled-up single-layer ferromagnetic nanomembranes. *Advanced Materials*, 26(2):316–323, 2014.

[180] R. Streubel, L. Han, F. Kronast, A. A. Ünal, O. G. Schmidt, and D. Makarov. Imaging of buried 3d magnetic rolled-up nanomembranes. *Nano Letters*, 14(7):3981–3986, 2014. PMID: 24849571.

[181] R. Streubel, F. Kronast, D Fischer, D. Parkinson, O. G. Schmidt, and D. Makarov. Retrieving spin textures on curved magnetic thin films with full-field soft x-ray microscopies. *Nature Communications*, 6:7612, 2015.

[182] C.-C. Chen, A. Ishikawa, Y.-H. Tang, M.-H. Shiao, D. P. Tsai, and T. Tanaka. Uniaxial-isotropic metamaterials by three-dimensional split-ring resonators. *Advanced Optical Materials*, 3(1):44–48, 2015.

[183] J. P. Nibarger, R. Lopusnik, Z. Celinski, and T. J. Silva. Variation of magnetization and the land g factor with thickness in nife films. *Applied Physics Letters*, 83(1):93–95, 2003.

[184] C. Kittel. *Introduction to Solid State Physics*. Weily, New York, 1995.

[185] Y. Ajiro, H. Yamazaki, K. Kawaguchi, N. Hosoito, and T. Shinjo. Ferromagnetic resonance of fe/mg multilayered films with artificial superstructure. *Journal of the Physical Society of Japan*, 58(9):3339–3346, 1989.

[186] J. M. Shaw, H. T. Nembach, and T. J. Silva. Determination of spin pumping as a source of

linewidth in sputtered co$_{90}$fe$_{10}$/pd multilayers by use of broadband ferromagnetic resonance spectroscopy. *Phys. Rev. B*, 85:054412, Feb 2012.

[187] C. E. Patton, C. H. Wilts, and F. B. Humphrey. Relaxation processes for ferromagnetic resonance in thin films. *Journal of Applied Physics*, 38(3):1358–1359, 1967.

[188] B. Heinrich, J. F. Cochran, and R. Hasegawa. Fmr linebroadening in metals due to twomagnon scattering. *Journal of Applied Physics*, 57(8):3690–3692, 1985.

[189] J. M. Shaw, H. T. Nembach, T. J. Silva, and C. T. Boone. Precise determination of the spectroscopic g-factor by use of broadband ferromagnetic resonance spectroscopy. *Journal of Applied Physics*, 114(24):243906, 2013.

[190] C.-Y. Hung, M. Mao, S. Funada, T. Schneider, L. Miloslavsky, M. Miller, C. Qian, and H. C. Tong. Magnetic properties of ultrathin nife and cofe films. *Journal of Applied Physics*, 87(9):6618–6620, 2000.

[191] N. Pérez, M. Melzer, D. Makarov, O. Ueberschär, R. Ecke, S. E. Schulz, and O. G. Schmidt. High-performance giant magnetoresistive sensorics on flexible si membranes. *Applied Physics Letters*, 106(15):153501, 2015.

[192] F. Giesen, J. Podbielski, and D. Grundler. Mode localization transition in ferromagnetic microscopic rings. *Phys. Rev. B*, 76:014431, Jul 2007.

[193] S. Mendach, J. Podbielski, J. Topp, W. Hansen, and D. Heitmann. Spin-wave confinement in rolled-up ferromagnetic tubes. *Applied Physics Letters*, 93(26):262501, 2008.

[194] M. Kobayashi, S. Tomita, K. Sawada, K. Shiba, H. Yanagi, I. Yamashita, and Y. Uraoka. Chiral meta-molecules consisting of gold nanoparticles and genetically engineered tobacco mosaic virus. *Opt. Express*, 20(22):24856–24863, Oct 2012.

[195] A. D. Malay, J. G. Heddle, S. Tomita, K. Iwasaki, N. Miyazaki, K. Sumitomo, H. Yanagi, I. Yamashita, and Y. Uraoka. Gold nanoparticle-induced formation of artificial protein capsids. *Nano Letters*, 12(4):2056–2059, 2012. PMID: 22414047.

[196] P.-S. Huang, G. Oberdorfer, C. Xu, X. Y. Pei, B. L. Nannenga, J. M. Rogers, F. DiMaio, T. Gonen, B. Luisi, and D. Baker. High thermodynamic stability of parametrically designed helical bundles. *Science*, 346(6208):481–485, 2014.

[197] G. Wagnière. Inverse magnetochiral birefringence. *Phys. Rev. A*, 40:2437–2440, Sep 1989.

[198] L.P. Pitaevskii. Electric forces in a transparent dispersive medium. *Sov. Phys. JETP*, 12:1008, 1961.

[199] J. P. van der Ziel, P. S. Pershan, and L. D. Malmstrom. Optically-induced magnetization resulting from the inverse faraday effect. *Phys. Rev. Lett.*, 15:190–193, Aug 1965.

[200] G. H. Wagnière and G. L.J.A. Rikken. Chirality and magnetism ii: Free electron on an infinite helix, inverse faraday effect and inverse magnetochiral effect. *Chemical Physics Letters*, 502(13):126 – 129, 2011.

[201] P. Landeros and Á. S. Núñez. Domain wall motion on magnetic nanotubes. *Journal of Applied Physics*, 108(3):033917, 2010.

[202] V. K. Dugaev, P. Bruno, B. Canals, and C. Lacroix. Berry phase of magnons in textured ferromagnets. *Phys. Rev. B*, 72:024456, Jul 2005.

[203] Y. Moritake, K. Nakayama, T. Suzuki, H. Kurosawa, T. Kodama, S. Tomita, H. Yanagi, and T. Ishihara. Lifetime reduction of a quantum emitter with quasiperiodic metamaterials. *Phys. Rev. B*, 90:075146, Aug 2014.

[204] Y. E. Kraus, Y. Lahini, Z. Ringel, M. Verbin, and O. Zilberberg. Topological states and adiabatic pumping in quasicrystals. *Phys. Rev. Lett.*, 109:106402, Sep 2012.

[205] M. Verbin, O. Zilberberg, Y. E. Kraus, Y. Lahini, and Y. Silberberg. Observation of topological phase transitions in photonic quasicrystals. *Phys. Rev. Lett.*, 110:076403, Feb 2013.

[206] G.-D. Pang and F.-C. Pu. Ferromagnetic spin waves in quasiperiodic superlattices. *Phys. Rev. B*, 38:12649–12652, Dec 1988.

[207] D. H. A. L. Anselmo, M. G. Cottam, and E. L. Albuquerque. Magnetostatic modes in quasiperiodic fibonacci magnetic superlattices. *Journal of Applied Physics*, 85(8):5774–5776,

1999.

[208] V. S. Bhat, J. Sklenar, B. Farmer, J. Woods, J. T. Hastings, S. J. Lee, J. B. Ketterson, and L. E. De Long. Controlled magnetic reversal in permalloy films patterned into artificial quasicrystals. *Phys. Rev. Lett.*, 111:077201, Aug 2013.

[209] L. D. Machado, C. G. Bezerra, M. A. Correa, C. Chesman, J. E. Pearson, and A. Hoffmann. Static and dynamic properties of fibonacci multilayers. *Journal of Applied Physics*, 113(17):17C102, 2013.

[210] J. Rychły, J. W. Kłos, M. Mruczkiewicz, and M. Krawczyk. Spin waves in one-dimensional bicomponent magnonic quasicrystals. *Phys. Rev. B*, 92:054414, Aug 2015.

[211] T. Suwa, S. Tomita, N. Hosoito, and H. Yanagi. Magnetic properties of fibonacci-modulated fe-au multilayer metamaterials. *Materials*, 10(10):1209, 2017.

[212] G. L. J. A. Rikken, J. Fölling, and P. Wyder. Electrical magnetochiral anisotropy. *Phys. Rev. Lett.*, 87:236602, Nov 2001.

[213] L. Onsager. Reciprocal relations in irreversible processes. i. *Phys. Rev.*, 37:405–426, Feb 1931.

[214] L. Onsager. Reciprocal relations in irreversible processes. ii. *Phys. Rev.*, 38:2265–2279, Dec 1931.

[215] L. D. Landau, E. M. Lifshitz, and L. P. Pitaevskii. *Electrodynamics of Continuous Media.* Butterworth-Heinemann, Oxford, 2008.

[216] V. Krstić, S. Roth, M. Burghard, K. Kern, and G. L. J. A. Rikken. Magneto-chiral anisotropy in charge transport through single-walled carbon nanotubes. *The Journal of Chemical Physics*, 117(24):11315–11319, 2002.

[217] F. Pop, P. Auban-Senzier, E. Canadell, G. L. J. A. Rikken, and N. Avarvari. Electrical magnetochiral anisotropy in a bulk chiral molecular conductor. *Nature Communications*, 5:3757, 2014.

[218] A. De Martino, R. Egger, and A. M. Tsvelik. Nonlinear magnetotransport in interacting chiral nanotubes. *Phys. Rev. Lett.*, 97:076402, Aug 2006.

[219] T Yokouchi, N. Kanazawa, A. Kikkawa, D. Morikawa, K. Shibata, T. Arima, Y. Taguchi, F. Kagawa, and Y. Tokura. Electrical magnetochiral effect induced by chiral spin fluctuations. *Nature Communications*, 8:866, 2017.

[220] Z. Wang, Y. Chong, J. D. Joannopoulos, and M. Soljačić. Observation of unidirectional backscattering-immune topological electromagnetic states. *Nature (London)*, 461:772–775, 2009.

[221] H. Hisamoto, T. Ueda, K. Sawada, and S. Tomita. Observation of asymmetric electromagnetic field profiles in chiral metamaterials. *submitted*.